Deeply-etched DBR mirrors for photonic integrated circuits and tunable lasers

Document status and date:
Published: 01/01/2009

Document Version:
Publisher's PDF, also known as Version of Record (includes final page, issue and volume numbers)

Please check the document version of this publication:

Deeply-Etched DBR Mirrors for Photonic Integrated Circuits and Tunable Lasers

PROEFSCHRIFT

ter verkrijging van de graad van doctor aan de
Technische Universiteit Eindhoven, op gezag van de
rector magnificus, prof.dr.ir. C.J. van Duijn, voor een
commissie aangewezen door het College voor
Promoties in het openbaar te verdedigen
op donderdag 1 oktober 2009 om 16.00 uur

door

Boudewijn Docter

geboren te Amsterdam

Dit proefschrift is goedgekeurd door de promotor:

prof.dr.ir. M.K. Smit

Copromotoren:
dr. F. Karouta
en
dr. J.J.G.M. van der Tol

Table of contents

SEM gallery

"The beginning"

The very first realization of a DBR pattern at TU/e.

1 Introduction & State of the Art

Optical fiber communication systems have proven over the past few decades to be a very efficient solution to the ever increasing demand for communication bandwidth. Being the "highway" of the communication infrastructure, the glass network is extending further each year. Where in the past only long range (>100 km) connections were made using optical fiber, today more and more cities are deploying so-called 'metro networks'. The number of Fiber-To-The-Home (FTTH) connections is increasing exponentially, with Japan being the leading market in this field. Optical fiber is expected to replace (A)DSL or other electrical broad-band subscriber connections in the near future [1].

With this increase in deployment of the optical network, the switching nodes are becoming more complex. This is the main driving force behind the research on Photonic Integrated Circuits (PICs), where the main goal is to combine many optical components on a single chip. The main advantage of this integration is the reduced number of fiber-chip couplings, decreasing overall losses and increasing the stability [2]. Additionally the reduced number of Optical-Electrical-Optical (O-E-O) conversions leads to an increase of the overall speed of the switching nodes.

Traditionally, researchers active in the area of Photonic Integrated Circuits have used the argument of potential cost reduction to defend large investments in fabrication and characterization equipment. This cost reduction was foreseen because once a successful design was made, many thousands of similar devices could be made in the same fabrication process – analogous to the economics that drive the CMOS electronics businesses these days. However, since this business model requires large production volumes, while on the other hand the devices have to be cheap to be applied in large numbers, there is a 'chicken and egg' problem that so far seems to prevent the market for PICs to grow.

Recently there have been some interesting developments though. Many players in academia and industry have realized that the investment required to set up a stable production process that is able to produce optical chips in large quantities is so big that it cannot be realized by every player in the market. It is therefore necessary to move to a generic fabrication technology in which with standardized basic building blocks many optical functionalities can be realized on a single chip [3].

With the current state-of-the-art technology, when a designer wants to create for example a multi-wavelength laser, a cleaved chip facet is often used as a broadband mirror. However, the chip cleaving process is not very accurate (+/- 10 µm) and therefore the resulting cavity length varies with each fabrication run. And since the cavity length determines which wavelengths can resonate, there is always some uncertainty in the final operation wavelength.

Chapter 1

The research presented in this thesis is focused on adding a new building block in the generic integration technology: a deeply-etched Distributed Bragg Reflector (DBR) mirror. The DBR mirror adds a lot of design functionality, because with this component it is possible to place a broadband mirror anywhere on a chip, creating laser cavities with very accurate lengths. Another advantage of the DBR mirror over a cleaved chip facet is that with a DBR mirror the light that is not reflected by the mirror is still on the chip and can be used for other purposes. This allows us to create (for example) an external filtered-feedback circuit which can be used to switch a multimode laser, as will be shown in Chapter 6 of this thesis.

The purpose of this introduction chapter is to further explain the basic terminology used in this thesis and to show the current state of the art in PIC technology using DBR mirrors. First the working principle of DBR mirrors is introduced, followed by the most commonly used material platforms for PIC fabrication. Although the work in this thesis focuses on the Indium-Phosphide (InP) material system, it is good to have an overview of the other PIC platforms in order to put the work into perspective.

There are currently many groups working on DBR mirrors for PICs. The most widely used designs will be shown in section 1.3, together with their main application areas. Finally the structure of the rest of the thesis is explained.

1.1 Distributed Bragg Reflector (DBR) mirrors

Distributed Bragg Reflector (DBR) mirrors are widely used in photonic applications. The terms DBR mirror and (DBR-) grating are both often used in the literature to indicate a periodic structure that reflects light. In this thesis both terms will also be used. The principle behind the DBR mirror is illustrated in figure 1.1. A light wave that travels through a medium, with a certain refractive index, reaches an interface with a material with a different refractive index. Depending on the refractive index difference, part of the light is transmitted and another part of the light is reflected. When multiple interfaces are placed at constant intervals, a periodic structure is created in which, for certain wavelengths, all the reflections will add up in phase to form a very high total reflection.
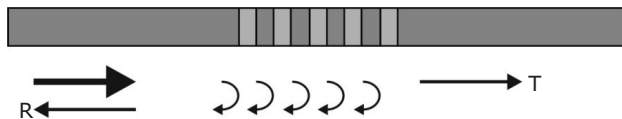
Figure 1.1: Principle of a DBR mirror: multiple reflections add-up to form a wavelength-selective total reflection (R). Some of the light is transmitted (T).

By varying the position of the interfaces (the period of the grating) and the refractive index difference of the materials (the amplitude of the grating) it is possible to tune the reflection and transmission properties. It is possible to make very wide-bandwidth reflectors, but it is also possible to make very narrow-band reflectors that can serve as wavelength filters. As a general rule, the lower the refractive index difference, the more reflections build up the total

reflection. This requires a more stringent phase condition which results in a narrower reflection bandwidth.

Low index-difference gratings are mostly used in Fiber Bragg Gratings (FBGs), where the narrow bandwidth of the grating is exploited, for example in FBG sensor applications [4]. In PICs these kind of gratings are often used in tunable lasers, where the grating element serves as a wavelength filter that makes the laser operate on one single wavelength. Examples are tunable DBR lasers [5,6] and Distributed FeedBack (DFB) lasers [7].

Wide bandwidth gratings are used in multimode Fabry-Perot lasers, where the bandwidth of the grating should cover the total gain bandwidth of the material used. High index difference gratings are therefore used. These gratings can be formed by multi-layered coatings on chip facets, or by etching narrow gaps through the waveguide channel. The latter is the main focus of the research in this thesis.

1.2 Photonic Integrated Circuits (PICs)

A photonic integrated circuit (PIC) can be defined as a waveguide-based circuit that contains more than one component, integrated on the same chip. There are several material systems, or platforms, in which the circuits can be realized, each with their advantages and disadvantages, each suitable for a specific set of applications.

Silica-based platforms are very suitable for extremely low-loss devices. This is not only due to the existence of high quality manufacturing processes, but also because the refractive index matches that of standard optical fibers (n=1.45), making it possible to realize fiber-chip couplings with very low loss [8]. However, because the refractive index contrast is generally low, circuits tend to get very big (several cm^2), since the bending radius of a curved waveguide scales inversely with the lateral index contrast. Monolithic integration with active components (amplifiers, fast switches) is not possible in this material.

Recent advances in silicon-oxi-nitride (SiON) technology have shown that it is possible to obtain the same low propagation losses also in a higher refractive index (n=1.45-2.0) material and also maintain good polarization properties [9]. However, the lack of active components is still a limitation for some applications.

In the past few years another new material system has gained much attention: silicon-on-insulator or SOI [10]. The SOI platform uses silicon as the main waveguiding material. It has a high refractive index (n=3.6), and the refractive index contrast in the vertical direction can be made very high as well, because the silicon waveguide layer is separated from the substrate by low-index SiO$_2$. This allows to shrink the waveguide dimensions further, rendering very small circuits (<1 mm^2). Furthermore, processing benefits from the expertise gained in the silicon electronics industry and large wafer sizes (up to 8 inch) promise low chip costs in the future. However, due to the high refractive index, fiber-chip coupling can be cumbersome and no active functionality has been obtained yet in SOI

technology. Many researchers are trying to combine the SOI technology with InP/InGaAsP technology to use the advantages of both worlds, but this is still in an early stage[11].

The indium-phosphide/indium-gallium-arsenide-phosphide (InP/InGaAsP) material system also has a high refractive index (n=3.17-3.46). Circuits made in this material system are therefore also compact. As a direct-bandgap semiconductor material it is suitable for applications where the electrical carriers have to interact with the photons, e.g. electrically pumped optical amplifiers and lasers. Also the non-linear properties can be exploited for fast switches and wavelength conversion. The broad gain-spectrum for light in the 950-1650 nm range makes it very suitable for telecommunication applications. A moderately complex circuit can be made on a few mm^2, and therefore many devices can be realized on a single 2-4 inch wafer, which is the standard today.

In this thesis we focus on InP/InGaAsP technology because most applications of DBR mirrors are in laser sources and those require an active material system. Since the largest application field of laser sources and (complex-) PICs is (still) in the telecommunication market, the InP material system is the most interesting.

1.3 DBR mirrors in PICs

The fabrication of DBR mirrors in InP is challenging, especially when the mirrors should be integrated with other components to create a complex circuit. However, the DBR mirrors are versatile components and can be applied anywhere in a PIC. This creates a lot of interesting opportunities, for example creating laser cavities with a very accurate mode-spacing. It is therefore worthwhile putting effort in developing a fabrication process that is capable of integrating the DBR mirrors and other circuit components in the same chip.

Surface gratings

Until recently, most DBR mirrors were realized by e-beam lithography or laser-interferometer lithography and selective wet-etching processes. An example for such a surface grating is shown in figure 1.2. The grating amplitude is determined by the etch depth, which is generally quite small. To obtain a reasonable refractive index difference, the grating is formed just above or beneath the waveguide layer. This means that the etching is done before the last growth steps. This puts extra restrictions on the etching process, since the growth process requires high quality surfaces without crystal damage.
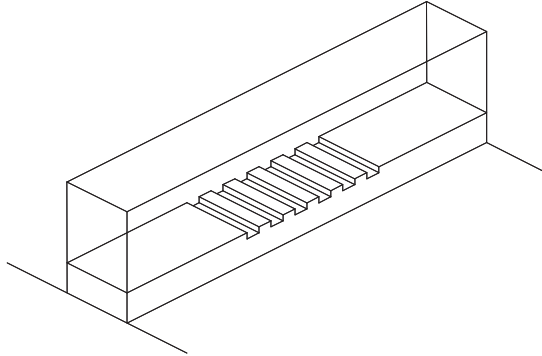
Figure 1.2: Schematic drawing of a low index-difference surface grating. The grating is placed on top of the waveguide layer. Afterwards the top cladding is grown and the waveguide is etched to the bottom of the waveguide layer.

The application of this type of surface grating is found mostly in DFB lasers and tunable DBR lasers. In a DFB laser, the grating is applied in the active part of the chip. DFB lasers are mainly used as fixed wavelength lasers for communication applications due to their high side-mode suppression ratio (SMSR), high output power and narrow line width [7]. Although the lasing wavelength can be tuned by changing the temperature of the device, the tuning range in not very large (<5 nm) and is usually only used for fine-tuning.

A much broader tuning range (>40 nm) can be obtained when using the DBR mirrors in the passive part of the chip. The DBR mirrors reflect only a narrow wavelength range, thus creating a single mode laser. The reflection band can be changed using current injection. Nowadays this is the preferred technique to create widely tunable lasers. A good overview of the different device designs can be found in [5] and [6].

Vertical Groove gratings
Recently work has been done on creating the mirrors after all the growth steps have been completed. By changing the waveguide width as shown in figure 1.3, a so-called Vertical-Groove (VG) grating is obtained. In a VG grating the amplitude of the refractive index modulation can be larger as compared to a surface grating. Although the VG grating requires a high-quality dry-etching process, it is still attractive because it offers design flexibility as well. For example, a variation of the grating depth along the propagation axis can be applied, which is not possible with surface gratings. This allows the use of apodization techniques to tune the shape of the reflection spectrum [12,13].
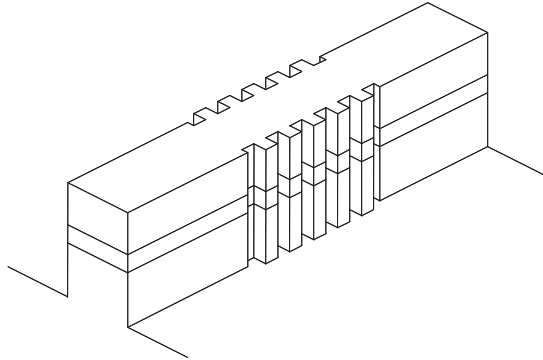
Figure 1.3: Schematic drawing of a vertical groove grating. The grating is etched together with the waveguide through the waveguide layer. The grating depth is determined by (e-beam) lithography and can be varied along the waveguide.

Vertical Groove gratings can be used in similar applications [14,15,16] as the surface gratings described above. An example of using the VG gratings as mirrors to create a short-cavity laser is shown in chapter 3 of this thesis.

Deeply etched DBR mirrors
The main focus of this thesis is on the application of a third type of mirror: deeply etched DBR mirrors. A schematic picture of a deeply etched DBR mirror is shown in figure 1.4. The deeply etched mirror has the highest possible reflection per period of all the DBR mirror types. It therefore results in the shortest mirrors with the largest reflection bandwidth. It is therefore a suitable replacement for cleaved facet mirrors, with the advantage that they can be placed anywhere on the chip.
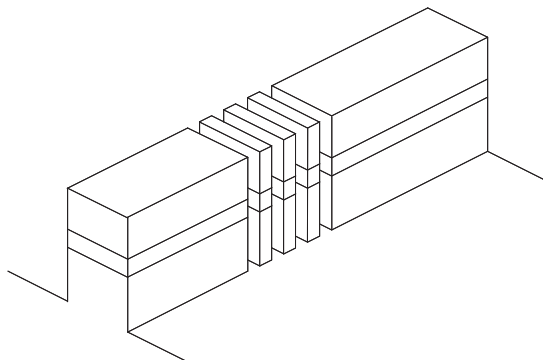
Figure 1.4: Schematic drawing of a deeply-etched DBR grating. The grating is etched together with the waveguide through the waveguide layer.

Several research groups have done work on the fabrication of these type of DBR mirrors [17,18,19,20,21,22,23]. Almost all groups were focusing on making small laser devices with

low threshold currents. Both InGaAs/AlGaAs and InGaAsP/InP are popular material systems for this purpose. Cavity lengths down to only 12 μm[24] and threshold currents down to just 1.2 mA[25] in CW operation have been reported for quantum dot based devices. However, there are only very few publications on using deeply-etched DBR mirrors in more complex PICs. Realizing the DBR gratings in combination with other building blocks adds more complexity to the fabrication process. This will be addressed in this thesis.

1.4 Structure of this thesis

The research described in this thesis focuses on realizing deeply etched DBR gratings in InP-based PICs. It covers DBR theory, simulation models, fabrication processes, characterization methods and finally shows an example of an application of DBR mirrors in a novel tunable laser device.

Chapter 2 of this thesis describes the design and simulation of DBR gratings. It covers basic grating theory as found in the literature and describes several simulation models that can be used to design different types of gratings.

In chapter 3 a short-cavity DBR laser using Vertical Groove gratings is presented. This work has been carried out at the Advanced Opto-electronics group of NTTs Photonics Laboratories. It has been published in Photonics Technology Letters [26] and briefly covers the aspects of making a DBR laser in InP technology.

The fabrication process that was developed to integrate deep etched DBR gratings in a generic integration technology is described extensively in chapter 4. It covers the progress in etching processes, e-beam lithography and planarization issues that was necessary to be able to integrate the new DBR mirrors with the existing components used in complex integrated circuits.

Chapter 5 describes the first realizations of deeply-etched DBR mirrors with this fabrication technology. It covers DBR mirrors in deeply-etched passive waveguides and two types of DBR lasers: fully deeply-etched lasers and shallow-deep etched lasers. The main focus of this chapter is on characterization methods developed to analyze the behavior of the DBR mirrors in these different configurations.

In chapter 6 all the work described before comes together in a novel Integrated Filtered Feedback Tunable Laser (IFF-TL) device. This devices demonstrates the realization of a full active-passive PIC with deeply etched DBR mirrors. It covers device design and characterization and shows the powerful new possibilities that can be obtained with deeply etched DBR mirrors integrated with other active and passive components on a single chip.

The final chapter gives a summary and conclusion of the work covered by this thesis.

Chapter 1

References

1 M. Abrams, P.C. Becker, Y. Fujimoto, V. O'Byrne, D. Piehler, "FTTP deployments in the United States and Japan-equipment choices and service provider imperatives," Journal of Lightwave Technology, vol.23, no.1, pp. 236-246, Jan. 2005

2 T.L. Koch, U. Koren, "Semiconductor photonic integrated circuits," IEEE Journal of Quantum Electronics, vol.27, no.3, pp.641-653, Mar 1991

3 M.K. Smit, M.T. Hill, R. Baets, E.A.J.M. Bente, H.J.S. Dorren, F. Karouta, P.M. Koenraad, A.J.M. Koonen, X.J.M. Leijtens, R. Nötzel, Y.S. Oei, H. de Waardt, J.J.G.M. van der Tol, G.D. Khoe, "How complex can integrated optical circuits become?" Proc. 13th Europ. Conf. on Integrated Optics (ECIO 2007) Copenhagen, Paper ThPT2

4 A. D. Kersey, T. A. Berkoff, and W. W. Morey, "Multiplexed fiber Bragg grating strain-sensor system with a fiber Fabry - Perot wavelength filter," Opt. Lett. 18, pp. 1370, 1993

5 L.A. Coldren, G. A. Fish, Y. Akulova, J. S. Barton, L. Johansson, and C. W. Coldren, "Tunable Semiconductor Lasers: A Tutorial," J. Lightwave Technol. 22, pp. 193, 2004

6 H.G. Bukkems, "New approaches to widely tunable semiconductor lasers," PhD thesis, Technische Universiteit Eindhoven, Eindhoven, The Netherlands, 2006. ISBN 90-386-1793-3

7 G. Morthier, P. Vankwikelberge, "Handbook of distributed feedback laser diodes," Boston: Artech House, 1997

8 Y.P. Li, C.H. Henry, "Silica-based optical integrated circuits," Optoelectronics, IEE Proceedings, vol.143, no.5, pp.263-280, Oct 1996

9 F. Morichetti, A. Melloni, M. Martinelli, R.G. Heideman, A. Leinse, D.H. Geuzebroek, A. Borreman, "Box-Shaped Dielectric Waveguides: A New Concept in Integrated Optics?," Journal of Lightwave Technology, vol.25, no.9, pp.2579-2589, Sept. 2007

10 W. Bogaerts, D. Taillaert, B. Luyssaert, P. Dumon, J. Van Campenhout, P. Bienstman, D. Van Thourhout, R. Baets, V. Wiaux, and S. Beckx, "Basic structures for photonic integrated circuits in Silicon-on-insulator," Opt. Express 12, 1583-1591 (2004)

11 G. Roelkens, D. Van Thourhout, R. Baets, R. Nötzel, and M. Smit, "Laser emission and photodetection in an InP/InGaAsP layer integrated on and coupled to a Silicon-on-Insulator waveguide circuit," Opt. Express 14, 8154-8159 (2006)

12 M.J. Strain, M. Sorel, "Integrated III–V Bragg Gratings for Arbitrary Control Over Chirp and Coupling Coefficient," IEEE Photonics Technology Letters, vol.20, no.22, pp.1863-1865, Nov.15, 2008

13 T. Segawa, S. Matsuo, Y. Ohiso, T. Ishii, H. Suzuki, "Apodised sampled grating using InGaAsP/InP deep-ridge waveguide with vertical-groove surface grating," Electronics Letters , vol.40, no.13, pp. 804-805, 24 June 2004

14 J. Wiedmann, K. Ebihara, H.C. Kim, B. Chen, M. Ohta, K. Matsui, S. Tamura, J.I. Shim, S. Arai, "1.5 μm wavelength distributed reflector lasers with vertical grating," Electr. Lett., vol.37, no.13, pp.831-832, Jun 2001

15 M. Gnan, H.M.H. Chong,C.S. Kim, A.C. Bryce, M. Sorel, R.M. De La Rue, "Coupled microcavity in photonic wire Bragg grating," Conf. on Lasers and Electro-Optics, 2004. (CLEO), vol.1, no., pp.2 pp. vol.1-, 16-21 May 2004

16 K. Mathwig, W. Kaiser, A. Somers, J.P. Reithmaier, A. Forchel, K. Ohira, S.M. Ullah, S. Arai, "DFB Lasers With Deeply Etched Vertical Grating Based on InAs–InP Quantum-Dash Structures," IEEE Photonics Technology Letters, vol.19, no.5, pp.264-266, March, 2007

17 T. Baba, M. Hamasaki, N. Watanabe, P. Kaewplung, A. Matsutani, T. Mukaihara, F. Koyama, K. Iga, "A Novel Short-Cavity Laser with Deep-Grating Distributed Bragg Reflectors", Jpn. J. Appl. Phys., Vol. 35, 1996

18 Y. Yuan, T. Brock, P. Bhattacharya, C. Caneau, R. Bhat, "Edge-emitting lasers with short-period semiconductor/air distributed Bragg reflector mirrors," IEEE Phot. Tech. Letters, vol.9, no.7, pp.881-883, 1997

19 E. Hofling, F. Schafer, J.P. Reithmaier, A. Forchel, "Edge-emitting GaInAs-AlGaAs microlasers," IEEE Photonics Technology Letters, IEEE , vol.11, no.8, pp.943-945, Aug 1999

20 M.M.Raj, S. Toyoshima and S. Arai, "Multiple Micro-Cavity Laser with Benzocyclobutene/Semiconductor High Reflective Mirrors Fabricated by CH4/H2-Reactive Ion Etching", Jpn J Appl Phys 2, Vol.38, No.7B 1999

21 K. Avary, S. Rennon, F. Klopf, J. P. Reithmaier, A. Forchel, "Reactive ion etching of deeply etched DBR-structures with reduced air-gaps for highly reflective monolithically integrated laser mirrors," Microelectronic Engineering, Volumes 57-58, September 2001

22 L. Raffaele, R.M. De La Rue and T.F. Krauss, "Ultrashort in-plane semiconductor microlasers with high-reflectivity microstructured mirrors", Optical and Quantum Electronics, Vol. 34, No. 1-3 / Jan 2002

23 H.C. Kim, H. Kanjo, T. Hasegawa, S. Tamura, S. Arai, "1.5-µm wavelength narrow stripe distributed reflector lasers for high-performance operation," IEEE Journal of Selected Topics in Quantum Electronics, vol.9, no.5, pp. 1146-1152, Sept.-Oct. 2003

24 S. Rennon, F. Klopf, J.P. Reithmaier, A. Forchel, "12 µm long edge-emitting quantum-dot laser," Electronics Letters, vol.37, no.11, pp.690-691, 24 May 2001

25 S. Rennon, K. Avary, F. Klopf, J.P. Reithmaier, A. Forchel, "Edge-emitting microlasers with one active layer of quantum dots," IEEE J. of Selected Topics in Quantum Electronics, vol.7, no.2, pp.300-305, Mar/Apr 2001

26 B. Docter, T. Segawa, T. Kakitsuka, S. Matsuo, T. Ishii, Y. Kawaguchi, Y. Kondo, H. Suzuki, F. Karouta, M.K. Smit, "Short Cavity DBR Laser Using Vertical Groove Gratings for Large-Scale Photonic Integrated Circuits," IEEE Photonics Technology Letters, vol.19, no.19, pp.1469-1471, Oct 2007
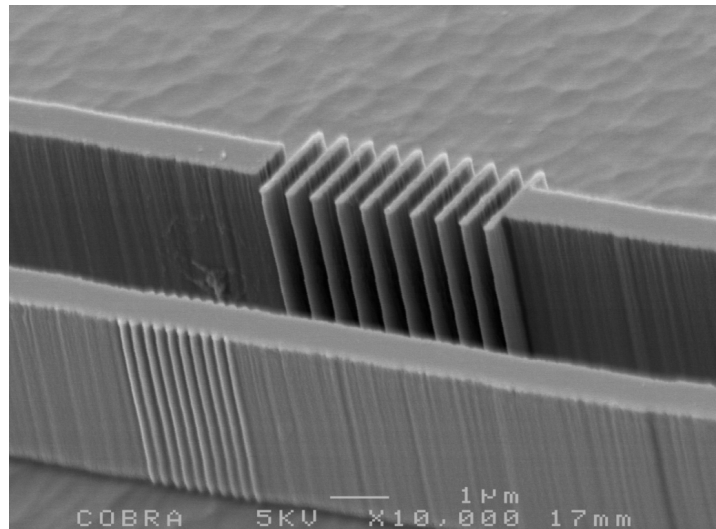
"Gratings in waveguides"

VG grating (front) and deeply-etched grating (rear) in two waveguides.
Realized with an Aluminum lift-off process using e-beam lithography.

2 Grating theory - simulation & design

2.1 Introduction

This chapter reviews the most common theories and simulation methods to describe light propagation in periodic structures. Initially in section 2.2 we will follow the same coupled mode approach as given in [1, chapter 3]. This approach is valid for gratings in waveguides with small variation in refractive index (i.e. small etch depths in surface gratings or small variation of waveguide width in the case of vertical groove gratings).

However, if the mode shape in the different sections of the grating varies too much (e.g. larger etch depths), the overlap between the fields in the consecutive sections has to be taken into account as well, because mode conversion and coupling losses can play a bigger role. For this a bi-directional eigenmode propagation tool is more suitable. This is described in section 2.3.

For the deeply-etched gratings, where the grating slits are etched all the way through the waveguide layer and no waveguiding structure is left between the semiconductor sections, a robust Finite Difference Time Domain (FDTD) approach is often required. Although these calculations require quite some computational resources, the results give information on the grating performance over a wide spectral range. 3D FDTD calculations are described in section 2.4.

Unless stated otherwise, the wavelength used for the simulations in this chapter is 1.55 µm and the polarization is Transverse Electric (TE). The reason is that we focus on applications of DBR gratings for telecommunication lasers and the chosen wavelength is in the center of the commonly used C-band (1530-1570 nm). Additionally, the optical gain medium used in this work has a higher gain for TE polarized light and therefore lasers fabricated in this material usually only operate in the TE polarization state.

2.2 Coupled mode theory

The coupled mode theory is the most common way to study the behavior of light propagating through long periodic structures. In the following section we will consider a general situation where there is a waveguide with an effective index N_{eff}. The grating is modeled with a periodic change of the effective index given by Δn, so the refractive index as a function of the propagation axis z is given by:

$$n(z) = N_{eff} + \Delta n \quad for \quad n\Lambda \leq z < \left(n + \tfrac{1}{2}\right)\Lambda$$
$$n(z) = N_{eff} - \Delta n \quad for \quad \left(n + \tfrac{1}{2}\right)\Lambda \leq z < (n+1)\Lambda$$

(2.1)

with n an integer and Λ the period of the grating.

This structure is shown schematically in figure 2.1.

11
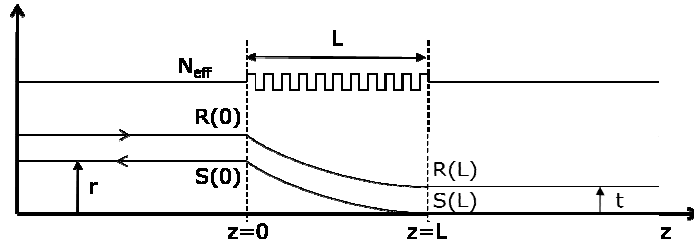
Figure 2.1: Schematic picture of the effective index variation as a function of the propagation direction z. Also the forward (R(z)) and backward (S(z)) field amplitudes are shown.

The reflection coefficient for an incident field at one of the grating interfaces is given by the Fresnel formula, which results in:

$$r = \frac{\pm \Delta n}{2 N_{eff}}$$
(2.2)

Note that the reflection coefficient is negative for a low-to-high transition, but positive for a high-to-low transition.

At the Bragg wavelength, where the reflection is maximum, the following relation is satisfied:

$$m \lambda_B = 2 \Lambda N_{eff}$$
(2.3)

in which m is the order of the grating and Λ is the grating period. Because at the Bragg wavelength the total phase change within one period of the grating is 180 degrees due to the propagation and 180 degrees due to the phase jump at the low-to-high index interface, all the reflections in the grating add up in phase. This is valid for a so-called 1st order grating, where the period Λ equals half a wavelength in the specific medium ($\Lambda = \frac{1}{2} \cdot \lambda_B / N_{eff}$). In a 2nd order grating, where $\Lambda = \lambda_B / N_{eff}$, the reflections are exactly anti-phased, resulting in minimal reflection. A 3rd order design results in a high reflection again and so forth.

The total reflection per unit length for a 1st order grating is given by:

$$\kappa = \frac{2|r|}{\Lambda} = \frac{2 \Delta n}{\lambda_B}$$
(2.4)

κ is called the coupling coefficient of the grating and is usually given per cm ($[cm^{-1}]$). It can be used to describe the forward and backward propagating fields in the form of two coupled mode equations. First we write the field in the structure as the sum of forward (R) and backward (S) propagating waves:

$$E(z) = R(z)e^{-j\beta z} + S(z)e^{j\beta z} \qquad \textbf{(2.5)}$$

See also figure 2.1. β is the propagation constant, which is given by $k \cdot N_{eff}$ with $k=2\pi/\lambda$. Then we use the coupling coefficient κ to relate the forward and backward propagating waves:

$$\frac{dR}{dz} + j\Delta\beta R = -j\kappa S \qquad \textbf{(2.6)}$$

$$\frac{dS}{dz} - j\Delta\beta S = j\kappa R \qquad \textbf{(2.7)}$$

where $\Delta\beta$ is the deviation of the propagation constant to the propagation constant at the Bragg wavelength:

$$\Delta\beta = \beta - \frac{2\pi}{\lambda_B} N_{eff} \qquad \textbf{(2.8)}$$

When the amplitude of the two travelling waves at z=0 are known, the solution of the coupled mode equations can be written as follows:

$$R(z) = \left[\cosh(\gamma z) - \frac{j\Delta\beta}{\gamma}\sinh(\gamma z)\right]R(0) - \frac{j\kappa}{\gamma}\sinh(\gamma z)S(0) \qquad \textbf{(2.9)}$$

$$S(z) = \frac{j\kappa}{\gamma}\sinh(\gamma z)R(0) + \left[\cosh(\gamma z) + \frac{j\Delta\beta}{\gamma}\sinh(\gamma z)\right]S(0) \qquad \textbf{(2.10)}$$

where γ is defined as:

$$\gamma^2 = \kappa^2 - \Delta\beta^2 \qquad \textbf{(2.11)}$$

With this result we can describe the transmission and reflection from a grating of length L by the following F-matrix notation [2]:

$$\begin{bmatrix} R(L) \\ S(L) \end{bmatrix} = F_{per}(L) \cdot \begin{bmatrix} R(0) \\ S(0) \end{bmatrix} \qquad \textbf{(2.12)}$$

where the matrix elements are:

$$F_{per,11} = \cosh(\gamma L) - \frac{j\Delta\beta}{\gamma}\sinh(\gamma L)$$

$$F_{per,12} = -\frac{j\kappa}{\gamma}\sinh(\gamma L)$$

$$F_{per,21} = \frac{j\kappa}{\gamma}\sinh(\gamma L)$$

$$F_{per,22} = \cosh(\gamma L) + \frac{j\Delta\beta}{\gamma}\sinh(\gamma L)$$

(2.13)

This F-matrix notation is very useful because it relates the incoming and outgoing fields at one end of a grating structure to the incoming and outgoing fields at the other end. It can therefore be used as a transfer matrix to connect the grating to other components in a circuit. It is also useful to study gratings consisting of multiple sections like super-structure gratings [3] and gratings that have a varying grating shape along the propagation axis [4].

The transmission t of a single grating of length L is defined by $R(L)=t\cdot R(0)$, which straightforwardly leads to:

$$t = F_{per,11} = \cosh(\gamma L) - \frac{j\Delta\beta}{\gamma}\sinh(\gamma L)$$

(2.14)

Analogously the reflection r is defined by $S(0)=r\cdot R(0)$. When there is no field entering the grating from the rear side (e.g. $S(L)=0$, as shown in figure 2.1), using equation 2.10 the reflection r can be described as:

$$r = \frac{S(0)}{R(0)} = \frac{-F_{per,21}}{F_{per,22}} = \frac{-\frac{j\kappa}{\gamma}\sinh(\gamma L)}{\cosh(\gamma L) + \frac{j\Delta\beta}{\gamma}\sinh(\gamma L)}$$

(2.15)

Note that these are field reflectivity and transmission values. To obtain the power reflectivity the values should be squared ($R=r^2$, $T=t^2$). To include losses into the equations, β should be replaced by β-ja and $\Delta\beta$ by $\Delta\beta$-ja, where a is the field loss coefficient, which is half the value of the more commonly used power loss coefficient.

A typical reflection and transmission spectrum of a grating is given in figure 2.2
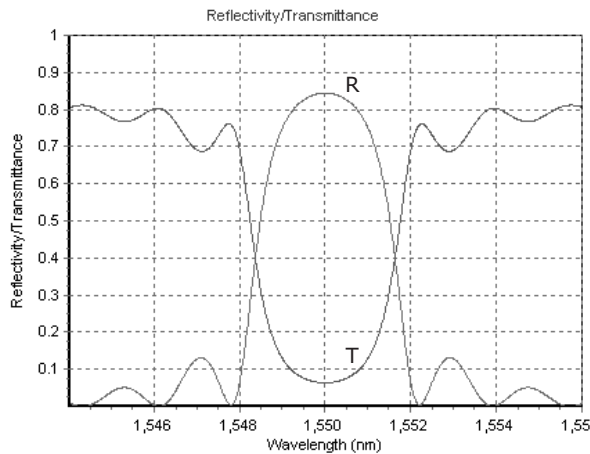
Figure 2.2: Typical reflection (R) and transmission (T) spectrum of a grating of 200 μm long, κ = 100 cm⁻¹ and a = 10 cm⁻¹.

The amplitude of the reflection, at the Bragg wavelength ($\Delta\beta=0$) and assuming no losses is given by:

$$|r| = \tanh(\kappa L)$$

(2.16)

which shows nicely that the peak reflectivity depends on the coupling coefficient times the grating length, but saturates at a certain length. When the propagation losses in the grating are taken into account, the maximum reflectivity is reduced. This is shown in figure 2.3, where the peak reflectivity is plotted as a function of the grating length. The graph shows the reflectivity saturation. When a certain length is reached, increasing the grating length further does not increase the reflectivity anymore.
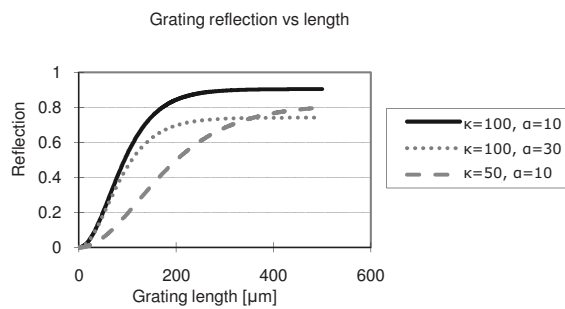
Figure 2.3: Peak reflection as a function of grating length, for different coupling coefficients and propagation losses.

15

When designing a laser cavity using these long mirrors it is often necessary to know how far the light penetrates into the grating mirror, since this will determine the total cavity length and therefore the modespacing. From the solution of the coupled mode equations it is possible to find the point at which the incoming power has decreased by a factor of e. This point is defined as the effective length (L_{eff}) of the grating and is given by the following expression [1]:

$$L_{eff} = \frac{\tanh(\kappa L)}{2\kappa} = \frac{L}{2}\frac{\tanh(\kappa L)}{\kappa L} \qquad\qquad \textbf{(2.17)}$$

which means that for small values of κL (e.g. small etch depth or short gratings) the effective length is equal to *L/2*, while for large values of κL (reflection is saturated) L_{eff} = *1/(2κ)*. The effective length is used to determine the effective cavity length of a DBR laser with long grating mirrors in chapter 3.

Another important design parameter is the bandwidth of the grating. For long gratings the bandwidth mainly depends on the coupling coefficient. This can be understood intuitively by the fact that the light penetrates the grating further when the coupling coefficient is smaller. Therefore more reflections add up to form the total reflection and consequently a deviation from the Bragg wavelength causes a larger phase mismatch.

This behavior is confirmed by the calculation shown in figure 2.4, where the relation between bandwidth and coupling coefficient is plotted for a 400 µm long grating using the transmission formula shown in equation 2.14. This grating length is also used later on in chapter 3 to characterize the grating performance. Note that the curve is linear for larger values of κ, but for small coupling coefficients the bandwidth reduces to 0 very rapidly. This is due to the limited length of the grating. The relation plotted in figure 2.4 can be used to determine the coupling coefficient from a measured transmission spectrum, as will be shown in section 3.3.2.
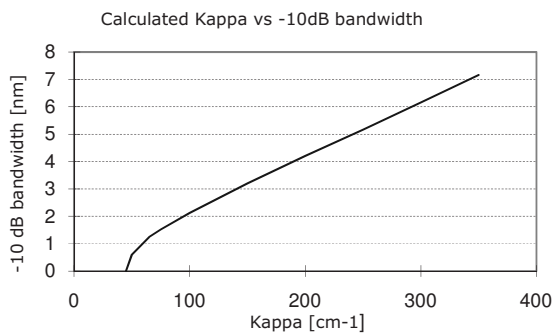
Figure 2.4: Relation between coupling coefficient κ and transmission bandwidth.

2.3 Eigenmode propagation methods

The coupled mode theory is a very fast method to calculate the effect of the refractive index variation on the reflection spectrum. It can also be used efficiently to study how apodization techniques [5] change the shape of the reflection spectrum. However, when the grating depth increases, the shapes of the guided modes in each grating section vary more. Therefore when the grating depth becomes larger a method that takes these shapes into account is required.

Eigenmode propagation methods can be used for this purpose. A schematic picture of the working principle is shown in figure 2.5. The method decomposes a field in a waveguide structure into a complete set of forward and backward propagating modes. Non-guided radiating modes are also taken into account. When for each section the modes are known, the method calculates the overlap between all the modes at the interface between two sections. Then the amplitude and phase of all the modes are calculated such that the field and its z-derivative (for TE polarization; for TM, the z-derivative divided by the relative dielectric constant) is continuous everywhere. Because the forward and the backward propagating modes are taken into account, this automatically results in the reflection at the interface.
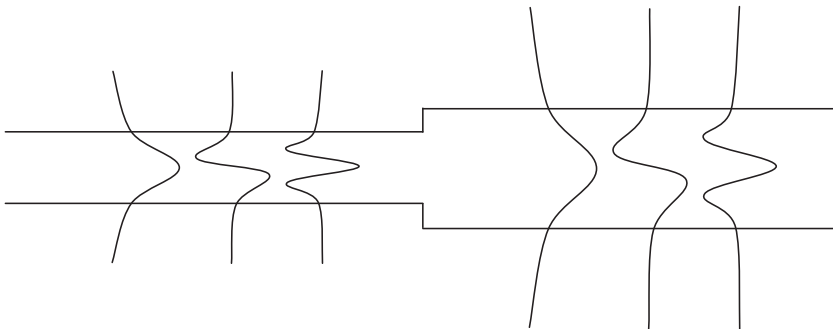
Figure 2.5: Modal decomposition in a 2-section waveguide structure.

The Eigenmode propagation method assumes that the field can be decomposed into a limited set of modes and that the mode set is complete. In order to make sure that no (radiating) modes are missed, the number of modes should be chosen high, much higher than just the modes that are supported by the waveguide structure. The exact amount of modes depends on the simulation structure and calculation window. In our case, when the waveguide width is usually 0.5-3.0 µm wide and the total calculation window is relatively small (<10 µm), 50 to 100 modes are usually sufficient. The calculation time scales quadratically with the number of modes.

The calculation window is bordered by Perfectly Matched Layers (PMLs) that suppress light that hits the calculation window edges. The settings of the PMLs should be chosen such that

17

light does not reflect from the calculation window borders. However, the if the absorption of the PMLs (PML strength) is set too high, it can disturb the calculation of the Eigenmodes. If this is the case, enlarging the calculation window usually provides a solution.

2.3.1 BEP simulations on VG gratings

In the following section the Bi-directional Eigenmode Propagator (BEP) algorithm as implemented in the OlympIOs design and simulation software [6] was used to perform calculations on vertical groove (VG) gratings (see figure 1.3 for a schematic picture). This program uses a 1D approach to calculate the modes and therefore an effective index method was used to reduce the 2D cross-section of the deeply-etched waveguides into a 1D slab equivalent, as shown in figure 2.6. When doing top-view calculations, the waveguide layer stack (InP/Q1.25/InP) is converted into an effective index equivalent (*Neff_WG*). The effective index depends on the layer thicknesses, but these are fixed in the case of VG gratings. The value shown in the figure can therefore be used throughout the structure.

In the calculations performed in the rest of this chapter we assume that the waveguides are planarized by a polymer called BenzoCycloButhene (BCB). This polymer has a refractive index of 1.539. The BCB is also present in the grating gaps.

n_BCB	1.539
n_InP	3.169
n_Q1.25	3.364
Neff_WG	3.264
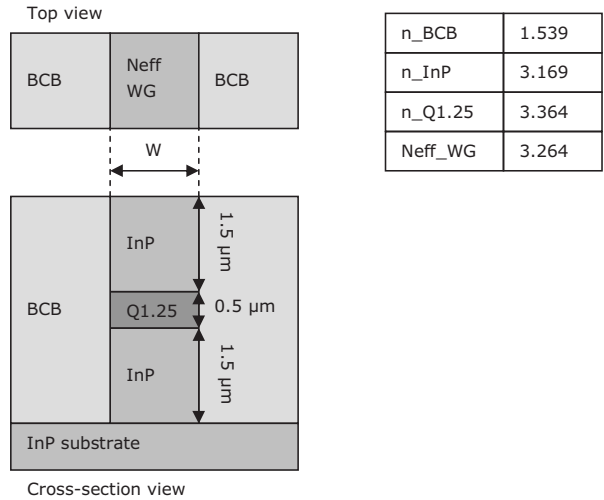
Figure 2.6: Effective index method to reduce 2D waveguide cross-section to 1D equivalent.

figure 2.7 shows a top view schematic of the analyzed VG grating structure. All the relevant design parameters are given. W is the waveguide width, Λ the grating period which equals $L_1 + L_2$, which are the lengths of the wide and narrow grating sections. D_g is the grating depth.
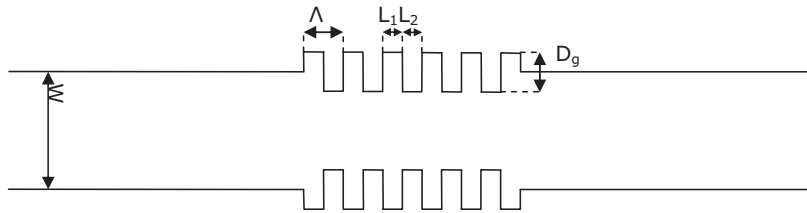
Figure 2.7: VG grating structure (top-view).

In many studies on DBR gratings with a low index contrast between the grating elements, the length of each grating section is the same ($L_1=L_2$). This length is then taken as $L=\frac{1}{4}*\lambda/N_{eff}$, where N_{eff} is the effective index of the waveguide without grating. However, in the case of higher index contrasts, it is better to choose a more appropriate value of $L_i=\frac{1}{4}*\lambda/N_{eff,i}$ where $N_{eff,i}$ is the effective index of each grating section.

A typical simulation result is given in figure 2.8. The simulated structure has the following parameters: $W = 1.0$ µm, $D_g = 0.2$ µm, 100 periods. Some conversion into higher order modes is clearly visible. This is due to the different shape of the guided modes in the different grating sections. Such an effect would not be observed when using the coupled mode theory described in the previous section.
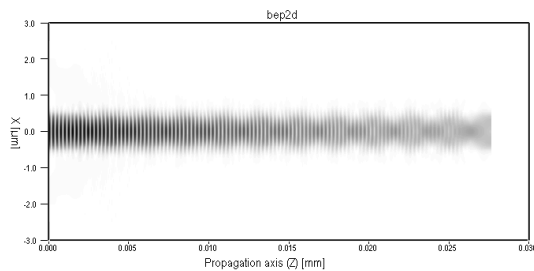
Figure 2.8: Calculated field intensity in a VG grating using the 2D BEP algorithm

When we plot the reflection for different waveguide widths as a function of the relative grating depth (D_g/W), we see that the reflection rises linearly, but then drops after a certain maximum (figure 2.9). The graph in figure 2.10 shows the field of the 1.0 µm wide waveguide with a grating depth of $D_g=0.8$ µm. Conversion to the second order mode is

clearly visible. In fact, 19% of the reflected light is coupled into a guided 2nd order mode in this particular case.
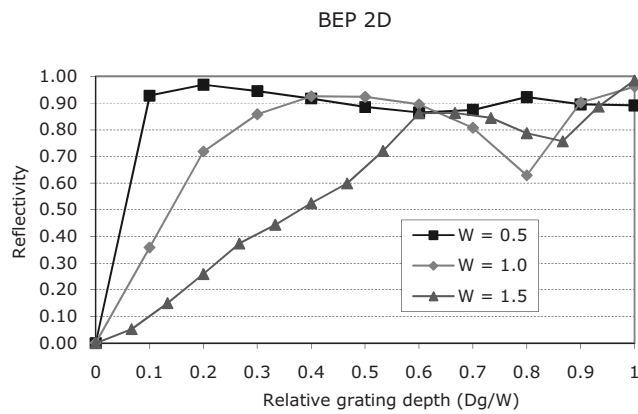
Figure 2.9: Reflectivity of a 100 period long VG grating, varying waveguide width and relative grating depth.
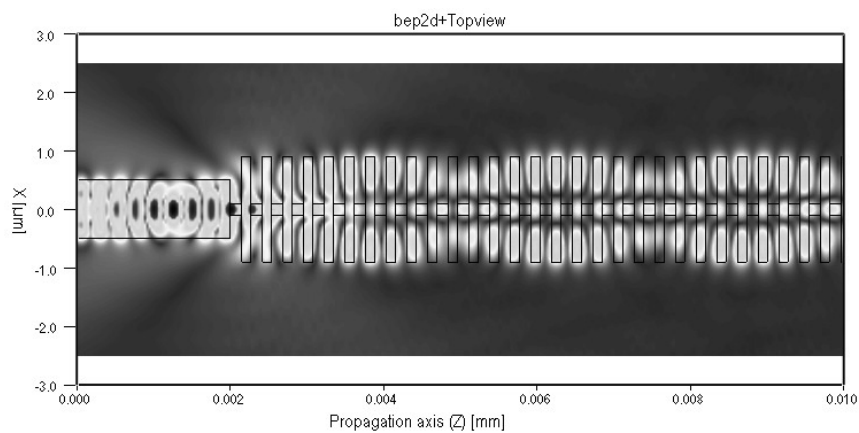
Figure 2.10: Field plot and structure of a VG grating with a waveguide width of 1.0 μm and a grating depth D_g=0.8 μm.

The conclusion from these simulations is that excitation of higher order modes can easily occur, deteriorating the reflectivity of the grating. When a high reflection in a small number of periods is required, it is better to reduce the waveguide width, rather than to increase the grating depth.

2.3.2 BEP simulations on deeply-etched gratings

In the extreme case of a vertical groove grating with a grating depth equal to the waveguide width ($D_g=W$), the structure becomes almost identical to a deeply-etched grating, shown in figure 2.11. The difference is that in the deeply etched gratings the high-index parts have the same width as the waveguide. In the following sections we will concentrate on these deeply etched gratings.
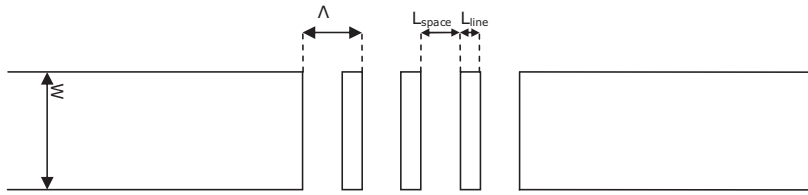
Figure 2.11: Deeply-etched grating structure (top-view).

Figure 2.12 shows the calculated reflectivity and transmission of a single period grating (one etched space, no line), as a function of L_{space}. There is a maximum in the reflectivity when the etched gap is 250 nm long. This corresponds to $L_{space} = ¼*λ/n_{BCB} = ¼*1.55/1.54$, which we call a 1st order grating. Normally we would expect the next maximum to be at 750 nm, corresponding to a 3rd order grating. However, from the plot we can see that the optimum occurs at a slightly longer gap length of approximately 780 nm. These small differences will be further investigated using 3D calculations later in this chapter.
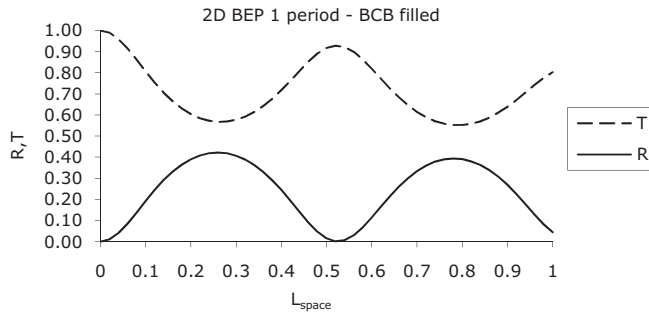
Figure 2.12: 2D BEP calculation of the reflectivity (R) and transmission (T) of a single-period deep etched grating filled with BCB as a function of the length of the etched gap.

Although the reflection per period is higher in the case of a 1st order grating, a 3rd order grating is easier to fabricate. To further investigate the impact of moving from a 1st order grating to a 3rd order grating we perform simulations on the DBR reflectivity as a function of the number of grating periods, the etch depth and deviations due to fabrication tolerances.

The result for the reflectivity (R) and the transmission (T) as a function of the number of grating periods is shown in figure 2.13. It shows that the reflectivity is slightly lower for a 3rd order grating compared to a 1st order grating, while the transmitted light is more or less the same. This indicates higher diffraction losses.
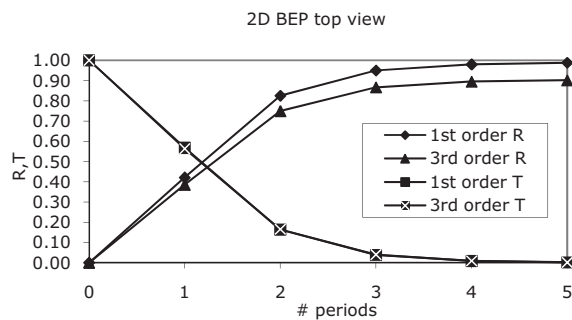
Figure 2.13: Reflectivity (R) and transmission (T) of 1st and 3rd order gratings as a function of the number of grating periods.

To study the etch depth dependence the orientation of the calculation window was changed from top-view to side-view. Similar to the top-view calculations an effective index method was used to reduce the 3D structure to a 2D structure. The waveguide width that was used in these calculations is 1 μm.

The graph in figure 2.14, showing the reflectivity as a function of the etch depth shows that the waveguide should be etched at least 1 μm through the waveguide layer (total etch depth of 3 μm) in order to obtain the highest reflectivity. This is due to light being coupled to substrate modes [7].
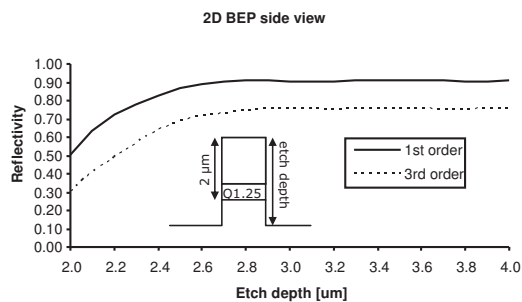
Figure 2.14: Reflectivity as a function of etch depth.

The plots in figure 2.15 show the tolerance on the fabrication of the DBR gratings as predicted by the top-view simulations. In the contour plot on the left the areas where there

is high reflectivity are clearly visible. As expected, when the lines become a little bit smaller or wider due to fabrication imperfections, the spaces have to be compensated in the opposite manner, in order to keep the period of the grating constant. These are actually the most common fabrication errors, since a small change in the dose of the e-beam writing process would result in a change in the line/space ratio, but not in the grating period.

The cross-section plots at the right show the reflectivity at the theoretical optimum line lengths for a 1st and a 3rd order grating. The reflection peak around L_{space}=750 nm is slightly narrower than the reflection peak around L_{space}=250 nm. This shows that a 3rd order grating is slightly more sensitive to fabrication imperfections.
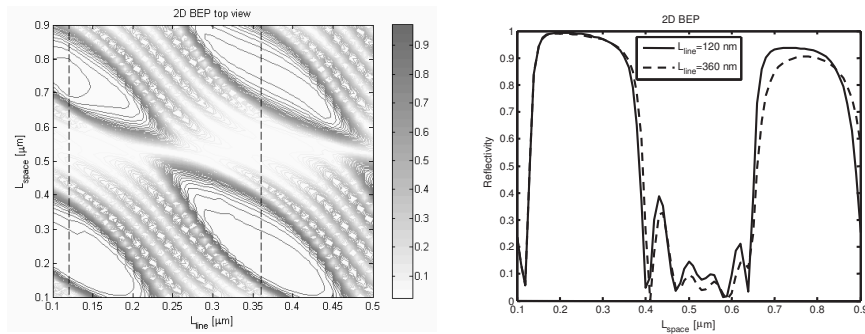
Figure 2.15: Contour plots of the DBR reflectivity of a 5 period deeply etched grating as a function of L_{line} and L_{space} (left figure). The figure on the right shows cross-sections of the contour plots at L_{line}=120 nm (1st order grating) and L_{line}=360 nm (3rd order grating), as indicated by the dashed lines in the left figure.

This section described the use of 2D bi-directional eigenmode propagation methods to investigate the design of vertical groove- and deeply etched gratings. It is shown that the method is suitable for scanning many design parameters as a single calculation does not require much computational power. However, the diffraction of the light in the non-guided areas is only taken into account in one direction. To assess the validity of these simulations it is therefore required to check some of the most common designs with a full 3D approach. Sub-section 2.4.2 describes calculations done with a 3D FDTD method, with which also the full wavelength behavior of the DBR gratings can be studied.

2.4 Finite Difference Time Domain (FDTD) methods

The most robust way of calculating electro-magnetic fields is to directly solve Maxwell's equations. Finite Difference Time Domain (FDTD) methods [8,9] do that for a number of time-steps and for a discrete computational grid. The accuracy is therefore determined by the grid settings and the time step size.

2.4.1 2D FDTD simulations

Before moving to the full 3D FDTD simulations, first a 2D approach is used to analyze the influence of non-straight waveguide sidewalls on the reflectivity and the transmission of deeply-etched DBR gratings. The structure that is used for this calculation is shown in figure 2.16. The waveguide is modeled using a side view approach, where the effective index method is used once again to reduce the 3D structure to a 2D equivalent. A single-period DBR grating etched through the waveguide layer and filled with BCB (n=1.54). The length of the spacing (L_{space}) is defined at the top of the waveguide layer, similar to what would happen in the fabrication process. An etching angle is defined, reducing the length of the space at the waveguide level. The influence of the etching angle on the gap length at the waveguide level for a 3rd order grating filled with BCB (L_{space} = *750 nm*) is shown in the table on the right.

angle [deg]	gap [nm]
0	750
1	689
2	628
3	567
4	505
5	444
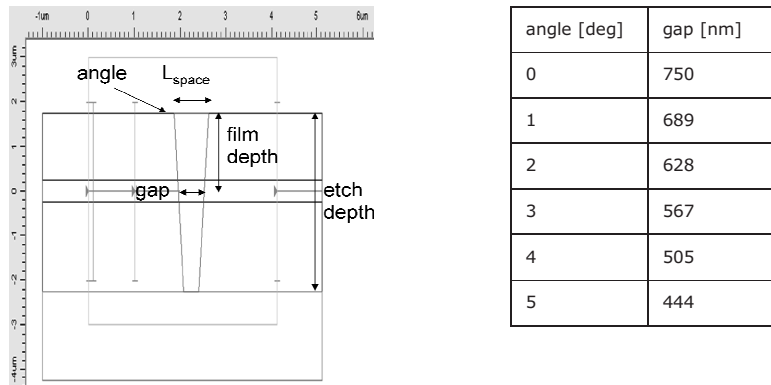
Figure 2.16: 2D side-view simulated structure used to calculate the influence of a non-straight sidewall in the DBR grating. In the table the gap lengths as a function of etching angle are given.

The simulations were performed at λ = 1.55 μm, using a CW input field. A convergence study on a structure with straight sidewalls showed that a step size of 50 nm in the propagation direction (Δz = 50 nm) as well as in the vertical direction (Δx = 50 nm) was sufficient to obtain the reflectivity and the transmission within 1% accuracy. However, since the angled side wall will be discretized by this rectangular grid, it was chosen to further reduce the step size to what was still practically feasible in terms of calculation time. The final settings were Δz = 15 nm and Δx = 25 nm.

The maximum time step for which the numerical simulation is still stable is a function of the spatial grid and is given by the following equation [9]:

$$\Delta t = \frac{1}{c\sqrt{\dfrac{1}{(\Delta x)^2} + \dfrac{1}{(\Delta y)^2} + \dfrac{1}{(\Delta z)^2}}} \qquad \textbf{(2.18)}$$

which is valid for both 2D and 3D calculations (in 2D calculations $\Delta y = \infty$). This relation leads to a step size of $\Delta t = 4.29 \cdot 10^{-17}$ s. The total simulation time must be set sufficiently long to reach a steady state, and therefore depends on the number of periods in the simulation structure. 250 fs is usually enough for a 5-period structure. For less periods the simulation time can be reduced.
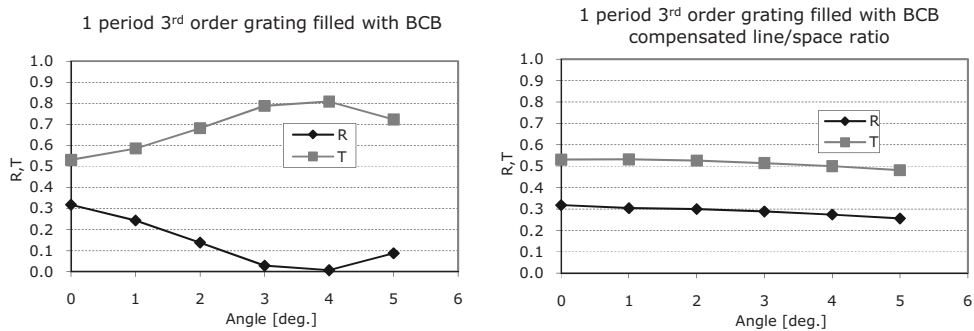
Figure 2.17: Calculated reflectivity (R) and transmitted (T) power for a single gap deep etched DBR grating filled with BCB as a function of the etching angle. The left figure shows the results when the grating dimension is not compensated for the etching angle, the right figure shows the results for the compensated structure.

The recorded transmitted (T) and reflected (R) powers as a function of the angle are shown in figure 2.17 (left figure). At an angle of 4° the gap length in the waveguide layer is reduced to 505 nm, which is almost the same as ½ * λ/n_{BCB} for λ=1.55 µm. At this length the reflected wave from the first interface is exactly anti-phased with the reflected wave from the second interface. The destructive interference causes a very low reflection at this length. However, when the etching angle is known, the grating design can be adapted to compensate for the reduction in L_{space}. The result is shown in figure 2.17, right figure. The grating design is compensated such that the length of the etched gap is exactly 750 nm at the waveguide layer. The resulting dependence of the reflectivity on the etched angle is much smaller.

The conclusion from these simulations is that when the etching angle is known and is reproducible, the design of the DBR gratings can be adjusted so that the right dimensions are obtained at the waveguide layer. In that case etching angles up to 5° can be tolerated since the effect on the peak reflectivity is small. However, for optimal performance, the etching angle should be kept as small as possible.

2.4.2 3D FDTD simulations

This section describes the 3D FDTD simulations we performed on deeply-etched DBR gratings. This is done with the commercial software package CrystalWave [10]. In the simulations a grid spacing of 25 nm is used in all directions so that small changes in the

grating shape can be taken into account. This determines the optimal (longest) time step at 4.76×10^{-17} s (see eq. 2.18). Due to limited computational resources this allows only small ($<10 \times 10 \times 5 \ \mu m^3$) structures to be analyzed within a reasonable timescale (<1 hour per calculation). The simulations are performed on a machine with a CPU clock speed of 3 GHz and 3 GB of memory installed. The total computational time required to obtain good results depends on how long a light pulse will resonate in the structure. For our 1-5 period deeply-etched DBR structures usually 5000 time steps is sufficient.

In the simulations we launch a modal field with a sinusoidal time envelope of 20 fs into the structure. We record the reflected and the transmitted light as a function of the simulation time and perform a Fourier transformation on the data. In this way we can investigate the reflection and transmission as a function of the wavelength. The bandwidth of the obtained spectra depends inversely on the duration of the input pulse. The resolution of the spectra is determined by the total computation time.
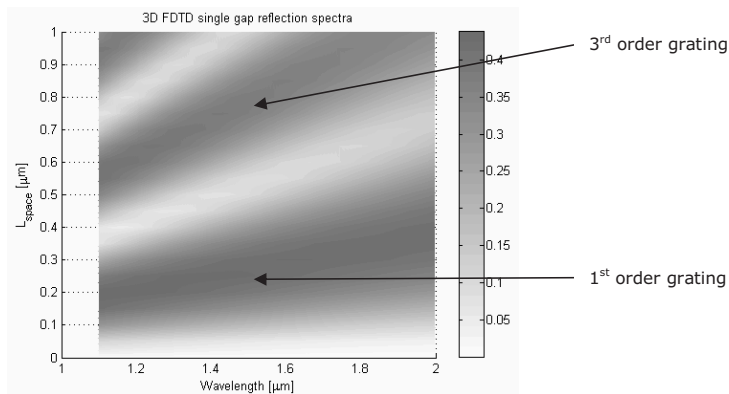
Figure 2.18: 3D FDTD calculation of the reflection spectra of a single-period deep etched grating filled with BCB as a function of L$_{space}$.

First we repeat the simulation of a single period deeply etched grating (figure 2.12) and vary the length of the etched gap, L_{space}. The spectra as a function of space length are shown in figure 2.18. The color scale shows the reflection amplitude. The color diagram shows several areas of high reflectivity corresponding to the different grating orders. Note that the area corresponding to a 3rd order grating is tilted more than the area corresponding to the 1st order grating. This indicates that the bandwidth of the 3rd order grating is smaller. This also means that the fabrication tolerance is slightly lower, since a variation in L_{space} will lead to a larger shift in reflection spectrum, compared to a 1st order grating.
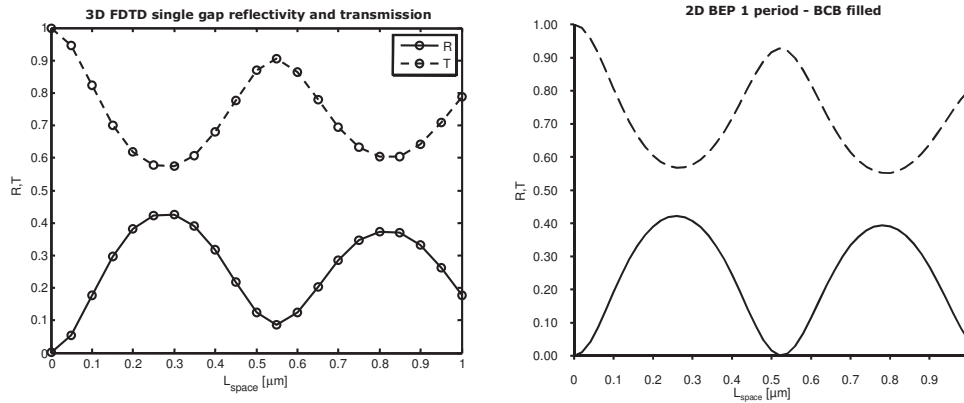
Figure 2.19: 3D FDTD calculation (left figure) of the reflectivity and transmission at λ=1.55 μm of a single-period deep etched grating filled with BCB as a function of the length of the etched gap. For comparison the results from the 2D BEP calculations (figure 2.12) are repeated as well (right figure).

Figure 2.19 shows a cross-section of the reflectivity plot at $\lambda=1.55\ \mu m$. It also shows the transmission through the grating. We can see a similar behavior as with the 2D results from figure 2.12. The first order reflection is maximum at $L_{space} = 275\ nm$, which is slightly larger than $\frac{1}{4} * \lambda/n_{BCB}$, and also the third order reflection is maximum at $L_{space} = 825\ nm$, which is larger than $\frac{3}{4} * \lambda/n_{BCB}$.

The 2D calculations agree quite well with the (more accurate) 3D calculations. The biggest difference is the position of the reflection peaks, which are shifted a little towards a longer value for L_{space} in the 3D simulations. This is caused by the diffraction in the vertical direction that is not taken into account in the 2D simulations. This will be studied in more detail in the next paragraphs.
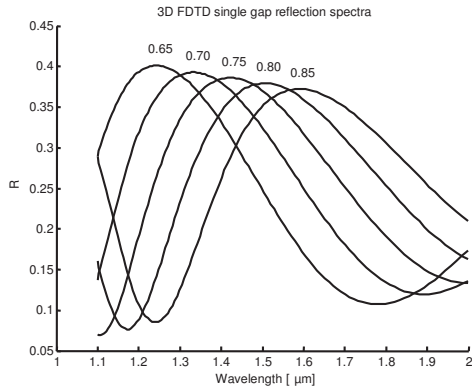
Figure 2.20: 3D FDTD simulation of the reflection spectra of a single period deeply-etched grating. The numbers in the plot refer to the length of the etched gap (L_{space}).

Figure 2.20 shows the reflection spectra for L_{space} between 0.65 μm and 0.85 μm. In this figure we also see that the peak wavelength shifts to the longer wavelengths as the space length increases. In order to obtain a reflection peak at λ=1.55 μm, we need to define the space length between 0.80 and 0.85 μm.

The difference between the optimal simulated space length and the one we expected from the analytic equation (L_{space}= ¾ *λ/n_{BCB}) is attributed to the fact that the field shape in the space-region is not a plane wave, but has a Gaussian shape. This means that the field is actually a superposition of various plane waves with different k-vectors. The average k-vector of the total field therefore has a smaller component in the propagation direction. The effective propagation speed is therefore higher, resulting in a longer optimal gap.
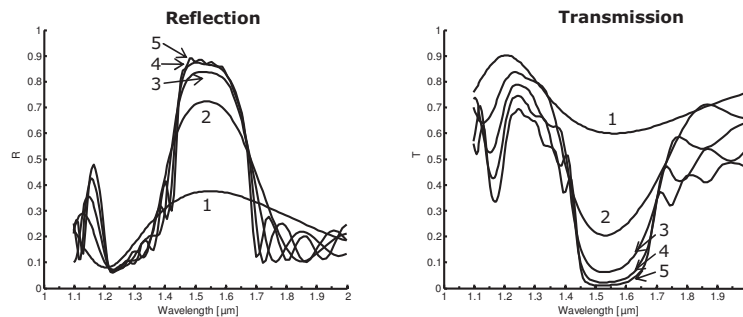
Figure 2.21: Reflection and transmission spectra as a function of number of grating periods for L_{space}=0.825 μm and L_{line}=0.350 μm. The numbers in the graphs indicate the number of periods.

Using the obtained 'new' optimal gap length we calculate the reflection and transmission spectra of the deeply-etched DBR gratings as a function of the number of periods. The results are shown in figure 2.21. In this simulation we used a value of L_{line} = 350 nm, instead of the optimal 360 nm, because this equals an integer number of 25 nm grid units. The oscillation observed in the 5-period reflection spectrum is an artifact caused by the finite simulation time. In this particular case not all the light had left the simulation window yet, but running the simulation for a longer period was not possible due to system resource limitations.

The reflection seems to saturate at approximately 87 % for a 5-period grating at λ=1.55 μm. The bandwidth of the grating is more than 200 nm, allowing for some tolerance in the fabrication process.

2.5 Conclusion

In this chapter we introduced some commonly used theoretical models for studying different types of DBR gratings. It was shown that for gratings with small refractive index differences the coupled mode theory approach is a suitable method to study its reflection and transmission properties. Because this is an analytical method, also wavelength dependencies can be analyzed directly. However, when the refractive index contrast is so large that the field profiles of the propagating modes in the different sections of the grating have significantly different shapes, more complex methods are required.

The Bi-directional Eigenmode Propagator (BEP) is capable of analyzing a broader variety of grating structures. It can even handle structures where some of the grating elements do not support any guided modes (e.g. deeply-etched gratings). However, this method also has its limitations, mainly due to the fact that it works in 2D only. Also, in order to study the wavelength-behavior of the gratings, a lot of simulation time is required.

For the case of deeply-etched DBR gratings, where only a few periods are needed to obtain maximum reflectivity and thus the total structure is small (<10 μm), a 3D FDTD simulation is most feasible. It has the advantage that the entire spectral behavior is obtained from a single simulation run.

It was found that for a deeply etched DBR grating, the angle of the sidewalls needs to be small (<5°). Compared to a 1st order grating, a 3rd order design can still provide a wide enough reflection bandwidth (>200 nm). Although the fabrication tolerances in terms of the length of each section become a bit tighter, the required etch depth is more easy to obtain for a 3rd order grating, as will be shown in Chapter 4 of this thesis. It is also expected that the dimensions of 825 nm for the grating gaps and 360 nm for the grating lines can be realized using modern photo-lithography equipment, making mass production of these 3rd order gratings commercially viable.

Chapter 2

References

1 J. Buus, M.C. Amann and D.J. Blumenthal, "Tunable Laser Diodes and Related Optical Sources", Second Edition, New Jersey, J. Wiley & Sons, 2005

2 M. Yamada and K. Sakuda, "Analysis of almost-periodic distributed feedback slab waveguides via a fundamental matrix approach", Appl. Optics, Vol. 26, No. 16, August 1987

3 Eggleton, B.J.; Krug, P.A.; Poladian, L.; Ouellette, F., "Long periodic superstructure Bragg gratings in optical fibres," *Electronics Letters* , vol.30, no.19, pp.1620-1622, 15 Sep 1994

4 K. O. Hill, "Aperiodic Distributed-Parameter Waveguides for Integrated Optics," Appl. Opt. **13**, 1853-1856 (1974)

5 T. Segawa, S. Matsuo, Y. Ohiso, T. Ishii, Y. Shibata, and H. Suzuki, "Fast Tunable Optical Filter Using Cascaded Mach–Zehnder Interferometers With Apodized Sampled Gratings", *IEEE Photon.Technol. Lett.*, vol. 17, no. 1, Jan. 2005

6 OlympIOs version 5.1.14 by Concept2Volume (C2V) Software, Enschede, The Netherlands

7 A.A.M. Kok, "Pillar photonic crystals in integrated circuits", chapter 2, PhD thesis, TU Eindhoven, The Netherlands, 2008

8 K. Yee, "Numerical solution of initial boundary value problems involving Maxwell's equations in isotropic media," IEEE Transactions on Antennas and Propagation, No. 14, pp. 302–307, 1966

9 A. Taflove, S. C. Hagness, "Computational Electrodynamics: The Finite-Difference Time-Domain Method", 3rd ed., Artech House Publishers, 2005

10 CrystalWave version 4.3 by Photon Design, Oxford, United Kingdom
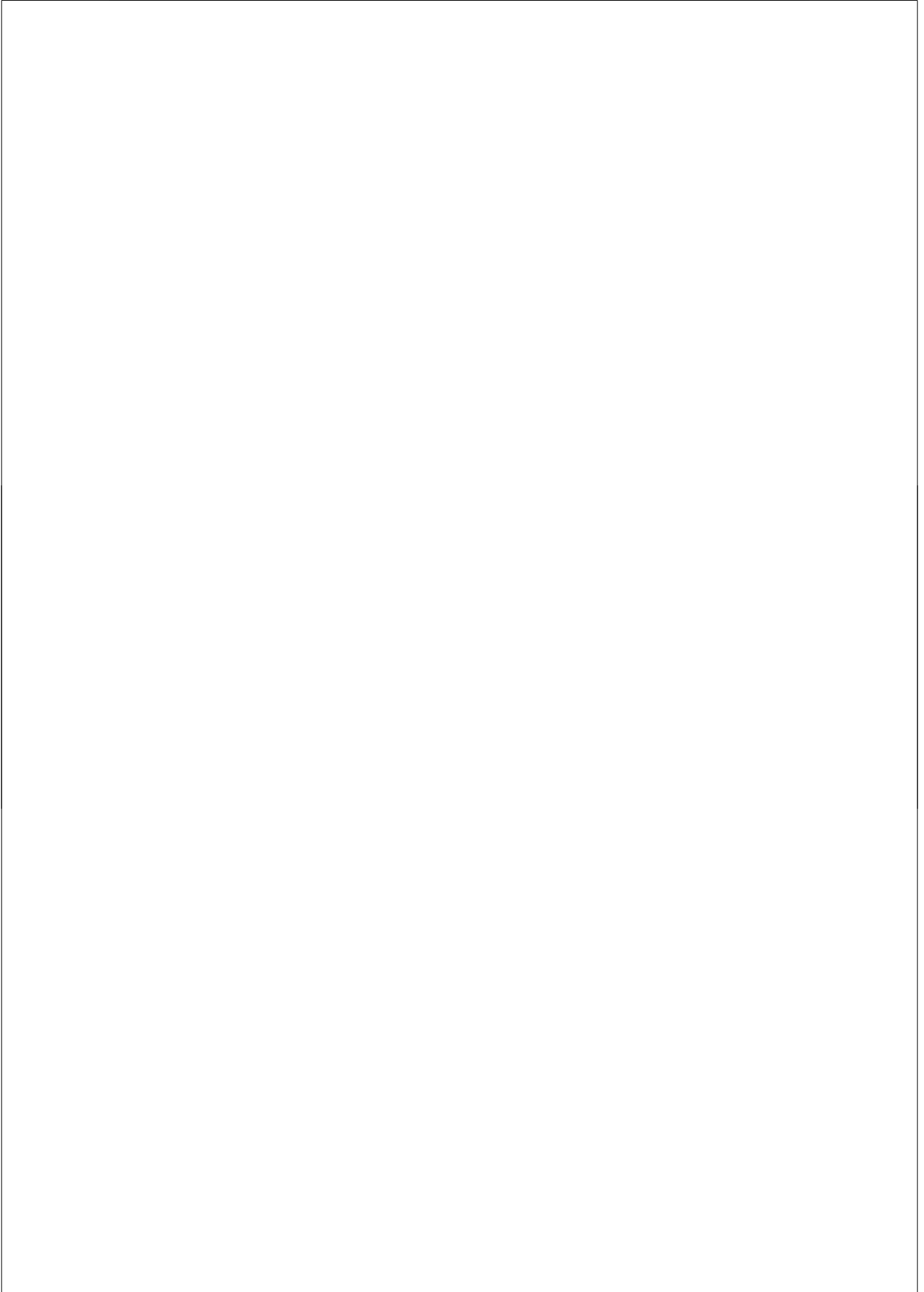
SEM gallery
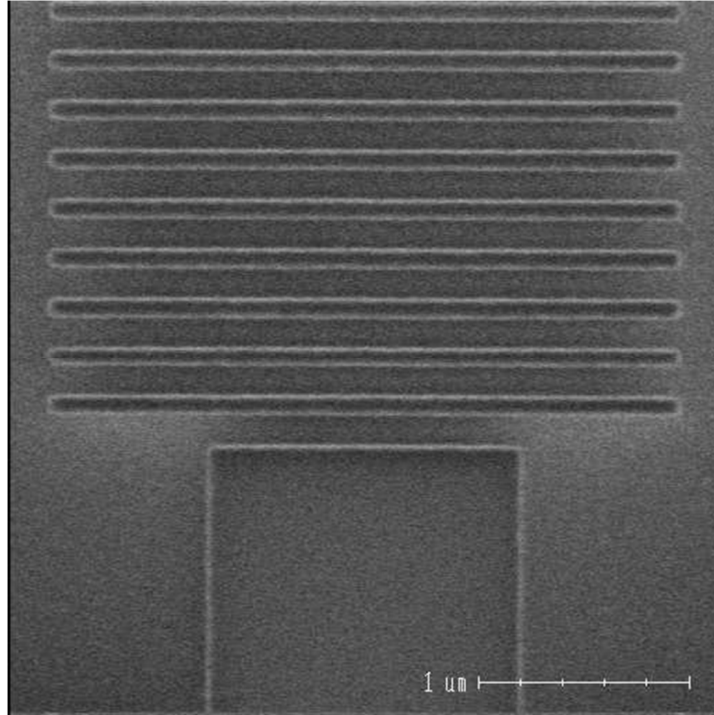
"Japanese precision"

DBR pattern in ZEP e-beam resist written by a
100-kV e-beam writer at NTT Photonics Laboratories

3 Active-passive short cavity DBR laser (NTT)

3.1 Motivation

In this chapter, a short cavity DBR laser is presented that was realized in the fabrication technology developed at NTT Photonics Laboratories[1]. In this technology it is possible to integrate active and passive components, as well as Vertical Groove (VG) gratings on a single chip. This allows us to make VG-grating based DBR lasers that potentially can be integrated with other active and passive components to create more complex integrated circuits.

Various aspects of DBR laser design are described in this chapter. It is shown that the VG-gratings provide high reflectivity with a relatively short grating length. Therefore the total cavity length is quite small. The resulting modespacing is so wide, that the wide reflection bandwidth of the VG gratings is still selective enough to provide single mode operation with a reasonable Side Mode Suppression Ratio (SMSR).

The fabricated devices show that it is possible to achieve laser operation even with very short active regions. However, the loss in the DBR mirrors is still quite high and the device size is limited by the size of the DBR mirrors. It is also found that the VG gratings cannot be made smaller, since the coupling coefficient saturates at some point. These aspects are the basis for the new fabrication technology developed for deeply-etched DBR grating described in Chapter 4.

3.2 Introduction

Compact lasers operating at low powers are important building blocks in digital optical applications. Coupling these lasers makes it possible to realize logical gates and memory cells [1]. In future packet switched networks header processing may be done completely in the optical domain using circuits built from substantial numbers of lasers. Such circuits are already demonstrated using separate components connected by fibers [2]. It is expected that large scale Photonic Integrated Circuits (PICs), containing large numbers of coupled lasers integrated on a single chip could do the job much better, since optical losses and reflections from fiber-chip couplings can be avoided. The polarization control also becomes easier when fiber connections are avoided.

However, integration of large numbers of lasers on a single chip will cause huge thermal dissipation. Therefore there is a demand for small, stable lasers with low power

---

[1] This chapter presents research carried out at NTT Photonics Laboratories, Atsugi, Japan. The results were published in IEEE Photonics Technology Letters, Vol. 19, No. 19, October 1, 2007. The original title is "Short Cavity DBR Laser Using Vertical Groove Gratings for Large-Scale Photonic Integrated Circuits" and is authored by B. Docter, T. T. Segawa Kakitsuka, S. Matsuo, T. Ishii, Y. Y. Kawaguchi Kondo, H. Suzuki, F. Karouta and M.K. Smit. The text in this chapter is based on this letter, but adapted for clarification and to make it fit in the scope of this thesis.

consumption, rather than high output power. Short-cavity DBR lasers provide a good solution, because small drive currents are sufficient to reach high current densities and the wide mode spacing results in stable single mode operation.

Another advantage of devices with a short laser cavity is the broad mode-hop-free tuning range [3]. They also allow high-speed direct modulation [4], and because of their flexible design, the devices allow for easy integration with other active or passive components.

The DBR mirrors consist of VG-gratings, where a corrugation is applied on both sides of the waveguide. This structure enables us to fabricate DBRs with a simple one-step-etching technique. In this structure, the grating depth, which defines the coupling strength and therefore the reflection properties, is controlled by electron beam (EB) lithography [5]. Because of this flexible design strategy, variable types of DBR lasers can be integrated on a single chip. For example, unidirectional light output from DBR lasers, which is desirable in large scale PICs, can be achieved by using an asymmetric-κ DBR structure [6]. In addition, high coupling strengths can be obtained with vertical-groove gratings, making the devices more compact.

3.3 Device design and fabrication

3.3.1 Device layout

A schematic top view and a photograph of the fabricated device are shown in figure 3.1. The device consists of an active region and front/rear gratings, which are connected by tapered waveguides. A deep-ridge waveguide structure was used in the grating and tapered waveguides. This allows a good confinement of the light in the waveguide and a strong interaction of the mode field with the sidewall corrugation.
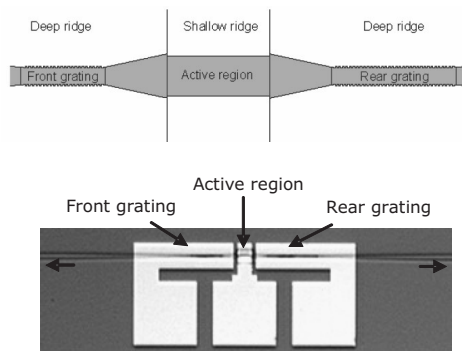
Figure 3.1: Schematic picture (top) and microscope picture (bottom) of short-cavity DBR laser.

For the active region however, using a deep-ridge waveguide would cause unwanted non-radiative recombination of the carriers on the sidewalls due to crystal damage caused by the

etching process. Therefore a shallow-ridge waveguide was used in the active region. The shallow ridge waveguide in the active region is 3 μm wide, whereas a much narrower waveguide was used for the deeply-etched grating regions. To connect the two waveguide types, linearly tapered waveguides were employed to expand the mode profile.

3.3.2 Vertical Groove gratings

The deep-ridge waveguide with vertical-groove gratings enables us to obtain a high reflectivity with a small grating length. The inset in figure 3.2 shows the grating structure, where the grating depth is given by D_g. The plot in figure 3.2 shows the measured coupling coefficients κ (see equation 2.4) of the fabricated deep-ridge waveguides. These measurements were performed on 400 μm long vertical-groove gratings. We estimated κ as a function of the grating depth D_g by measuring the bandwidth of the fabricated gratings. From the measured transmission spectra we took the -10 dB bandwidth and fitted this to calculated transmission spectra using the coupled mode theory[1] as described in section 2.2.

For a given D_g, as the waveguide width becomes narrower, κ increases as shown in figure 3.2. Also, as D_g increases, κ increases linearly up to about 330 cm^{-1} for a waveguide width of 0.55 μm and a grating depth of 125 nm. A further increase in grating depth showed a decrease in κ, which is probably due to mode conversion in the grating. However, a κ of 330 cm^{-1} is adequate to obtain a high reflectivity with short grating length. Therefore these values were used for the fabricated devices. With the length of the front and rear gratings being 50 and 80 μm, respectively, we estimate the peak reflectivity to be 84% for the front grating and 95% for the rear grating.
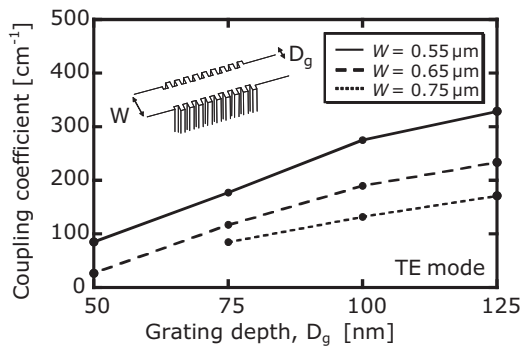
Figure 3.2: Measured coupling coefficient of various vertical groove gratings.

---

[1] The coupled mode theory method might not be 100% accurate for these gratings since the etch depth is quite large compared to the waveguide width and therefore it would be better if the field profile of the guided modes had been taken into account using an Eigenmode Propagation method as described in section 2.3. However, this work was published before the Eigenmode Propagation tools were investigated. It is therefore possible that there is a small error in the values of the coupling coefficients.

3.3.3 Deep-shallow connection

The deeply-etched gratings are connected to the shallow-ridge active waveguide by 23-µm long tapered waveguides. The length of the taper is chosen such that the angle of the taper is the same as for a test structure taper. This test structure taper connected a 6 µm waveguide to a 1 µm waveguide over a length of 40 µm. The loss of this test structure taper was measured to be comparable to the propagation loss of the 1 µm waveguide.

The taper was fabricated in the deep-etched part and it was connected to the shallow active ridge. In the deep-shallow transition there is a 0.4 µm width difference to provide optimal mode coupling. With these tapered waveguides, the total device length of the smallest device becomes 200 µm.

3.3.4 Active-passive integration

The active region consists of a multiple quantum well (MQW) active layer containing 10 QWs on an n-InP substrate. A schematic picture of the shallow ridge containing the quantum wells is shown in figure 3.3. The exact composition of the MQW layer stack is confidential, but the relevant parameters for designing the laser are given in the table next to the figure.
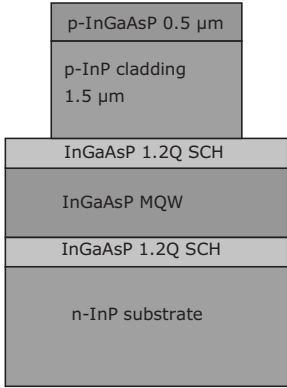
MQW parameters:	
# of wells	10
Total thickness	170 nm
Equivalent refractive index	3.2174 @ 1.55 µm
SCH layer thickness	70 nm

Figure 3.3: Schematic cross-section of the active waveguide and MQW parameters.

For this laser device an active-passive integration process based on metal organic chemical vapor deposition (MOCVD) was used. The process consists of 3 growth steps: first the MQW layer stack is grown, ending with a non-doped InP layer of 130 nm. Then the active areas are covered by a SiO_2 layer which is patterned by a photo-lithography process. The MQW layer is removed from the passive areas by selective wet etching with diluted sulfuric acid. In the second growth step a passive InGaAsP layer (λ_{PL} = 1.4 µm) is re-grown in the areas not covered by SiO_2. After removing the SiO_2 layer the p-doped InP cladding and InGaAsP contact layers are grown in the third and final growth step. The final layer structure is shown in figure 3.4.
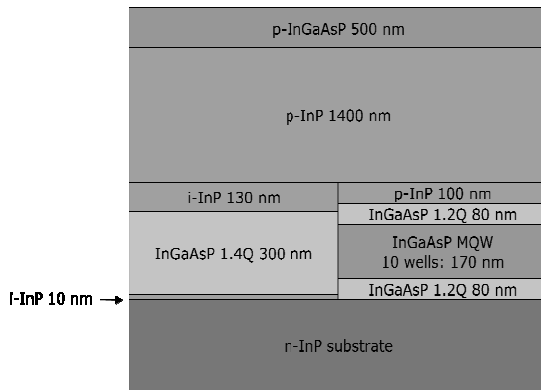
Figure 3.4: Passive and active layer structures.

3.3.5 Fabrication process

The deep ridge, containing the vertical-groove grating structures, was formed by chlorine-based inductively coupled plasma reactive ion etching (ICP-RIE). The waveguide pattern was defined by 100-kV EB lithography, and then transferred into a pre-deposited SiN layer (600 nm) by RIE. This SiN layer served as a mask for the ICP-RIE process. This process provides a deep etch (4 µm) with steep and smooth sidewalls. SEM images of the fabricated deep-ridge containing a vertical groove grating connected to a tapered waveguide are shown in figure 3.5.
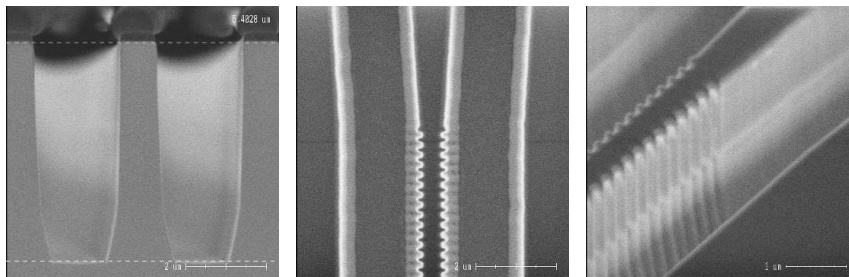
Figure 3.5: Left: Cross-section of dummy sample after 30 min. of ICP etching. Middle: Top view of 0.55 µm wide waveguide with 125 nm deep grating and a taper towards the active-passive Butt-Joint. Right: Same structure from a different angle.

After fabricating the deep-ridge structure, the shallow-ridge was formed by selective wet etching with diluted HCl, which stops at the top of the active layer. The shallow-ridge waveguide is 3 µm wide to provide enough gain for the short cavity. The structure was coated with a Benzocyclobutene (BCB) and etched back for planarization. Then, Ni/Zn/Au electrodes were deposited on the contact layer by a lift-off process. After the metallization, the sample was polished down to 120 µm thick and Au/Ge/Ni n-contacts were deposited on

the back-side. Finally the sample was cleaved and both facets were coated with anti-reflection films.

3.3.6 Round trip loss calculation

Figure 3.6 shows the calculated round trip loss as a function of the wavelength deviation from the Bragg wavelength of the gratings. For the propagation loss in the passive parts a value of 10/cm was used. The grating reflectivity was calculated using a coupled mode theory method as described in section 2.2. The dots represent the cavity mode spacing, resulting from the effective length of the gratings as defined in section 2.2.

In the calculations we assumed that one of the cavity modes coincides exactly with the Bragg wavelength of the gratings. Although the reflection bandwidth of the gratings is quite wide, the short cavity increases the mode spacing. The increased mode spacing gives enough difference in round trip loss between the main laser mode and the neighboring side-modes to result in a sufficiently high SMSR.
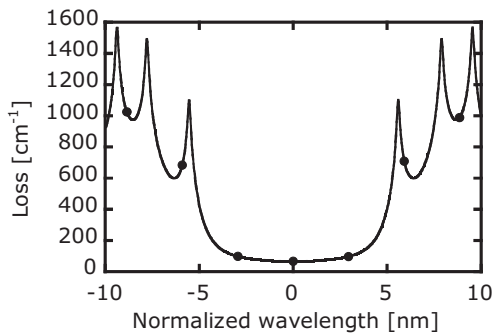
Figure 3.6: Total round trip losses for a device with an active area length of 25 μm, around the Bragg wavelength of the gratings. The dots indicate the cavity modes.

3.4 Device characterization

3.4.1 L-I characteristics

The L-I curves for 3 devices with different active region lengths were recorded at room temperature as shown in figure 3.7. The devices show threshold currents of 14, 13 and 10 mA for 25, 35 and 50 μm long active regions respectively. The power consumption was in the order of 30 mW per device. A thermal roll-off effect is clearly visible for the shorter devices.

This is probably also the reason for the higher threshold current of the shorter devices: although the reduced cavity length results in a higher current density (threshold current density is 18.7, 13.3 and 9.3 kA/cm^2 for the 25, 35 and 50 μm active region devices respectively), the gain per unit length increases only marginally (due to the higher

temperature). At the same time the gain per round trip is lower, due to the shorter active area, while the mirror losses stay the same. Therefore even higher current densities are required to reach the lasing threshold.
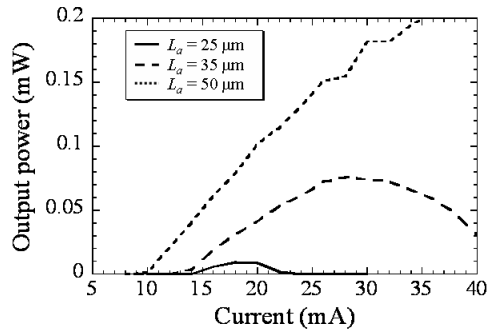
Figure 3.7: L-I curves for 3 short-cavity DBR lasers with active area lengths of 25, 35 and 50 μm.

3.4.2 Spectral properties

The lasing spectra of the different devices are shown in figure 3.8. The shortest device shows a mode spacing of 2.95 nm and a side mode suppression ratio of 35 dB when operated at 18 mA. The longer devices have a smaller mode spacing and according to the graph in figure 3.2, one would expect a worse SMSR. However, both the 35 μm and the 50 μm active area devices have an SMSR of 41 dB. The most probable explanation is that the dominant laser mode of the 25 μm device is not aligned with the peak DBR reflectivity. Therefore the main laser mode has a smaller round trip gain advantage compared with the longer devices, where the dominant mode is aligned better to the mirror reflectivity spectrum. This hypothesis is supported by the fact that in the 35 μm and the 50 μm devices both side modes have comparable output power and therefore the main laser peak is aligned with the peak reflectivity, whilst in the 25 μm device there is only one side mode visible.

25 um active area
I = 18 mA, FSR = 2.95 nm, SMSR = 35 dB

35 um active area
I = 26 mA, FSR = 2.65 nm, SMSR = 41 dB

50 um active area
I = 40 mA, FSR = 2.35 nm, SMSR = 41 dB
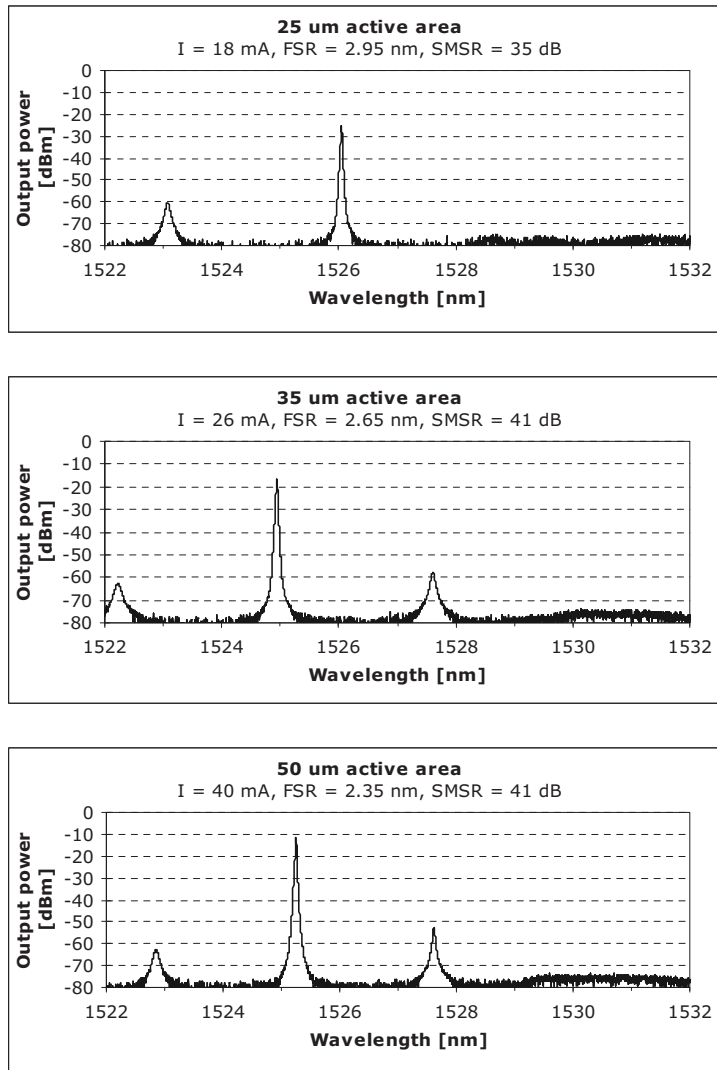
Figure 3.8: Lasing spectra of 25, 35 and 50 µm active area short-cavity DBR lasers. Drive currents, Free Spectral Range (FSR) and Side-Mode Suppression Ratio (SMSR) values are given in graph titles.

3.5 Discussion and conclusion

For future photonic integrated circuits, heat generation in active components is going to be a major issue, since most devices need very stable temperature conditions. For logical circuitry, stable single mode operation with low power consumption is more important than high output power, since the communication distances are not very long. The short-cavity DBR lasers presented in this chapter show a power consumption in the order of 30 mW per device, which means that several hundreds of devices could easily be integrated on the same chip, without getting into serious problems disposing the generated heat.

However, the current device is not the limit in terms of power consumption. These devices operate at current densities of 10 kA/cm^2 and above, due to the high losses in the DBR sections. At these high current densities the gain medium is not very efficient anymore, so a reduction in the mirror loss could improve the device performance substantially.

The loss in the DBR mirrors is mainly caused by the narrow waveguide width, necessary to obtain a high coupling strength and thus a small device footprint. However, with the current fabrication process it is not possible to obtain a larger grating depth. Therefore in the next chapter a new fabrication process is described in which it is possible to create DBR mirrors that are etched all the way through the waveguide. With these gratings it is possible to obtain over 90% reflectivity within only a few µm, even in 1.5 µm wide waveguides.

Using gratings with higher coupling strengths could reduce the drive current, but a higher coupling strength would increase the reflection bandwidth of the gratings as well. This means that the different modes experience almost the same DBR reflectivity and therefore the SMSR of the laser will be reduced. However, if the laser can be made so small that the mode selectivity will be dominated by the gain spectrum, rather than the DBR reflection spectrum, single mode operation would still be feasible.

There are also other ways to influence the mode competition inside the laser cavity. A very effective example is given in chapter 6 where we demonstrate the use of filtered feedback to obtain single mode operation in a long Fabry-Perot laser with broadband DBR mirrors.

Chapter 3

References

1 M. T. Hill, H. J. Dorren, T. de Vries, X. J.M. Leijtens, J. H. den Besten, B. Smalbrugge, Y.-S. Oei, H. Binsma, G.-D. Khoe, and M. K. Smit, "A fast low-power optical memory based on coupled micro-ring lasers," Nature, vol. 432, pp. 206-209, Nov. 2004

2 H. J. S. Dorren, M. T. Hill, Y. Lui, N. Calabretta, A. Srivatsa, F. M. Huijskens, H. de Waardt, and G. D. Khoe, "Optical packet switching and buffering by using all-optical signal processing methods," J. Lightwave Technol., Vol. 21, No. 1, Jan. 2003

3 N. Fujiwara, T. Kakitsuka, M. Ishikawa, F. Kano, H. Okamoto, Y. Y. Kawaguchi Y. Kondo Yoshikuni, Y. Tohmori, "Inherently mode-hop-free distributed Bragg reflector (DBR) laser array," IEEE J. Sel. Top. Quantum Electr., Vol. 9, No. 5, pp. 1132- 1137, Sept-Oct. 2003

4 K. Shinoda, T. Kitatani, M. Aoki, M. Mukaikubo, K. Uchida, K. Uomi, "1.3-μm InGaAlAs short-cavity DBR lasers for uncooled 10-Gb/s operation with low drive current," IEEE Phot. Techn. Lett., Vol. 18, No. 22, Nov. 2006

5 T. Segawa, S. Matsuo, Y. Ohiso, T. Ishii, Y. Shibata, H. Suzuki, "Fast tunable optical filter using cascaded Mach-Zehnder Interferometers with apodized sampled gratings," IEEE Phot. Techn. Lett., Vol. 17, No. 1, pp. 139-141, Jan. 2005

6 K. Takahata, K. Kasaya, H. Yasaka, Y. Kondo, M. Ikeda, "A unidirectional output optical frequency conversion device with anasymmetric-κ DBR structure", IEEE J. Quantum Electr., Vol. 30 No. 5, pp. 1219-1226, May 1994

42
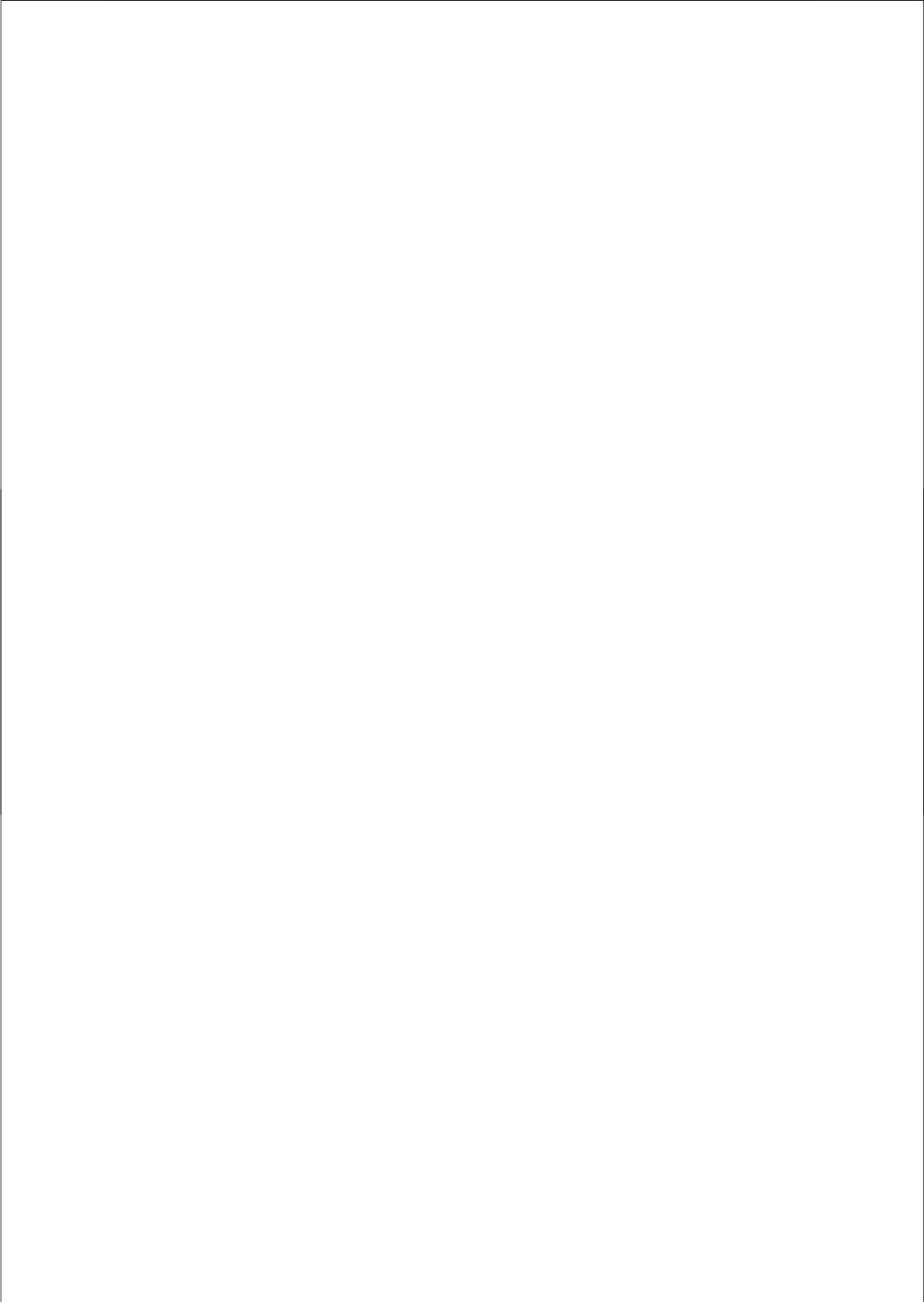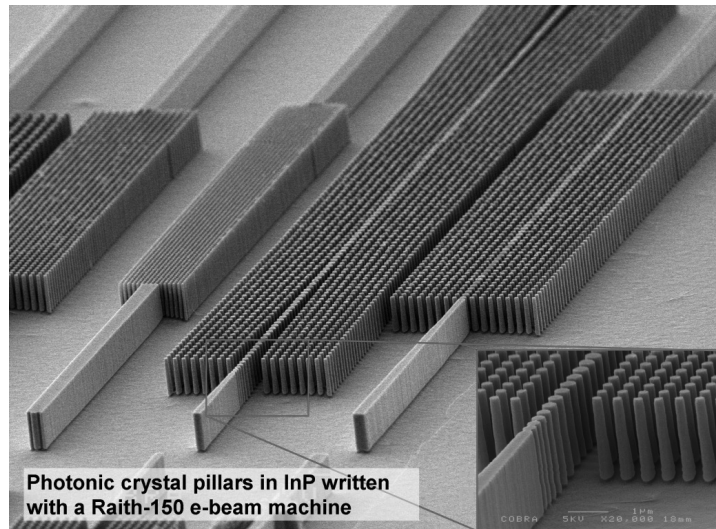
"Bed of nails"

Photonic crystal pillars realized in the etching process described in section 4.3.4.
Winner of the 2007 Raith micrograph award 1st prize.

4 Fabrication technology

4.1 Introduction

This chapter describes the fabrication technology that was developed for the realization of deeply-etched DBR gratings in InP-based Photonic Integrated Circuits. In order to add these gratings as a new building block for PICs, the standard fabrication process as described for example in [1] has to be adapted. There are two main issues that need to be addressed:

• DBR pattern definition

• Straight & smooth deep etching of DBR structures and waveguides

The working principle of the DBR grating relies on the fact that the positions of the interfaces between waveguide and low-refractive index material (either air or some polymer) are accurately defined. This requires the use of e-beam lithography (EBL) as a replacement or an addition to conventional optical lithography. Additionally, as was shown in Chapter 2, the reflections inside the DBRs are only efficiently coupled back into the waveguide if the interface is as straight as possible (preferably <3° angle) and well through the waveguide layer (>1.5 µm). This requires the development of a new etching process to realize deeply etched structures.

Microchip fabrication processes often require carefully balanced process parameter settings. These processes are easily disturbed by small changes in material composition, machinery condition, and the status of the sample. It is therefore not surprising that changing the lithography step and one of the etching steps has its consequences for the rest of the device process flow. The masking process, for example, is crucial in order to transfer a well-defined lithography pattern into a high quality waveguide structure. Also the new deep etching process requires a new way of planarizing the chip before adding metal contacts.

This chapter describes the main advances in the fabrication technology, starting with the e-beam lithography process in section 4.2. Then the new ICP etching process will be described in section 4.3. Since the choice of etching process puts extra requirements on the masking materials, the most suitable masking layers are described in section 4.4. These new masking layers also enable the combination of EBL and optical lithography. The BCB-based planarization is described in section 4.5 and finally in section 4.6 the total process flow for fabricating an active-passive integrated circuit with deeply etched DBR mirrors will be described briefly. More extensive processing details can be found in Appendix A.

4.2 E-beam lithography (EBL)

4.2.1 Introduction

As shown in chapter 2, a DBR mirror needs to be defined with sub-micrometer resolution. Although with modern deep-UV lithography systems it is possible to achieve these dimensions, a mask set for such a system is very expensive and therefore only cost effective when used in very high volume production. Electron-Beam Lithography (EBL) provides a good alternative, especially for prototyping and for low volume production.

However, the DBR mirrors only form a very small part of the whole Photonic Integrated Circuit (PIC) and writing the whole circuit with an e-beam machine would be very time-consuming. Therefore a process is developed in which only the DBR mirrors are written by EBL, while the rest of the circuit is patterned with optical lithography. This is further described in sub-section 4.4.3. In this section we will focus on the initial EBL process for getting an accurate DBR definition.

4.2.2 Electron-beam system

In this work we used a Raith 150 e-beam system. The basis of the system is a LEO Scanning Electron-beam Microscope (SEM) that is connected to a computer controlled pattern generator. The maximum acceleration voltage that the machine can operate at is 30 kV. The electron beam of the SEM can be used to write a pattern, but the write-field is generally limited to a maximum size of 200x200 μm^2. Of course the system can be used to write larger patterns, but this requires the movement of the sample stage, resulting in stitching errors between different write-fields. These stitching errors can range from 30 to 200 nm, depending on the use of local alignment markers.

4.2.3 E-beam resist

The e-beam resist used for the DBR patterns is ZEP520 [2], which is a positive resist (exposed areas are removed in the development process). ZEP520 is known for its good resistance against dry etching processes. It can easily be removed by oxygen plasmas or in a n,n-dimethylacethamide solution. Using a moderate spinning speed of 5000 rpm, a 320 nm thick layer of ZEP can be obtained. DBR patterns can be created by defining the spaces between the DBR sections as shown in figure 4.1.
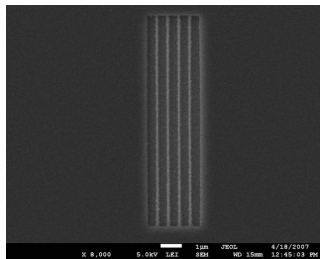
Figure 4.1: DBR pattern in ZEP.

4.2.4 Proximity effect

The exposure in an electron-beam system is influenced by a so-called proximity effect. This proximity effect is caused by electrons that scatter from the substrate (see figure 4.2) and expose the e-beam resist over a wide area. The exposure dose of the back-scattered beam is very low compared to the dose produced by the forward-scattered electrons. But because the range over which it affects the surrounding pattern is usually quite large (several μm's), the combined influence on a single point in the pattern can be significant. When the acceleration voltage is moderate (<50 kV) this proximity effect can cause a serious change in the exposed pattern, and some form of correction is usually necessary.
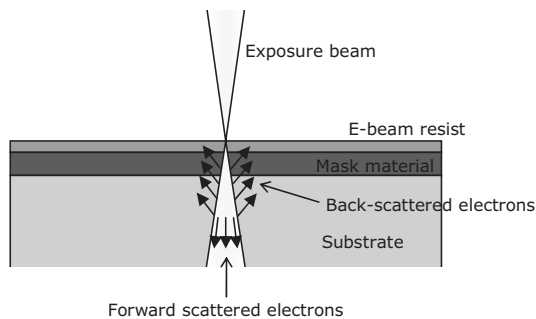
Figure 4.2: Proximity effect due to back-scattered electrons in e-beam lithography.

A common way to describe the influence of the forward-scattered beam and the backward-scattered beam is given by the following double-Gaussian equation [3]:

$$f(r) = \frac{1}{\pi(1+\eta)}\left[\frac{1}{\alpha^2}e^{-\left(\frac{r}{\alpha}\right)^2} + \frac{\eta}{\beta^2}e^{-\left(\frac{r}{\beta}\right)^2}\right]$$

(4.1)

This equation gives the exposure f at a distance r from the initial beam. α and β give the range of the forward- and backward- scattered electrons respectively and η determines the ratio between back- and forward-scattered exposure.

The parameters α, β and η depend on the masking materials and the substrate material and can be determined by conducting a doughnut-test [4,5]. This test consists of writing a series of ring-shaped structures while varying the dose and the size of the rings. The value for α, β and η that were found in this way are given in table 4.1. These values are valid for the masking materials described in section 4.4.

α	19 nm
β	2335 nm
η	0.34

Table 4.1: Proximity effect parameters for 320 nm ZEP / 50 nm Cr / 430 nm SiO$_x$ on an InP substrate

With these parameters it is possible to calculate the exposure dose of any particular pattern. Reciprocally, it is also possible to compensate the exposure dose of a pattern so that the final pattern is written with effectively a constant dose. To achieve this, the software of the e-beam writer fractures the pattern in small rectangular shapes and calculates the influence of each element on all other elements surrounding it. An example of the final dose-pattern achieved this way is shown in figure 4.3.

It is clearly visible that the center of the pattern is assigned a lower dose than the outer edges and corners of the pattern, to compensate for the back-scattered electrons from the surrounding pattern.

Fracturing the design like this has a few drawbacks. First of all, calculating the proximity effect correction takes quite some computer power. Second, the resulting structure contains much more elements, and therefore the total design file size is much larger. Third, when the pattern contains many small elements, the writing time in the Raith150 system is mainly determined by the movement and stabilization waiting times between each structure, and therefore the writing time can increase several orders of magnitude after a proximity effect correction. And finally, fracturing the structure can result in an increased roughness of the final structure. The latter can happen when the size of the fractured pattern is not an integer times the e-beam step size. This will result in an interference effect, where some parts of the pattern get a higher dose simply because more e-beam steps fit into that particular shape. An example of this effect is shown in figure 4.4.
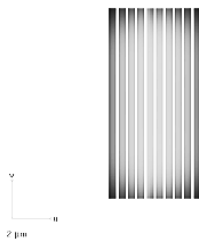
Figure 4.3: Proximity effect compensated DBR pattern. The dark areas on the corners indicate a higher dose than the light shades in the center of the pattern.
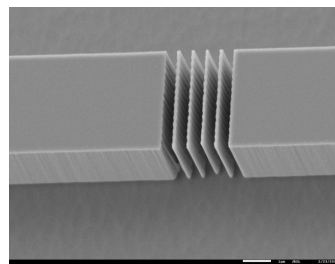
Figure 4.4: Proximity effect compensated DBR pattern etched into InP waveguide. The roughness on the DBR mirror is caused by the fractured proximity effect corrected pattern.

4.2.5 Determination of dose factors for deeply-etched DBR gratings without proximity effect correction

In the previous sub-section a proximity effect compensation method as included in the software of the Raith 150 machine was described. It was shown that there are several complications with this method. However, in the case of our deeply etched DBR mirrors, the biggest compensation is required on the corners of the pattern (see figure 4.3), while these corners fall outside the waveguide pattern. This is shown in section 4.4.3 where the combination of optical- and e-beam lithography is described. This suggests that it is sufficient to find an exposure dose so that the center of the exposed pattern is as designed, only taking into account the number of DBR periods.

The SEM images in figure 4.5 show DBR patterns written without proximity effect correction, but with two different dose factors. This dose factor gives the fraction used of the nominal dose, which is usually set at 100 $\mu C/cm^2$. At the center of the patterns, the variation in line width between the inner line and the two lines on the outside is smaller than the accuracy of the measurement method. But when the total exposure dose is increased, the width of the lines is also increased. This means that the right dimensions can be obtained simply by choosing the right dose factor for the whole structure, depending on the number of DBR periods.
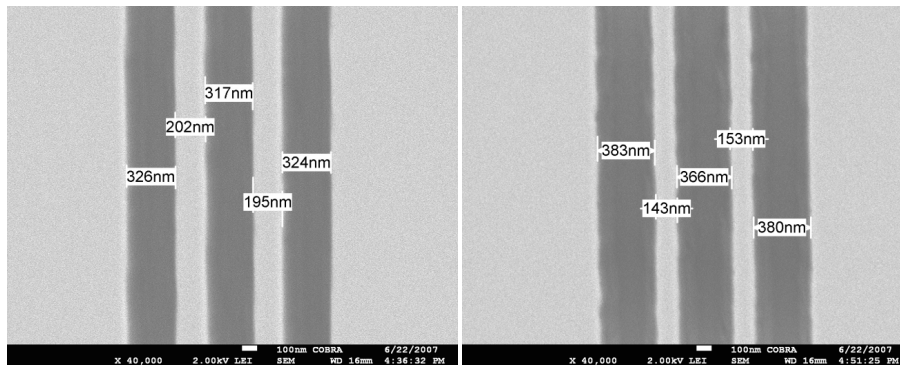
Figure 4.5: DBR patterns written without proximity effect compensation with dose factor 0.53 (left) and 0.61 (right).

Two experiments were conducted to find the correct exposure dose. In each experiment a matrix of grating patterns were written. In one direction the number of periods was varied, in the other direction the dose factor. In the first experiment, lines with a designed width of 387.5 nm were written. This corresponds to a 1st order grating when the spaces are filled with air. In the second experiment, 750 nm wide lines were written, corresponding to a 3rd order grating for spaces filled with BCB. After processing the patterns were measured and the results are plotted in figure 4.6 and figure 4.7.

1st order DBRs in air
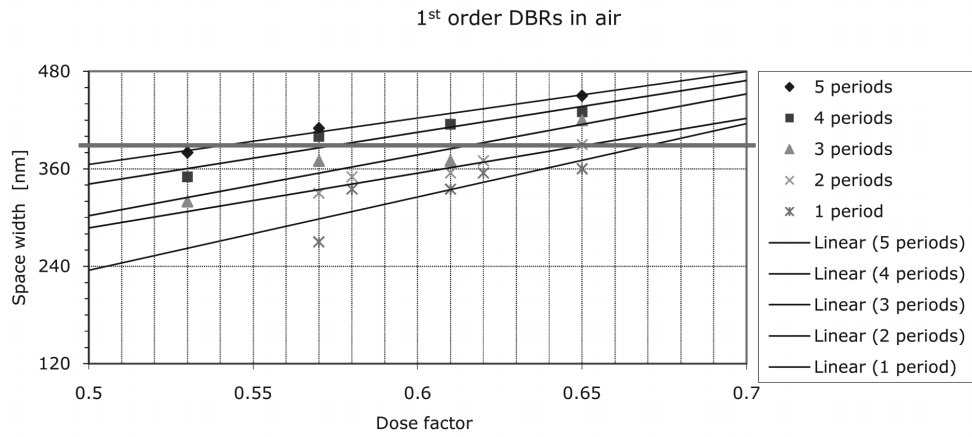
Figure 4.6: Measured average line widths of 1st order DBR gratings filled with air. Linear function fits are also plotted. The lowest diagonal line corresponds to 1 period, the highest diagonal line to 5 periods. The horizontal solid line shows the targeted size (387.5 nm).

3rd order DBRs in BCB
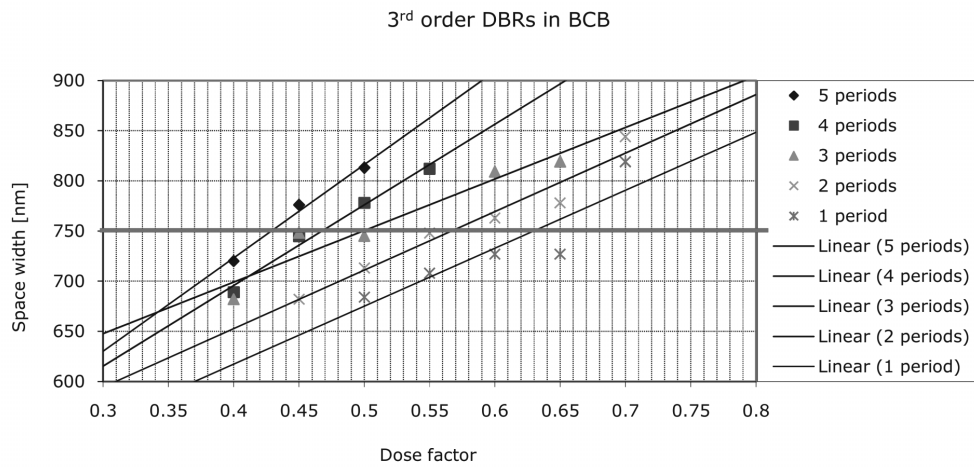
Figure 4.7: Measured average line widths of 3rd order DBR gratings filled with BCB. Linear function fits are also plotted. The lowest diagonal line corresponds to 1 period, the highest diagonal line to 5 periods. The horizontal solid line shows the targeted size (750 nm).

The measured data points were fitted with a linear function and from the crossing with the appropriate line width (showed with horizontal solid line in graphs), the correct dose was determined. The final dose is shown in figure 4.8.
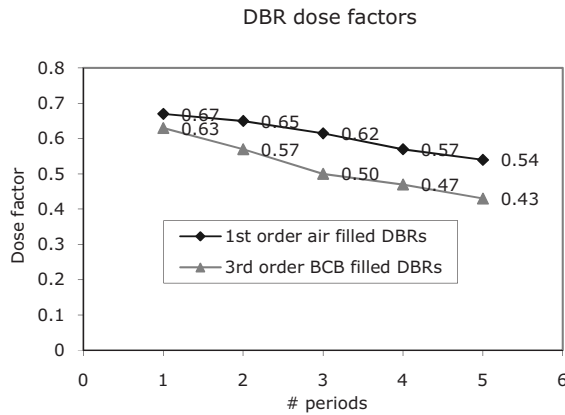
Figure 4.8: Dose factors to obtain correct line widths for 1st order DBRs in air and 3rd order DBRs in BCB.

4.2.6 Conclusion

In this section a method was described that can be used to write simple DBR patterns for DBR mirrors that cross the full width of the waveguides. It was shown that the proximity effect plays an important role, but full compensation of this effect by fracturing the design in small shapes is not necessary. Instead, a simple compensation of the exposure dose as a function of the number of DBR periods is sufficient. This technique was tested for DBR mirrors with 5 or less periods.

4.3 ICP etching

4.3.1 Introduction

To be able to realize deeply-etched DBR gratings in complex PICs we changed from a $CH_4:H_2$-based Reactive Ion Etching (RIE) process to a Cl_2-based Inductively Coupled Plasma (ICP) process. This process allows us to realize high aspect ratio structures with smooth and straight sidewalls. In a Photonic IC fabrication process, however, the etching of the optical waveguides is probably the most critical step. A slight change in process conditions will immediately influence both optical and electrical performance of the device. Changing the etching process is therefore a very risky affair, and should be done carefully.

4.3.2 ICP etching system

The new etching process was developed using an Oxford Plasmalab 100 system with an ICP plasma source. The main difference between an ICP system and a normal RIE system is that the plasma is created with an induction coil, which allows the user to control the ion density in the plasma (ICP power) separately from the ion energy (RF power). This makes it possible to go to high plasma densities without increasing the physical energy of the etching species and therefore reducing surface damage. The high ionization rate allows a reduction

of the total process pressure, resulting in fewer collisions in the plasma sheath and therefore less under-etching.

4.3.3 Etching processes

The quality of the etched structures depends strongly on the chemistry of the etching process. A common chemistry used for etching InP is $CH_4:H_2$ [6]. The CH_4 in this chemistry is responsible for the formation of a polymer layer during the etching process. This polymer protects the sidewalls of the etched structures from further (chemical) etching. However, it also builds up on the bottom of an etched surface. Therefore the $CH_4:H_2$ etch step is usually alternated with a O_2 descum cycle. This results in a etch process with a very well controlled etch rate and smooth sidewalls. A disadvantage is that the etch cycle and descum cycle need to be balanced very carefully. This can be difficult when the size of the etched features is very different, for example in the case of a waveguide with a deeply-etched DBR grating.

In this work we will investigate several chlorine based processes. We will discuss a pure Cl_2 process, a $Cl_2:CH_4:H_2$ process and a $Cl_2:Ar:H_2$ process. Although there are more chlorine based gasses (BCl_3 is often used [7], so is $SiCl_4$ [8]) only Cl_2 gas was available.

In all three processes, the Cl_2 ions react with the In, P, Ga and As atoms creating mostly tri-chloride compounds (e.g. $InCl_3$, PCl_3, etc.). Most of these tri-chlorides have low boiling temperatures (75 – 200 °C) at atmospheric pressure, making them very volatile at low processing pressure. $InCl_3$, however, has a standard boiling point of 800 °C, which reduces to about 150 °C at the typical processing pressure of 4 mTorr. If the process temperature is lower than 150 ºC, the $InCl_3$ tends to induce micro-masking that results in rough etched surfaces [9]. This effect is shown in figure 4.9. Several samples were etched with different electrode temperatures. The samples were glued to a 4" silicon carrier wafer with a thermal conductive paste, so the actual sample temperature will not be much higher than the electrode temperature. However, if we omit the heat sink paste (see figure 4.10), and the sample temperature can increase during the etching process, all the etched samples show a smooth etched surface. The fact that without thermal paste the etch depth is comparable for each temperature setting indicates that the temperature quickly rises to more than 150 °C in the initial stage of the etching process. This experiment shows that it is possible to obtain smooth structures even at low temperature settings and we do not need to use a thermal paste. This is advantageous because the paste is difficult to remove afterwards and can contaminate other equipment during further processing.

60 °C   **100 °C**   **150 °C**   **200 °C**
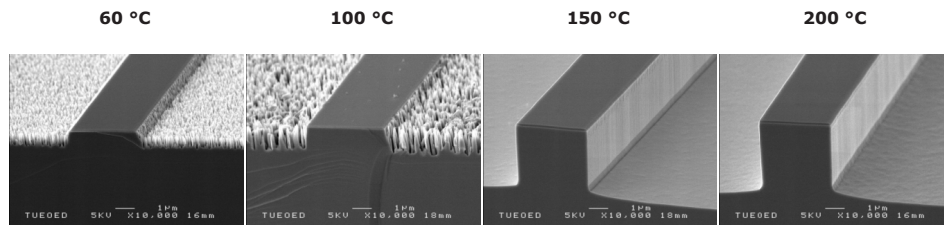
Figure 4.9: ICP etched waveguides with different electrode temperature settings using heat sink paste. Other process conditions: Cl$_2$:Ar:H$_2$ 7:4:12 sccm, 2 min., ICP 1000 W, RF 120 W, 400 nm SiN$_x$/InP.

60 °C   **100 °C**   **150 °C**   **200 °C**
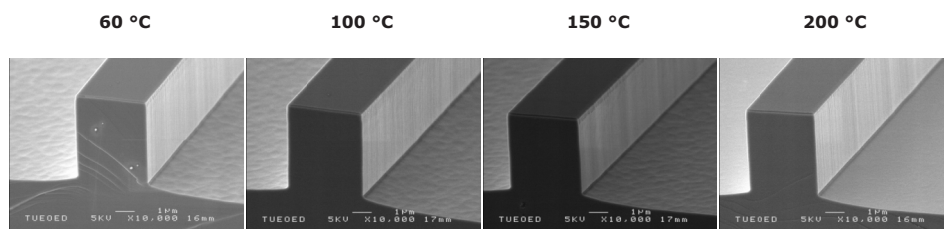
Figure 4.10: ICP etched waveguides with different electrode temperature settings without heat sink paste. Other process conditions: Cl$_2$:Ar:H$_2$ 7:4:12 sccm, 2 min., ICP 1000 W, RF 120 W, 400 nm SiN$_x$/InP.

The simplest process to etch InP/InGaAsP is to use a pure chlorine plasma. This chemistry results in very smooth surfaces and the selectivity of the InP with respect to the etching mask (SiO$_2$ or SiN$_x$ are suitable materials) is usually more than 20:1. However, etch rates are generally low (< 1 µm/min) and the shape of the etched waveguide structures tends to be wider at the bottom (see figure 4.11). This shape can be improved slightly by adjusting the process pressure and the gas flow, but it can never be completely straight. Although this is a problem for high aspect ratio structures with very narrow openings (e.g. DBR gratings), for deep etched waveguides a wider waveguide foot is not a big problem, because the waveguide film is usually less than 2 µm below the top of the waveguide.

Cl$_2$ Cl$_2$:Ar:H$_2$ Cl$_2$:CH$_4$:H$_2$
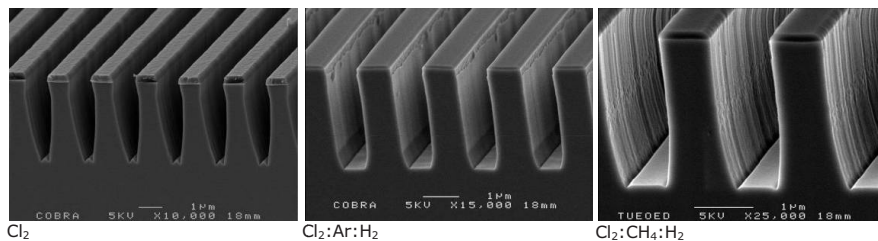
Figure 4.11: Different etching chemistries resulting in different etch profiles. Note that the pictures are taken with different magnification.

To increase the etch rate and improve the directionality of the etching process, some argon can be added to the process chamber. The argon ion bombardment adds energy to the

etching process. This increases the etch rate and improves the etched profile. However, the argon also causes more mask degradation. Some faceting on the corners of the mask is observed and if the etch time is too long, this faceting will cause extra roughness on the etched sidewalls.

Adding hydrogen to the chemistry results in some passivation of the etched surface. By balancing the H_2 content, under etching can be prevented without decreasing the etch rate much. The best results were obtained using a Cl_2:Ar:H_2 ratio of 7:4:12 sccm and a pressure of 4 mTorr.

Another way to passivate the sidewalls of the waveguides, and thus to decrease the roughness, is to add some methane to the process. The CH_4 creates a polymer coating that protects the sidewall to further etching by the Cl_2 species. The optimal gas flow was found to be Cl_2:CH_4:H_2 7:8:5.5 sccm and 4 mTorr process pressure. The CH_4 process results in smooth sidewalls and therefore low waveguide losses [10]. However, the etch rate is lower compared to the Cl_2:Ar:H_2 process, while mask erosion is similar. This limits the maximum etch depth. Also the etching profile tends to widen as the etch depth increases, which is problematic for the small openings required for the DBR gratings.

After this preliminary investigation of the different chemistries, the Cl_2:Ar:H_2 process was chosen as the most promising for realizing deeply-etched DBR gratings. The next sub-section describes the process in more detail.

4.3.4 Cl_2:Ar:H_2 etching for DBR gratings

Taking the Cl_2:Ar:H_2 process with a gas ratio of 7:4:12 sccm as a basis, some experiments were done to investigate the influence of process pressure and ICP- and RF power settings on the etch rate, mask selectivity and lag effect. The mask selectivity is defined as the difference in etch rate between the InP and the masking material. The lag effect is the reduction in etch rate in small spaces (e.g. inside the DBR gratings) compared to the etch rate in large open areas. This is indicated in figure 4.12. It is caused by the fact that it is more difficult for the etching products to be removed from the bottom of the etched feature. The lag effect should not be confused with the 'loading effect', which describes a reduction in etch rate when the mask only covers a small part of the total chip surface and large areas are exposed to the plasma, reducing the concentration of reactive species. The loading effect can cause small isolated features to etch faster than large open areas, but in the case of the Chlorine based plasmas described in this chapter the lag effect is more dominant.

In figure 4.12 also the effect of mask faceting is shown. In dry etching processes it is common that the mask erodes faster at the corners. This results in an approximate 45° angle at the mask edges. Especially for the small DBR features, this can cause a much faster degradation of the mask pattern than what would be expected from the material selectivity alone.
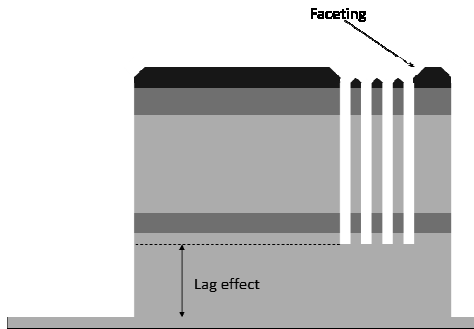
Figure 4.12: Schematic presentation of the lag effect and the mask faceting effect.

The graphs in figure 4.13 show the etch rate and the selectivity between InP and SiO_x masking material as a function of RF power (left figure) and process pressure (right figure), for various ICP power settings. As expected, the etch rate increases as the ICP and RF powers increase. The trend in selectivity is not so clear, due to lower measurement accuracy when measuring the low etch rate in the SiO_x mask layer. However, almost all process settings show a value higher than 20:1. This is high enough to obtain a sufficiently deep etch with when using the standard 430 nm thick SiO_x masking layers.

Changing the process pressure increases both the etch rate and the selectivity. Higher (> 4 mTorr) processing pressures can deteriorate the etched profile due to under-etching and was therefore not investigated.
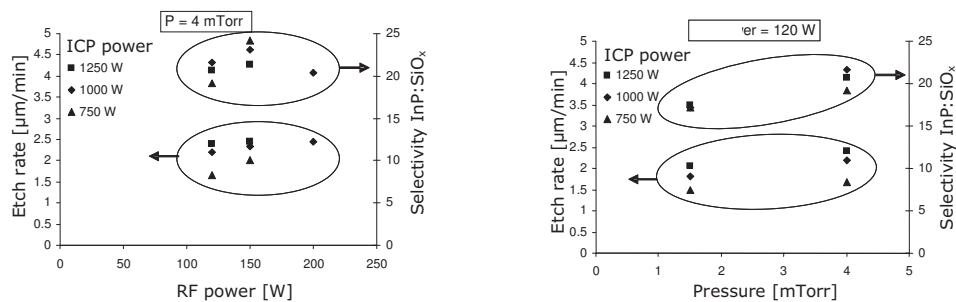
Figure 4.13: Etch rate and selectivity as a function of RF power (left) and process pressure (right) for various settings of ICP power.

The graphs in figure 4.14 show the lag effect as a function of RF power (left figure) and process pressure (right figure) for different ICP power settings. From these figures it is clear that an ICP power of 750 W is beneficial in order to limit the lag effect and to obtain a sufficiently deep etch in between the DBR mirrors.

However, for 1st order BCB-filled gratings, where the gap in the DBRs is just 250 nm, the lag effect is still around 50%. This means that to obtain an etch depth of 3.5 µm inside the

grating, the surrounding area must be etched to a depth of 7 µm. With a process selectivity of about 20:1, this means that the mask will be etched by about 350 nm. Due to the faceting effect, the standard mask thickness of 430 nm will not be sufficient. It is therefore decided to move to 3rd order DBR gratings filled with BCB. These gratings have a gap of 750 nm and suffer much less of the lag effect. An example of an etched DBR grating that is designed as a 3rd order BCB filled grating is shown in figure 4.15. The lag effect in this case (ICP power: 750 W, RF power: 150W, pressure: 4 mTorr) was only 18%.
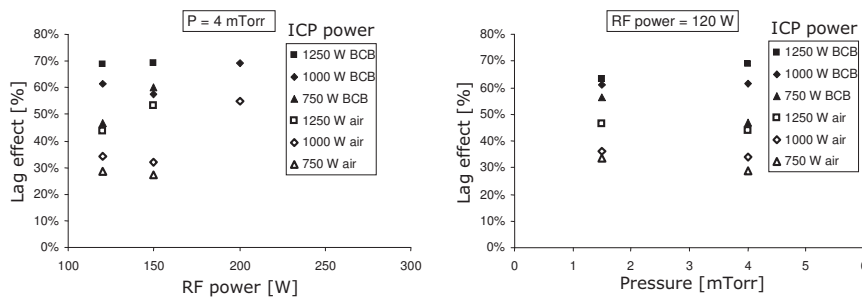
Figure 4.14: Lag effect in 1st order BCB filled gratings (solid points, gap=250 nm) and 1st order air filled gratings (open points, gap=388 nm) as a function of RF power (left) and process pressure (right) for various settings of ICP power.
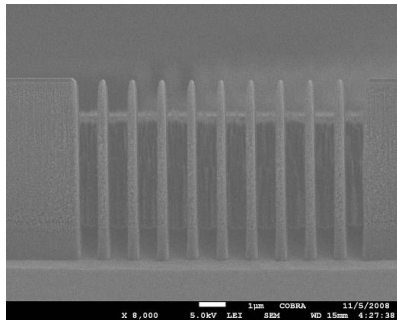
Figure 4.15: SEM image of a deeply-etched DBR grating designed as a 3rd order grating filled with BCB. Line/space ratio is 360/750 nm. In the background the shallow-etched chip surface is visible. The lag effect between the DBR lines is measured to be approximately 18%.

4.3.5 Chemical passivation mechanism

The profile of an etched structure depends on the process settings. The process pressure and the RF power are known to have a large influence on sidewall roughness and under-etching. However, in many processes also chemical passivation of the sidewalls is used. In CH_4-based processes, for example, the formation of polymers during the etching process prevents the sidewalls from being etched. In the Cl_2-based etching processes a SiO_x-based passivation mechanism was found [11]. There it is shown that when an InP sample is placed on a silicon carrier wafer, a very thin (3-20 nm thick) SiO_x film is deposited on the sidewalls

of the etched structures. The source of the silicon is probably the silicon carrier wafer, while the oxygen is thought to come from the quartz carrier wafer holder.
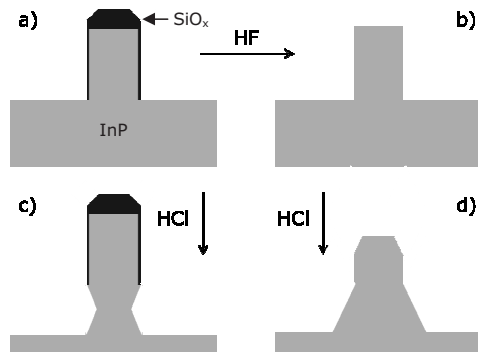
Figure 4.16: During the Cl2:Ar:H2 etching process a SiOx passivation layer is formed on the sidewalls of the structure (a). Part of the sample is put in a HF solution to strip the SiOx (b). Both samples are then put in a HCl solution that etches the InP. In the sample where the SiOx is still present, the etching only occurs below the passivation layer (c). In the other case the InP is attacked everywhere (d).

The SiO_x passivation layer is so thin that it can't be made visible with the SEM. However, an experiment with a wet etching solution shows that in the Cl_2:Ar:H_2 etching process a similar passivation mechanism occurs. The experiment is shown schematically in figure 4.16. It shows a sample that is etched in a Cl_2:Ar:H_2 process. Then one part is put in 10% HF to strip the SiO_x mask and the SiO_x passivation layer. Then both samples are put in a HCl solution that etches the InP. The results of this experiment are shown in figure 4.17. It is clear that the structures on the sample that was not put in HF are only attacked below the initial ICP etch. This indicates that there is a passivation layer that can be removed by HF, which confirms that it is silicon-based. It is important to know that this passivation layer is present on the etched samples, since the sidewall surface now has a different composition. If not removed, the passivation layer can have a large impact on future process steps.
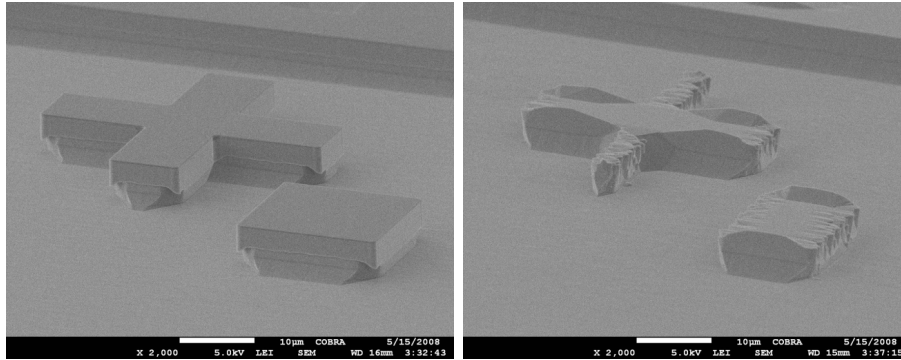
Figure 4.17: SEM images of samples treated with HCl InP wet-etch after the Cl$_2$:Ar:H$_2$ ICP etch. The image on the left shows that the InP is only attacked below the SiO$_x$ passivation layer. The sample in the right image was put in 10% HF solution after the ICP etch, to strip the SiO$_x$ mask and passivation layer. The HCl therefore also attacked the rest of the structure.

4.3.6 Conclusion

In this section a new ICP etching process based on a Cl$_2$:Ar:H$_2$ chemistry was described. With the new etching process it is possible to obtain deeply-etched structures with straight and smooth sidewalls. The low lag effect makes it suitable for the fabrication of 1st order DBR gratings filled with air (gaps of 388 nm) or 3rd order DBR gratings filled with BCB (gaps of 750 nm). It was found that a silicon-based passivation layer is formed on the sidewalls of the etched structures.

4.4 Etching masks

4.4.1 Introduction

In order to obtain waveguides and gratings with smooth and straight walls, a high quality etch mask is required, because any irregularities in the etch mask will be transferred to the final structure. Similarly, if the etch mask has angled sidewalls, these will be transferred to the etched waveguide as well, although the angle will be reduced by the mask selectivity.

The mask needs to be defined by optical- and/or e-beam-lithography. Usually standard photo- and e-beam resists have a limited resistance to dry etching processes. Therefore the resist layer has to be very thick, which generally decreases the pattern resolution.

It is possible to apply some intermediate materials into which the resist pattern is first transferred. These materials can then serve as etch masks later on. This section describes these multi-step masking techniques for application in high power ICP etching processes.

4.4.2 SiO$_x$ and SiN$_x$ dry etching masks

Common masking materials used for Cl$_2$-based ICP processes are SiO$_2$ and Si$_3$N$_4$. These so-called 'hard mask' materials show high selectivity with respect to InP and InGaAsP in

common dry etching processes. They can be etched by Fluorine-based plasmas and removed by (buffered-) hydrofluoric ((B)HF) acid. The films are deposited in a Plasma Enhanced Chemical Vapor Deposition (PECVD) system. Because the films deposited in this process are not 100% stoichiometric, we usually describe SiO_2 as SiO_x and Si_3N_4 as SiN_x.

In order to transfer a pattern into the hard mask we have two RIE processes available: one process is based on a $CHF_3:O_2$ chemistry and one uses purely CHF_3 gas. Although the former process has a higher etch rate, the latter usually gives smoother results and is therefore preferred. The etch rates of SiN_x and SiO_x for the pure CHF_3 process are shown in Table 4.2.

This table also shows the etch rates of various materials that can be used as a mask for the etching of SiN_x and SiO_x. Photo resist (HPR504) and e-beam resist (ZEP) have a higher etch rate compared to commonly used metals such as Ti, Al, and Cr.

CHF_3 process			
	etch rate [nm/min]	selectivity to	
		SiO_x	SiN_x
SiN_x	20		
SiO_x	17		
HPR504	4.4*	3.9	4.6
ZEP	11*	1.6	1.8
Ti	5	3.4	4.0
Al	1.3	13	15
Cr	<1**	>17	>20

Table 4.2: Etch rates and selectivity to SiO_x and SiN_x of various materials in the CHF_3-pure process. Process settings: CHF_3 flow: 60 sccm, Pressure: 15 mTorr, RIE power: 50 W, Room temperature. *: these etch rates were measured while etching SiN_x **: etch rate too low to measure accurately

Although the etch rate of SiN_x is slightly higher than the etch rate of SiO_x, the selectivity of SiO_x towards InP in the ICP etching process is slightly higher and therefore SiO_x is preferred. The etch rates of HPR504 and ZEP shown in Table 4.2 were measured during etching of SiN_x. However, when SiO_x is etched, extra oxygen atoms will be added to the process gas due to the etching products. The oxygen can increase the etch rate, especially of the polymer based resists. Therefore the selectivity of HPR504 and ZEP towards SiO_x reported in Table 4.2 is probably slightly overestimated.

The standard thickness of the SiO_x layer when used as a dry etching mask in the ICP is 430 nm. The standard thickness of the HPR504 optical resist after waveguide lithography is approximately 750 nm. Even with a moderate selectivity of about 1:3, this thickness is still sufficient to get a high quality transfer of the waveguide pattern from the photoresist to the hard mask. In the case of e-beam defined patterns, however, the 320 nm thick ZEP layer

combined with a selectivity of 1:1.6 is not enough, since a little over-etching to make sure all the small features are open is usually necessary. Increasing the ZEP layer thickness is not beneficial for the e-beam resolution. Therefore an extra chromium layer is introduced in the process as an extra intermediate layer for the pattern transfer. This is described in the next subsection.

4.4.3 SiO$_x$ / Cr masking for optical & e-beam lithography

In Table 4.2 it is shown that various metal layers can be used as etch masks for etching SiO$_x$ layers. Chromium shows the highest selectivity of the metals tested and can therefore be used with minimal thickness. This thickness is important because it determines the accuracy by which the lithographically defined pattern can be transferred to the metal.

The Cr intermediate layer allows the combination of e-beam and optical lithography. The process is as follows: We first deposit a 50 nm Cr layer by e-beam evaporation. Then we define the DBR pattern by e-beam lithography (see figure 4.18a). The DBR pattern consists of the gaps that will be etched away later on. Some alignment markers are also defined so that the waveguide pattern can be aligned to the DBR pattern. The grating lines are 10 μm long, much more than the waveguide width, which is typically 1.5-3.0 μm wide. This makes the alignment more tolerant and avoids the proximity effects that distort the corners of the pattern.

The pattern is etched into the chromium layer by a Cl$_2$:O$_2$ ICP process. The process is based on [12], which describes the etching of Cr and CrO$_x$ layers for anti-reflective EUV optical lithography masks. The gas flow settings are: Cl$_2$:O$_2$ 15:15 sccm, ICP power: 500 W, RF power: first 50 W for 5 seconds to ignite the plasma, then reduced to 5 W, pressure: 10 mTorr, electrode temperature: 60 °C. No heat sink paste was used, but the process powers are relatively low, so a major increase in temperature is not expected. The etch rate of the process is little more than 50 nm/min for Cr and between 100 and 150 nm/min for ZEP and HPR resists. The low selectivity that these numbers imply can be increased with lower RF power, but then there is a higher risk that the plasma will become unstable. Because the chromium layer is only 50 nm thick, the low selectivity is acceptable.

The thin chromium layer allows us to do a high quality optical waveguide lithography step. The waveguide pattern is defined in HPR photoresist and etched into the Cr layer (see figure 4.18b) by the same ICP process as described above. The final Cr pattern that serves as an etch mask for the SiO$_x$ layer is shown in figure 4.18c.
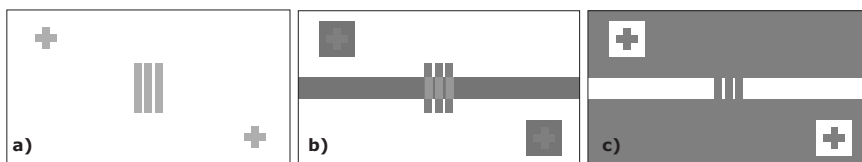
Figure 4.18: Two step lithography process. First the e-beam pattern is defined in ZEP (a). Then the pattern is etched into the chromium layer and the waveguide pattern is defined in HPR504 (b). Finally the waveguide pattern is also etched into the chromium layer and the total pattern is ready to be transferred into the SiO$_x$ layer (c).

A common way of removing e-beam- and photo-resists is by using an O$_2$ plasma in a barrel etcher. However, due to the relatively high pressure in such a system (1000 mTorr or higher) a chromium layer that is exposed to the oxygen plasma will oxidize forming a thermally unstable CrO$_3$ oxide rather than a thermally stable Cr$_2$O$_3$ oxide[13]. Therefore another way of removing the ZEP and the HPR photoresist has to be found.

ZEP can quite easily be removed by n,n-dimethylacetamide, although this solvent is quite aggressive towards many polymer-based materials (e.g. cleanroom gloves) and care has to be taken while using it. A ZEP layer that was used in a 1 minute Cr-etch process can be removed by 30 seconds in n,n-dimethylacetamide without damaging the Cr layer.

HPR is more difficult to remove. During the Cr-etch process the outer layer of the resist profile becomes very hard. When trying to remove the resist in acetone, this outer crust stays on the sample, either on the waveguide or just beside it. The crust can be removed using a short O$_2$ plasma process in an RIE system (1 minute 60 sccm O$_2$ plasma at 50 W and 15 mTorr pressure). The pressure is low enough to prevent the formation of unstable Cr-oxides. However, using this process to completely remove the photoresist can result in removal of the Cr layer as well. This is attributed to the presence of Cl ions in the photoresist layer. These ions are implanted during the Cr-etch process. When the Cl ions are released in the O$_2$ plasma they can attack the Cr layer. The O$_2$ plasma process should therefore only be used to remove the top of the resist layer, after which the rest of the resist can be removed in acetone.

4.4.4 Shallow-deep masking for ICP processes

Most complex photonic integrated circuits consist of two types of waveguides: Shallow-etched waveguides for low loss connections and amplifiers, and deeply-etched waveguides for tight bends and DBR mirrors. To avoid current leakage due to surface recombination, shallow waveguides are etched 100 nm into the waveguide film, while the deeply-etched waveguides are etched all the way through the waveguide layer.

In the past there was one etching process that was used for both waveguide types. This standard shallow-deep process is schematically shown in figure 4.19. When the waveguide mask is defined, the shallow part is covered by photoresist and the difference between the

deep- and the shallow etch depth is applied. Next the photoresist is removed and the whole structure is etched to the required shallow-etched depth.
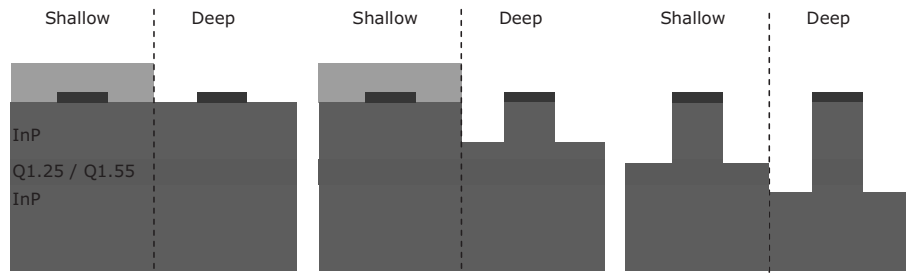
Figure 4.19: Standard shallow-deep processing. The left picture shows a cross-section of a shallow and a deep waveguide with the SiO_x/SiN_x waveguide definition. The shallow part is covered by photoresist. In the middle picture the difference between shallow and deep is etched. In the picture on the right the whole structure is etched to the final depth.

For the DBR mirrors a new Cl_2:Ar:H_2 etching process was developed (see section 4.3.4) that is not very suitable for shallow etched waveguides because the etch rate is very high and it is therefore difficult to stop the process at 100 nm into the waveguide film. Moreover, the bottom of the etched structures is usually not completely flat, causing problems further away from the waveguide. Therefore the etching of shallow waveguides is done using a CH_4:H_2 process [6] that has a more controlled etch rate.

In the new process, the deep-shallow definition is made in a layer of photo-definable polyimide. We use polyimide instead of photoresist because polyimide can be baked at 325 °C, which makes it resistant to the high-power Cl_2:Ar:H_2 process. When normal photoresist is baked at this temperature, it loses its shape and is very difficult to remove after the etching process.

There are two options to perform the 2-step etching starting with a mask pattern as shown in figure 4.18c. We can either first do the shallow etch, followed by the deep-shallow polyimide lithography and finish with the deep etch (S-D process). But we can also start with the deep-shallow lithography, followed by the deep etch and then do the shallow etch (D-S process). Both options are illustrated in figure 4.20.

| Shallow | Deep | Shallow | Deep | Shallow | Deep |

InP
Q1.25 / Q1.55
InP

| Shallow | Deep | Shallow | Deep | Shallow | Deep |

Q1.25 / Q1.55
InP
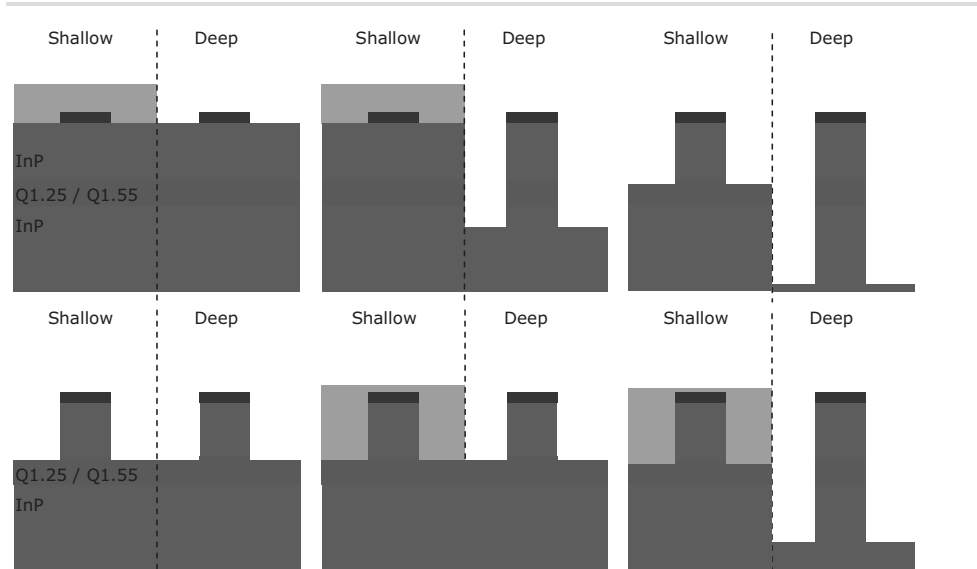
Figure 4.20: New shallow-deep processing. The top row shows the first-deep-then-shallow (D-S) process. The bottom row shows the first-shallow-then-deep (S-D) process. In both cases the shallow-deep definition is made by polyimide.

Both processes were tested and the results are shown in figure 4.21. The D-S process has some advantages over the S-D process. First, the shallow etch does not have to have perfectly straight sidewalls in the D-S case. A slight angle in the shallow etch will result in a small broadening at the bottom of the deep etch, which is not a problem. The roughness that is visible at the top of the deeply-etched waveguide in the S-D process is caused by non-straight shallow etch.

Second, the D-S process is less affected by roughness. At the transition between the shallow and deep etch, some roughness can occur due to the fact that the first seconds of a plasma process are usually not completely stable. The transition between shallow and deep etch is visible on the deep-waveguide sidewalls in figure 4.21. When the shallow etch is performed first, this roughness coincides exactly with the waveguide film, where most of the light is concentrated. This can therefore cause high losses. The disadvantage of doing the deep etch first is that the etching products of the shallow etch can re-deposit on the deep-etched sidewalls. However, this can easily be removed by standard H_3PO_4 and HF cleaning.

63
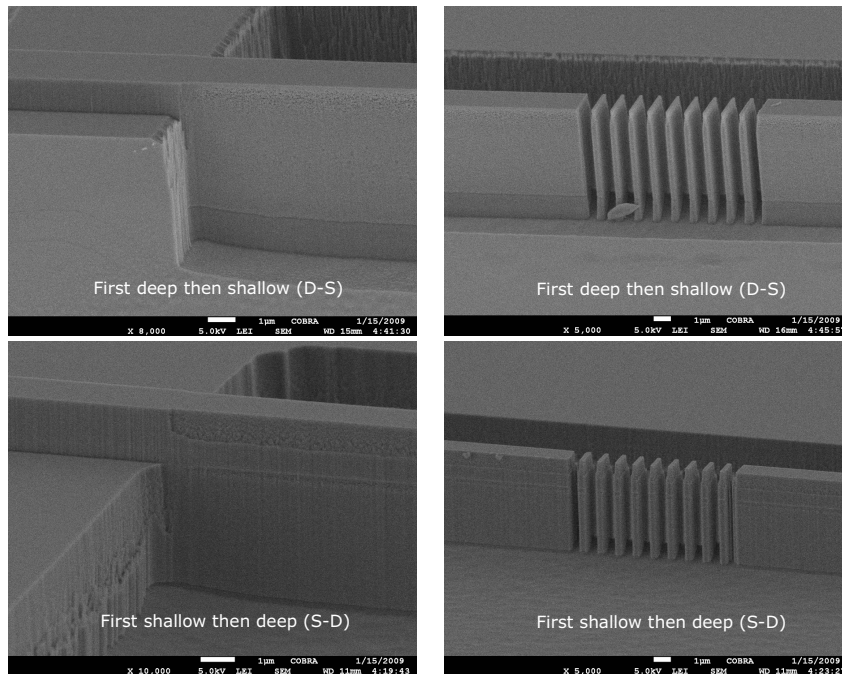
Figure 4.21: SEM images of the new shallow-deep processing. Left images show the interface between a shallow and a deeply-etched waveguide. The right images show a deep waveguide with a DBR grating. The top two images show the first-deep-then-shallow (D-S) process. The bottom row shows the first-shallow-then-deep (S-D) process.

4.4.5 Conclusion

In this section several masking techniques that are used in the fabrication process were described. It was shown how a complex mask pattern consisting of two lithography steps can be transferred into a SiO_x layer using a thin Cr inter-layer. It was also shown that photosensitive polyimide can be used as a mask for deep-shallow processing in a high power ICP process.

4.5 Planarization

4.5.1 Introduction

After the fabrication of the waveguides, electrical contacts have to be added to the circuit. The electrical contacts allow current injection for optical amplifiers and electrical field induced refractive index changes for optical phase modulators. Since the waveguides are only a few microns wide, they are too narrow to make a direct electrical contact on them. Additionally, the metal should have minimal overlap with the optical field in the waveguide, to avoid extra propagation losses. In order to overcome these issues, the waveguides are usually covered (planarized) by some polymers so that only the top of the waveguides are open. Subsequently a metal contact can then be defined by a lift-off lithography process

that does not require a very accurate alignment. In this section suitable materials and methods for planarization of deeply etched waveguides are discussed.

4.5.2 Polymers for planarization

The two most common polymer materials used for planarization purposes are polyimide and bisbenzocyclobutene (BCB). Polyimide has very good mechanical-, thermal-, and chemical properties and is used in many electronics applications for electrical passivation purposes. When planarizing a waveguide circuit with polyimide, first a layer is spun on the chip and then baked in an oven to cure the layer. Then another layer is spun and baked and this process is repeated until the height difference is in the order of 100 nm. See figure 4.22. Next, the polymer is etched back until the waveguides are exposed and the electrical contacts can be made.
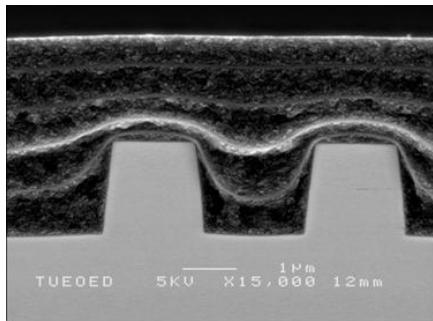
Figure 4.22: 2 μm wide waveguides planarized with 5 layers of polyimide. A thin SiO_x film was deposited between the different polyimide layers to make them visible in the SEM image.
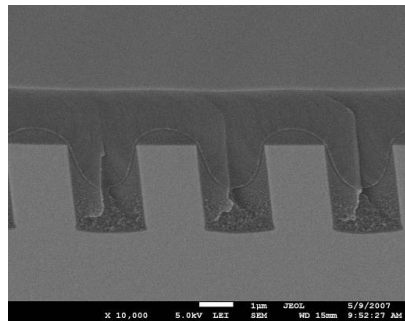
Figure 4.23: 2 μm wide waveguides planarized with 1 layer of polyimide and 1 layer of BCB. The sample is tilted 25° to the front side, so the surface is also visible.

Since the deep-etch that was developed for the DBR gratings is much deeper than the deep-etch used in the past, it would require many layers of polyimide to obtain a sufficiently planar surface. This is a very time-consuming process, since the baking process takes about 6 hours for each layer.

BCB generally has better planarization properties compared to polyimide. This is illustrated in figure 4.23, where a first layer of polyimide covers the waveguide and then a second layer of BCB planarizes the structure nicely. This is not a very practical case however. In order to contact the waveguide the combined polyimide/BCB layers need to be etched back, which is not possible since there is no etching process available that etches both materials at the same etch rate. Therefore a planarization process using only BCB was developed, which is described in the next sub-section.

4.5.3 BCB planarization of deeply-etched structures

In order to make good contacts it in not necessary to have a perfectly planarized surface. As long as the sidewalls of the waveguides are completely covered and the angle of the polymer surface next to the waveguide is not too large, a good contact can be made. It is therefore possible to achieve a good enough planarization with only 1 layer of polymer.

In figure 4.24 two SEM images are shown of a deeply-etched waveguide (including the SiO_x etching mask) planarized with a single layer of either polyimide or BCB. Both layers were spun and baked with a process that, on a flat sample, would result in a layer about half the thickness of the waveguide etch-depth. We can see that the BCB layer has a much more planar surface. Also, the BCB layer hardly covers the top of the waveguide, whereas the polyimide layer still requires etching back to open the top of the waveguides. The amount of polyimide on top of the waveguide increases with the waveguide width. In contrast, even 4 μm wide waveguides planarized with BCB are not visibly covered with BCB.

A disadvantage of BCB compared to polyimide is the limited adhesion of BCB to InP. This can be solved by first depositing a thin (~100 nm) layer of SiO_x on the structure.
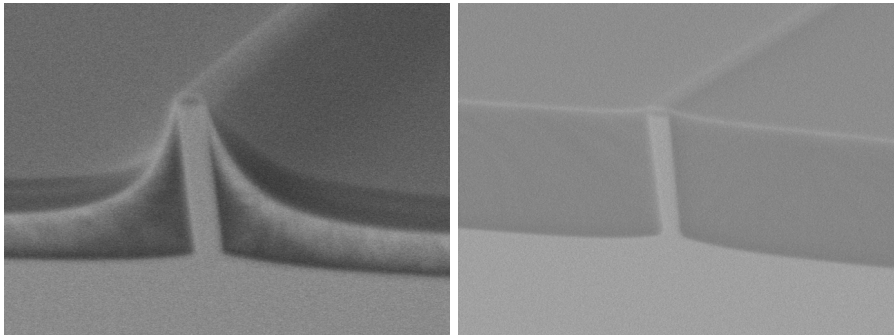
Figure 4.24: 1 μm wide waveguides planarized with a single layer of polyimide (left) and BCB (right). Note that the SiO_x etching mask is still present on top of the waveguides

4.5.4 Conlcusion

In this sub-section a new planarization process using BCB was described. It is shown that it is possible to planarize deeply-etched structures with a single layer of BCB. This can save a lot of processing time compared to the many layers of polyimide that would be required.

4.6 Process flow

This section describes the process flow for realizing a DBR laser on an active-passive wafer as shown in figure 4.25. In the figure the layer thicknesses are shown as well. The fabrication of such an active-passive wafer is described in [14]. This section only describes the main process blocks. For full details please refer to appendix A.
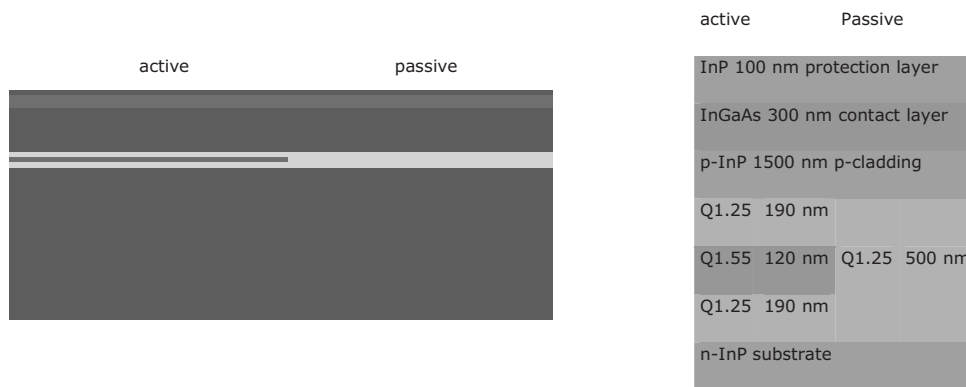
Figure 4.25: Active-passive wafer structure. The left part shows the active layer stack, the right part the passive regrown layer stack. The table shows the layer composition and thicknesses.

Cleaning

First the active-passive wafer is cleaned in an O_2 plasma to remove any organic contamination, followed by a diluted phosphoric acid ($H_2O:H_3PO_4$) solution to remove inorganic particles. Then the 100 nm thick InP protection layer is removed by $HCl:H_3PO_4$.

EBL alignment markers

Next an optical lithography step is performed using AZ4533 positive photo-resist to define alignment markers. The markers are etched about 1 μm into the substrate using a $CH_4:H_2$ RIE process, so that they are visible in the EBL. This allows the alignment of the E-beam pattern to the active-passive pattern.

Mask layer deposition

Then the different masking layers are deposited. First a 430 nm thick SiO_x layer is deposited by PECVD, followed by a 50 nm thick chromium layer, which is deposited by e-beam evaporation.

E-beam DBR lithography

The e-beam lithography step consists of spinning the ZEP resist layer, baking, e-beam exposure with the DBR pattern, development and etching the DBR pattern into the Cr layer with the ICP Cr-etch process. The ZEP resist is stripped with an n,n-dimethylacethamide solution.

Optical waveguide lithography

The optical waveguide pattern is defined in 750 nm thick HPR504 photoresist. This pattern is then transferred into the Cr layer by the same ICP process as was used to transfer the DBR pattern. The HPR photoresist is removed using a short O_2 RIE step to break the top of the resist layer followed by acetone spraying to remove the rest.
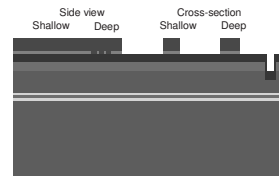
Mask etching

After the DBR and waveguide lithography the pattern is etched into the SiO_x mask. We use a pure CHF_3 process with some over-etching. The Cr layer is then removed in an O_2 plasma stripper and some phosphoric acid cleaning is done to clean the oxidized InP surface.

Shallow-deep definition

As described in section 4.4.4, the shallow-deep definition is done with photo-sensitive polyimide (PI2737). After the lithography, the pattern is hard-baked in a programmable vacuum oven that increases the temperature gradually to avoid bubble formation. The final curing temperature is 325 °C.

Deep etch

The deep waveguide etch is performed in the ICP system with the Cl_2:Ar:H_2 process described in section 4.3.4. The etch-time should be chosen such that the etch depth is at least a few hundred nm through the waveguide layer inside the DBR sections. The rest of the required etch depth (at least 1.5 µm through the waveguide film inside the DBR sections) will be added by the shallow etch. The polyimide can be removed with O_2 plasma stripping.

Shallow etch

The shallow etch is performed with an ICP CH_4:H_2 process. This process can etch smooth waveguides with a controlled etch rate. Usually a few etching and measurement steps are needed to determine the etch rates and to end up at the right etch depth, 100 nm into the waveguide layer.

Surface passivation

The SiO_x etching mask and any SiO_x deposited on the sidewalls is removed by BHF. Next, the structure is covered by a 75 nm thick PECVD SiO_x layer to passivate the deep-etched waveguides and to increase the adhesion of the BCB used in the planarization step.
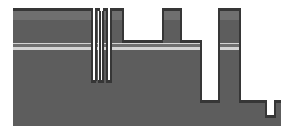
Planarization

To further increase the adhesion of the BCB, first a layer of adhesion promoter (AP3000) is spun on the sample. Then a single layer of BCB (Cyclotene 3022-46) is spun. The sample is baked in a vacuum oven using a recipe in which the sample is heated gradually in several steps until the final temperature of 325 °C is reached. This is the same temperature as will be used later in the annealing step.

Passive waveguide protection with SiO_x

In complex circuits it is quite common that there are electrical leads that cross passive waveguides. Additionally the metal that is used for the contacts does not adhere very well on the BCB. Therefore a 400 nm thick SiO_x layer is deposited by PECVD.

BCB removal

In order to make the cleaving of the chip easier, the BCB needs to be removed at those places. A lithography step with AZ4533 positive resist is used to first open the SiO_x using BHF. The photoresist can easily be removed with acetone. Next, an RIE process is used to remove the BCB, using the SiO_x pattern as a mask.

69
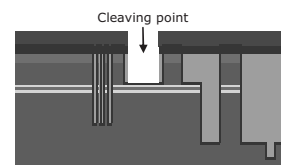
Contact opening

To make the electrical contacts on the SOAs we have to open the SiO$_x$ layer at those places. We use another AZ4533 lithography step, followed by a CHF$_3$ RIE process to etch the SiO$_x$ layer. The photoresist is removed by a 1 min. O$_2$:CHF$_3$ 20:4 sccm RIE process, which breaks to top of the resist layer, followed by acetone and IPA spraying and another O$_2$:CHF$_3$ plasma to remove any remaining residues.
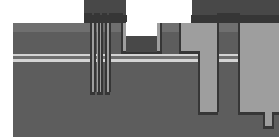
Metallization

For the metallization we use negative-resist lithography. Once the pattern is defined we first remove about 100 nm of the InGaAs contact layer with H$_2$SO$_4$:H$_2$O$_2$:H$_2$O 1:1:100 in order to obtain a clean surface. Then we deposit Ti/Pt/Au 60/75/300 nm metal contacts by e-beam evaporation and lift-off in acetone. Also the backside of the sample is metalized by the same layer stack. The sample is subsequently annealed at 325 °C for 30s.
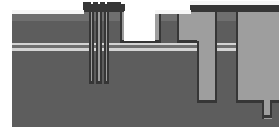
Plating

To assure uniform current injection in long gain blocks, we increase the metal thickness by an electroplating process. For this purpose we first deposit a 100 nm gold seed layer by sputtering. Then we define the plating pattern with AZ4533 positive photoresist. 40 cycles of electroplating deposit a gold layer of about 1 μm thick on all contacts. The photoresist can be removed by stripping with O$_2$ plasma and acetone. Finally the Au seed layer is removed by etching the gold layer briefly in a potassium cyanide (KCN) solution.

Cleaving & finishing

The last step is to cleave the chips and mount them on copper chucks using an electrical- and thermal conductive epoxy resin.

4.7 Conclusion

In this chapter the fabrication process that was developed to realize deeply etched DBR gratings in complex PICs was described. First an investigation of the e-beam lithography was done. There is was shown that a full proximity correction of the DBR pattern is not necessary when the DBRs are written separately from the waveguides. To realize this, a new 3-level masking process was developed using chromium as an intermediate layer, which allows the combination of EBL and optical lithography.

To realize the deeply-etched DBR gratings a new etching process was developed. An investigation of the ideal parameter settings to obtain straight and smooth sidewalls with minimal lag effect was conducted. The new Cl_2:Ar:H_2 process can be used to create 1st order air filled gratings as well as 3rd order BCB filled gratings.

Changing to this new etching process also has consequences on other process steps. A new shallow-deep process was described and also the method for planarization was changed. The full process flow for active-passive PICs with deeply etched DBR mirrors was described in the previous section.

The new fabrication process adds the DBR mirror building block to the existing range of building blocks (shallow- & deep waveguides, SOAs, phase modulators, etc.). The addition of the DBR mirrors does not compromise the other components.

Chapter 4

References

1 M.J.R. Heck, "Ultrafast Integrated Semiconductor Laser Technology at 1.55 μm", Chapter 2, PhD Thesis, TU Eindhoven, The Netherlands, 2008

2 Zeon Corporation (http://www.zeon.co.jp/)

3 T.H.P. Chang, "Proximity effect in electron-beam lithography", J. Vac. Sci. Technol., Vol. 12, No. 6, 1975

4 L. Stevens, R. Jonckheere, E. Froyen, S. Decoutere and D. Lanneer, "Determination of the proximity parameters in electron beam lithography using doughnut-structures", Microelectronic Eng. 5, pp 141-150, 1986

5 W. Patrick and P. Vettiger, "Optimization of the proximity parameters for the electron beam exposure of nanometer gate-length GaAs metal-semiconductor field effect transistors", J. Vac. Sci. Technol. B, Vol. 6, No. 6, 1988

6 C.W. Lee, D. Nie, T. Mei and M.K. Chin, "Study and optimization of room temperature inductively coupled plasma etching of InP using Cl2/CH4/H2 and CH4/H2", J. of Crystal Growth 288 (2006) 213-216

7 R. J. Shul, G. B. McClellan, R. D. Briggs, D. J. Rieger, S. J. Pearton, C. R. Abernathy, J. W. Lee, C. Constantine, C. Barratt, "High-density plasma etching of compound semiconductors," J. Vac. Sci. Technol. A 15, pp. 633, 1997

8 J. Etrillard, P. Ossart, G. Patriarche, M. Juhel, J. F. Bresse, and C. Daguet, "Anisotropic etching of InP with low sidewall and surface induced damage in inductively coupled plasma etching using SiCl₄," J. Vac. Sci. Technol. A 15, pp. 626, 1997

9 F. Karouta, B. Docter, E.J. Geluk, M.J.H. Sander-Jochem, J.J.G.M. van der Tol and M.K. Smit, "Role of Temperature and Gas-Chemistry in micro-masking of InP by ICP Etching", Proc. 18th annual IEEE/LEOS 2005, pp.987-988

10 Y.C. Zhu , F. Karouta, E.J. Geluk,T. de Vries, J.J.G.M. van der Tol and M.K. Smit, "ICP Etching of InP and its Applications in Photonic Circuits", Proc. IEEE/LEOS Benelux 2003, pp.81-84

11 S. Bouchoule, G. Patriarche, S. Guilet, L. Gatilova, L. Largeau and P. Chabert, "Sidewall passivation assisted by a silicon coverplate during Cl2–H2 and HBr inductively coupled plasma etching of InP for photonic devices", J. Vac. Sci. Technol. B 26(2), Mar/Apr 2008

12 K.H. Smith, J.R. Wasson, P.J.S. Mangat, W.J. Dauksher and D.J. Resnick, "Cr absorber etch process for extreme ultraviolet lithography mask fabrication", J. Vac. Sci. Techn. B, Vol. 19, nr. 6, 2001

13 S. Mukkavilli, R.W. Pasco, M.S. Farooq and M.J. Griffin, "Plasma processes for thin film surface treatment", Proc. 40th Electronic Components and Technology Conf., pp 737-745, May 1990

14 R.G. Broeke, A Wavelength Converter Integrated with a Discretely Tunable Laser for Wavelength Division Multiplexing Networks, Ph.D. thesis, Delft University of Technology, Delft, The Netherlands, 2003
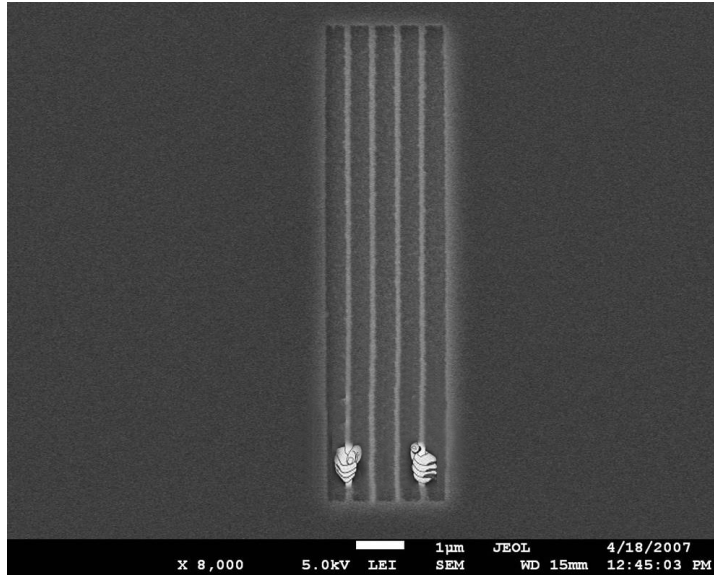
"Micro-prison"

ZEP on SiO_x

5 Characterization of deeply etched DBR mirrors

5.1 Introduction

Measuring the reflectivity of a mirror is a complicated process where it is often difficult to distinguish the mirror reflectivity from other device parameters like waveguide loss or gain, the coupling from the light in and out of the chip and other material parameters like internal quantum efficiency (η_i) etc. Various results on deeply etched DBR mirrors have been reported in literature [1,2,3]. Often high mirror reflectivities (95-99%) are claimed, but all of these results were obtained making assumptions on the value of one or more of the above parameters. Furthermore, the results reported are only valid for the lasing wavelength of the fabricated devices, while in complex PICs it is often necessary to know the full spectral response of the DBR mirrors.

This chapter describes the characterization of various chips with deeply-etched DBR mirrors, avoiding most of the issues mentioned before. A number of measurement methods are presented. These are used to characterize a number of chips with increasing fabrication complexity.

The first chip is a simple passive waveguide chip with straight waveguides and deeply-etched mirrors fabricated in a single (deep) etch step. A method to characterize the DBR reflectivity based on Fabry-Perot resonances is introduced.

Next, a series of deeply etched lasers is presented. These lasers were also processed in a single-step etching process, but with an all-active layer stack. In this section it is shown that the all-deep processing has negative influence on the laser properties and that therefore a combination of deeply-etched DBR mirrors and shallow etched waveguides would be beneficial.

Such a deep-shallow laser is presented in section 5.4. This improves the laser performance. For the characterization of the DBR mirrors in these devices a new sub-threshold characterization method was developed. This method allows the full characterization of the DBR reflectivity over a wide wavelength range.

The reflectivity values obtained with this method are much lower than what would be expected from simulations. This is due to the fact that the lasers are processed using all-active material, which is highly absorbing when there is no current applied to it, which is the case at the DBR mirrors. In the last section of this chapter some shallow-deep active-passive laser devices were characterized in which the DBR mirrors are realized in passive waveguides. It is shown that in these devices the mirror reflectivity matches quite well with the values expected from simulations.

In the following sub-sections each time first a chip is introduced, then the characterization method is explained and then the measurement results are given. The chapter concludes with a discussion of the different methods and the results that are obtained.

5.2 Deeply-etched DBR mirrors in passive waveguides

Passive waveguides are the simplest building blocks in a photonic integrated circuit, because they can be made with a minimal set of processing steps. This section describes the characterization of DBR mirrors in passive waveguides. First the chip layout and the fabrication process are described. Then the characterization method is explained followed by the results obtained with this method. The section concludes with a discussion of the applicability of the method for characterizing deeply etched DBR mirrors.

5.2.1 Chip layout & fabrication
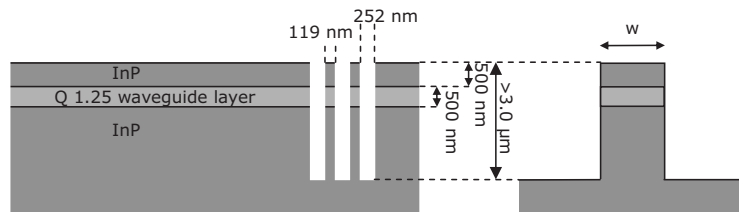
Figure 5.1: Side-view (left) and cross-section (right) of the passive waveguide structure with deeply-etched DBR mirror

The waveguides described in this section are created in a single growth step InP/InGaAsP/InP double heterostructure, with a Q1.25 passive core layer. Several mask layers are added to this layer stack and an EBL/optical lithography combination as described in section 4.4.3 is used to create a waveguide pattern containing deeply-etched DBR gratings. This pattern is transferred into the semiconductor material with a single deep-etch step followed by a planarization step using BCB. A schematic picture of the waveguide and the DBR mirror is given in figure 5.1. The dimensions of the DBR grating correspond to a 1st order grating for λ=1.55 μm, assuming an effective refractive index of the waveguide of N_{eff}=3.25 and a refractive index of the BCB of n_{BCB}=1.54.

5.2.2 Characterization of DBR mirrors in passive waveguides
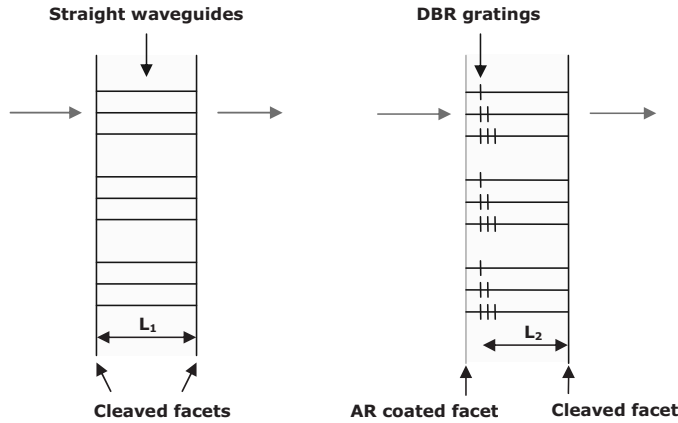
Figure 5.2: Two passive chips used to characterize waveguide propagation losses (left chip) and DBR reflectivity (right chip). Both chips are 5 mm long, the DBR mirrors are positioned 1 mm from the coated facet, e.g. L_1 = 5 mm, L_2 = 4 mm

The characterization of the deeply etched DBR mirrors in passive waveguides is based on determining the Fabry-Perot cavity resonances. The sample that is used for this characterization contains a number of straight waveguides with waveguide widths varying between 1.0 μm and 4.0 μm. The sample is cleaved to obtain two 5 mm long chips, which are shown in figure 5.2. The left chip contains only the waveguides and is used to determine the propagation losses, while the right chip contains waveguides with DBR gratings and is used to determine the DBR reflectivity. One of the facets of the DBR chip is coated with an anti-reflection (AR) coating, so that only one resonance cavity is present.

Straight waveguides

Cleaved facets

Measure Fabry-Perot fringe pattern

Calculate propagation loss

$$\alpha = -\frac{1}{L_1}\ln\left(\frac{1}{\sqrt{R_1 R_2}}\frac{\sqrt{C}-1}{\sqrt{C}+1}\right)$$

$C = P_{on}/P_{off}$

DBR gratings

Cleaved facet

AR coated facet

Measure Fabry-Perot fringe pattern

Calculate DBR reflectivity

$C = P_{on}/P_{off}$

$$R_2 = \frac{1}{R_1}\left(\frac{\sqrt{C}-1}{\sqrt{C}+1}e^{\alpha L_2}\right)^2$$
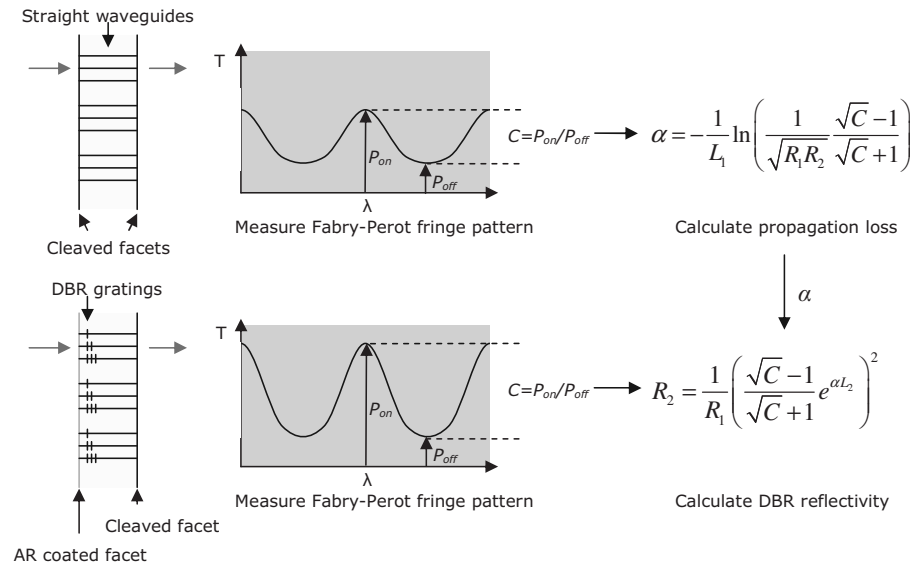
Figure 5.3: Schematic presentation of the measurement method used to characterize the DBR reflectivity

The characterization process is schematically shown in figure 5.3. The cleaved facets of the first chip are used as reference mirrors to determine the waveguide losses. Light from a tunable DFB laser is coupled into the waveguides and the transmitted Fabry-Perot fringe pattern is recorded. The contrast C between the on-resonance and off-resonance transmission gives us the propagation loss α using the following formula [4,5]:

$$\alpha = -\frac{1}{L_1}\ln\left(\frac{1}{\sqrt{R_1 R_2}}\frac{\sqrt{C}-1}{\sqrt{C}+1}\right)\quad\left[cm^{-1}\right] \tag{5.1}$$

In this equation C is given by the ratio of the on- and off-resonance transmission power (P_{on}/P_{off}), L_1 is the chip length and R_1 and R_2 are the facet reflectivities. This equation is commonly known as the Hakki-Paoli method, which is valid for low contrast values (e.g. low reflectivity/relatively high losses/long cavities). For higher contrast values it is better to do a complete curve fit of the resonance peaks with an Airy function as described in [6], but in this case the cavity length is assumed to be sufficiently long.

The facet reflectivities can be calculated using the program 'MIRF' developed by ETH Zurich [7]. This program first calculates the 2D mode profile in the waveguide using a finite difference method and then decomposes the field into a set of plane waves. For each plane wave the reflectivity with the waveguide facet is calculated and the reflected field is

reconstructed. The calculated facet reflectivities as a function of the waveguide width for these deeply-etched waveguides are given in figure 5.4.

Calculated cleaved facet reflectivity
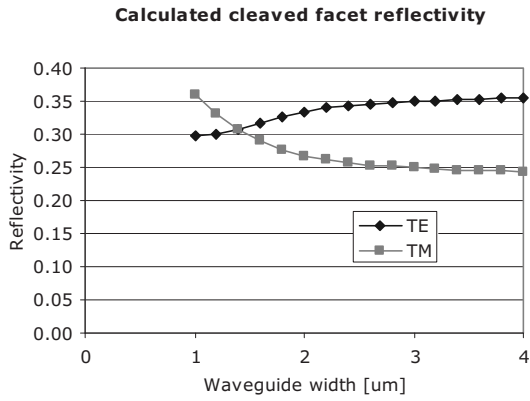
Figure 5.4: Calculated facet reflectivities as a function of waveguide width for deeply-etched passive waveguides

When the propagation losses are known, a similar transmission measurement is performed on the chip containing the DBR mirrors. Again the contrast ratio between the on- and the off-resonance transmission signal is recorded, but this time it is used to determine the reflectivity of the DBR mirror using the same equation as given in 5.1, but differently formulated:

$$R_2 = \frac{1}{R_1}\left(\frac{\sqrt{C}-1}{\sqrt{C}+1}e^{\alpha L_2}\right)^2 \qquad \textbf{(5.2)}$$

5.2.3 Results
First the propagation losses were measured with a temperature controlled DFB laser. At room temperature this laser emits at a wavelength of 1534.8 nm. The wavelength is tuned by cooling the laser. The exact wavelength of the laser is not recorded, but the total change in wavelength is less than 1 nm.

79
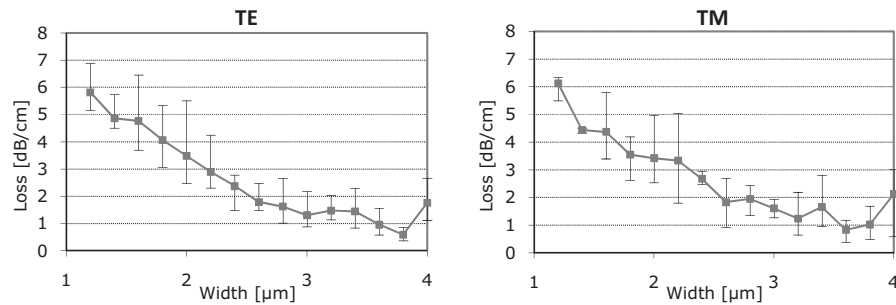
Figure 5.5: Propagation loss as a function of waveguide width for deep etched passive waveguides. The squares show the average value. The error bars indicate the maximum and minimum recorded propagation loss. For each waveguide width 4-6 waveguides were measured.

The results of the propagation loss measurements for both TE and TM polarizations are shown in figure 5.5. The propagation losses decrease as the waveguide width increases. This is due to the fact that sidewall roughness is the main cause of the loss. In wider waveguides, the modal field intensity is lower at the sidewall and thus the effect of roughness scattering is less.

There is a relatively large spread in the measured points. This is attributed to fabrication imperfections, which can occur anywhere along the 5 mm long waveguides: a high loss waveguide in the part of the chip used for the loss determination, might well be a low loss waveguide in the chip used for characterizing the DBR reflectivity and vice versa. Therefore the averages, as well as the minimum and maximum values, were used to calculate the DBR reflectivities.
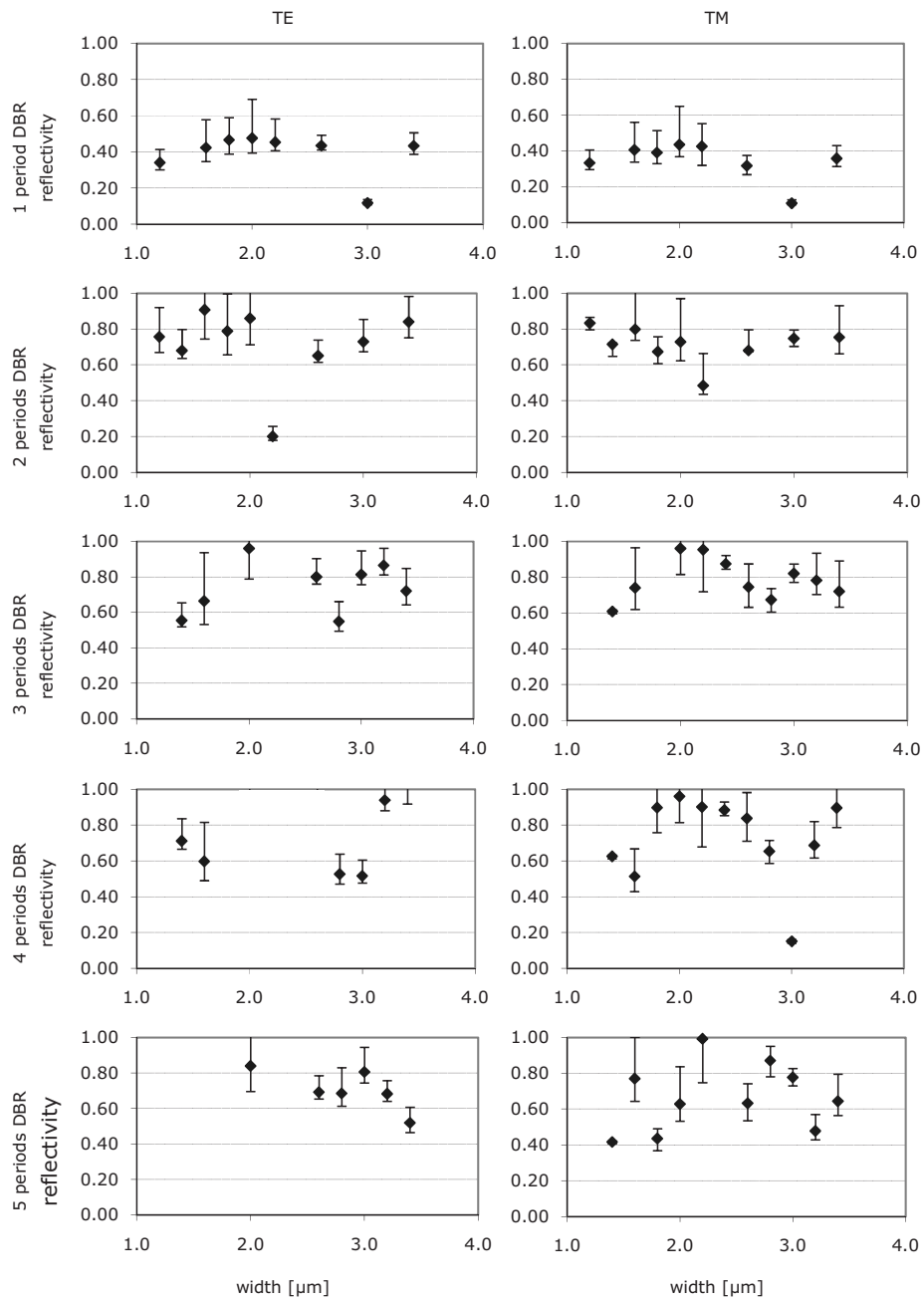
Figure 5.6: DBR reflectivity as a function of waveguide width for TE polarization (left) and TM polarization (right). The error bars indicate the variation of the reflectivity caused by the variation in propagation loss

Chapter 5

The results of the DBR reflectivity measurements are shown in figure 5.6, plotted both for TE and TM polarization as a function of the waveguide width. The solid points show the reflectivity value obtained by using the average propagation loss found in figure 5.5. The error bars indicate the variation of the reflectivity caused by the variation in propagation loss values.

The large spread in the data points is caused by the fact that the measured reflectivity value is constructed from two transmission measurements. This increases the total measurement error. Since the cavity length L_2 is quite large (4 mm), the method is quite sensitive to variations in propagation loss.

Figure 5.7 shows all reflectivity data combined in two graphs, plotted as a function of the number of grating periods. In this figure also the simulated reflectivity calculated with a 2D BEP algorithm as described in section 2.3 is plotted. For the gratings with 1 or 2 periods the measured data matches reasonably well with the simulations. For 3 periods and more, however, there is a large spread in the data points and most points are below the simulated curve.

This effect is attributed to the fact that the transmission signal becomes smaller as the reflection of the DBR increases. This means that the alignment of the input light is more difficult and the signal to noise ratio deteriorates. Therefore the measurement accuracy decreases for higher number of periods.
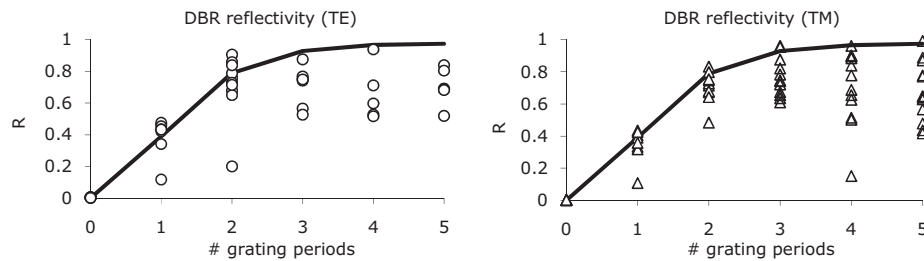
Figure 5.7: DBR reflectivity as a function of number of grating periods. The left figure shows TE reflectivity, the right figure the TM reflectivity. The solid lines show the simulated values.

5.2.4 Conclusion

In this section we presented a characterization method for deeply-etched DBR gratings in passive waveguides based on Fabry-Perot transmission measurements. It is a very simple measurement procedure, that is not affected by variations in the coupling efficiency from and to the chip. Furthermore it only requires a passive waveguide chip, fabricated in a single etch step. The method also has a few disadvantages: first, for high reflective DBR mirrors, the transmission signal is very low, resulting in a high noise level on the measurement results. Second, the need for 2 measurements to obtain a single measurement result is not beneficial for the accuracy. And finally the method only gives

measurement result is not beneficial for the accuracy. And finally the method only gives information about the reflection at a small wavelength range, determined by the thermal tuning laser used in the measurement setup. In section 5.6.2 a method to characterize single period DBR mirrors is presented that circumvents most of these drawbacks.

5.3 All-deep DBR lasers

The measurement method presented in the previous section used a DFB laser as an light source. Especially for high reflective mirrors, with only low transmission, alignment of the input coupling can be difficult. This can be avoided when the light used for characterization is actually generated on the chip itself. This section describes the characterization of DBR mirrors using DBR lasers having 1 cleaved facet and 1 DBR mirror.

5.3.1   Chip layout and fabrication

#	Material	d [nm]	doping
III-4	p-InGaAs	300	1.5e19
III-3	p-InP	1000	1e18
III-2	p-InP	300	5e17
III-1	p-Q1.25	20	3e17
I-7	p-InP	200	3e17
I-6	p-Q1.25	50	1e17
I-5	Q1.25	140	n.i.d.
I-4	Q1.58	120	n.i.d.
I-3	n-Q1.25	190	6e16
I-1	n-InP	500	3.5e17
I-0	n-InP	sub	1-4e18
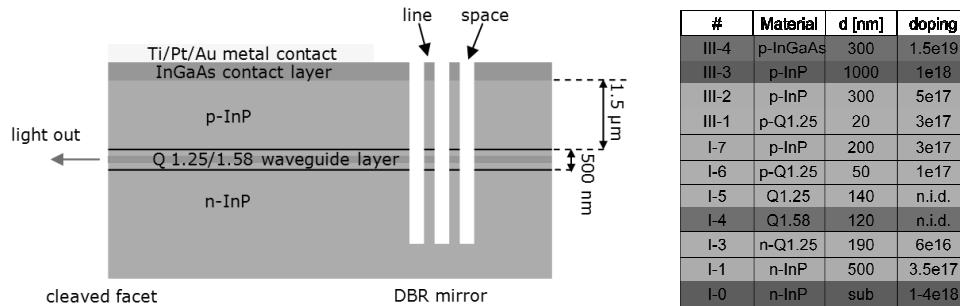
Figure 5.8: Side view of an all-deep all-active DBR laser. The table on the right shows the composition, thickness and doping levels of all the layers. The thin etch stop layer (layer III-1) is not shown in the left picture.

The lasers described in this section were processed in a similar manner as the passive waveguides from the previous section. They were etched in a single etch-step, etching through the waveguide layers in the DBR sections as well as in the amplifier sections. A schematic picture is shown in figure 5.8. Note that the waveguide layer now contains a 120-nm thick Q1.58 active layer surrounded by 190-nm thick Q1.25 confinement layers.

The laser cavities are formed by a cleaved facet and a DBR mirror. Current is applied through a top metal contact and flows through the active layer towards the n-doped substrate. The substrate has a backside ground contact (not shown in figure). Note that the semiconductor lines in the DBR mirror are not contacted and therefore not electrically pumped. The light leaves the laser through the cleaved facet. The light that is transmitted through the DBR mirror is absorbed in the (un-pumped) active waveguide on the right.

order	filling	line	space
1st order	air	120 nm	390 nm
3rd order/1st order	air	360 nm	390 nm
1st order	BCB	120 nm	250 nm
3rd order	BCB	360 nm	750 nm

Table 5.1: Different types of DBR lasers that were processed

In this chip the waveguide width is varied between 1.0 and 3.0 µm. Four different DBR designs were used: 1st and 3rd order combined with either air or BCB filling. The size of the lines and spaces in the DBR sections of these designs are shown in Table 5.1. The mixed 3rd order/1st order design that is shown in the second row of the table consists of 3rd order lines ($l_{line} = ¾ * λ / N_{eff}$) and 1st order spaces ($l_{space} = ¼ * λ / n_{air}$).
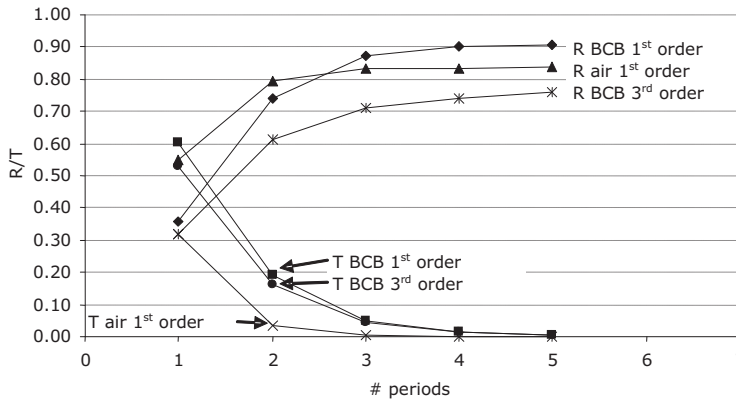
Figure 5.9: Simulated reflectivity (R) and transmission (T) of 1.5 µm wide deep etched 1st and 3rd order DBR gratings with air and BCB filling. For this simulation a 2D FDTD algorithm (see section 2.4.1) was used. The etch depth was 3 µm.

The simulated reflectivity and transmission as a function of the number of DBR periods is shown in figure 5.9. The gratings with 3rd order lines and 1st order spaces filled with air have been left out for clarity. The behavior of these gratings is similar to the 1st order air filled designs, since the loss in the grating is mainly caused by the non-guiding air-gaps.
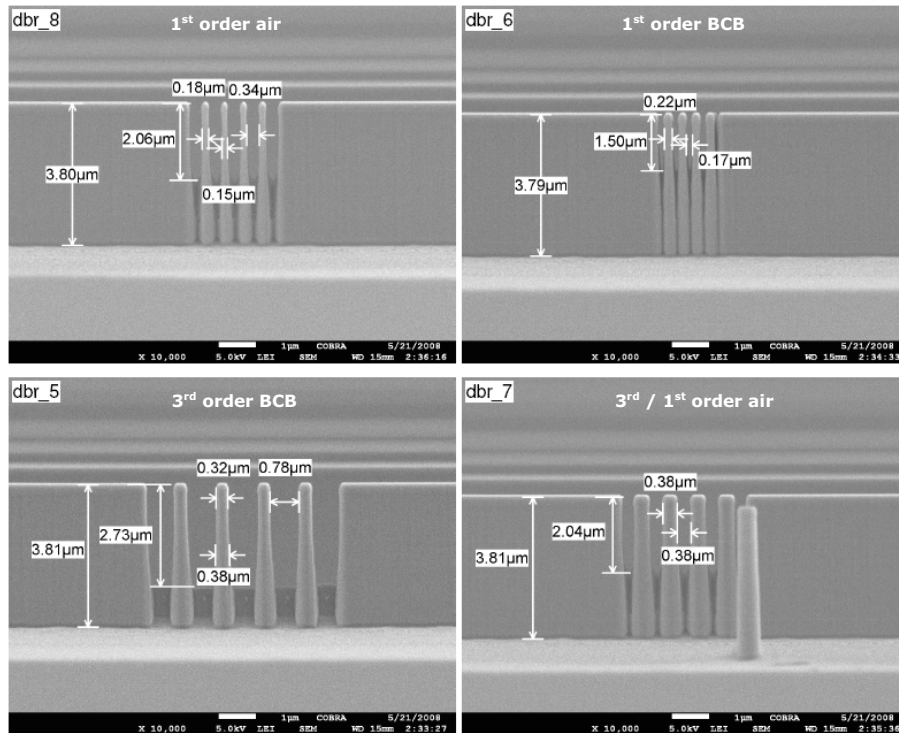
Figure 5.10: SEM images of different deeply-etched DBR gratings designed as 1st order filled with air (upper left, dbr_8), 1st order filled with BCB (upper right, dbr_6), 3rd order BCB (lower left, dbr_5) and 3rd/1st order air (lower right, dbr_7). Waveguide width is 2.2 μm, etching time was 2 minutes.

Order	filling	line	space	etch depth
1st order	air	150 nm	340 nm	2.06 μm
3rd order/1st order	air	380 nm	380 nm	2.04 μm
1st order	BCB	220 nm	170 nm	1.50 μm
3rd order	BCB	320 nm	780 nm	2.73 μm

Table 5.2: DBR dimensions as measured in the test chip

In order to test the fabrication process, first a test sample was processed. Inspection of the test sample in the SEM (see figure 5.10) shows that the actual DBR dimensions are slightly differing from the designed values. The measured line/space ratio and etch depth are summarized in Table 5.2. Note that the etched profiles are not completely straight. The DBR lines tend to broaden as the etch depth increases. Also the lag effect in the etching process is clearly visible. It is most pronounced in the 1st order BCB filled grating. Due to the same effect, the final etch depth is also lower in the wider waveguides. For the wide waveguide devices and the 1st order BCB filled gratings the final etch depth is much lower than the designed 3 μm.

In order to maximize the etch depth between the DBR lines, the actual laser sample was etched for 2.5 minutes instead of the 2 minutes that were used in the test sample. This increased the total etch depth to 4.3 µm instead of 3.8 µm.
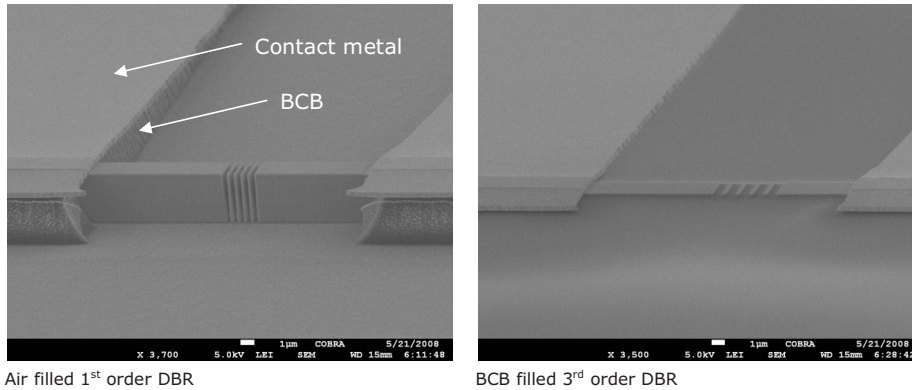
Air filled 1st order DBR   BCB filled 3rd order DBR

Figure 5.11: SEM images of an air-filled DBR laser (left) and a BCB-filled DBR laser (right)

After etching the chip is planarized using BCB (see section 4.5). Next the metal contacts are applied. In the areas of the chip that contain the air-gratings the BCB is etched away using an O_2:CHF_3 RIE process. This is shown in the SEM images in figure 5.11.

5.3.2 Characterization of DBR mirrors in deeply etched lasers

The characterization of the deeply etched mirrors will be done using the threshold current density of the lasers. Since the gain required for lasing is determined partly by the reflectivity of the laser mirrors, the threshold current density gives an idea of the DBR reflectivity. However, to get an exact value for the DBR reflectivity, the gain from the active waveguide as a function of the injected current should be known. In other words, a good gain model with appropriate parameters is required. Later in this section it will be shown that these lasers are not very suitable to obtain this. However, when comparing different deeply-etched lasers with each other, some conclusions about the reflectivity compared to cleaved facet mirrors can be drawn.

The fabricated sample was cleaved into different chips containing various laser lengths. The first chip was cleaved at 1 mm cavity length and did not contain any DBR mirrors, so the cavity is formed by 2 cleaved facets. This device can be used as a reference to compare with the DBR lasers. The threshold current density J_{th} as a function of waveguide width is shown in figure 5.12. These measurements were performed under CW operation at 12 °C.
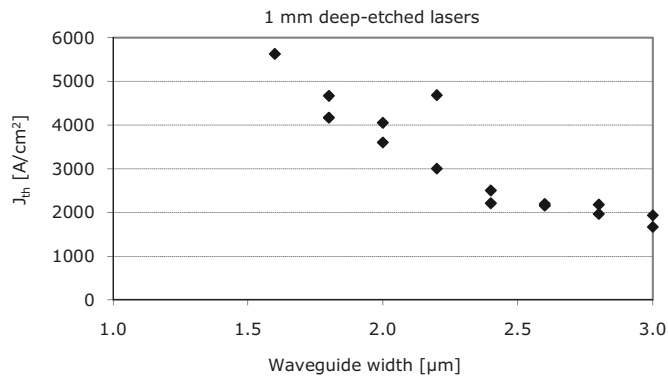
Figure 5.12: Threshold current density as a function of waveguide width of 1 mm long cleaved facet deeply-etched lasers.

The threshold current density increases as the waveguide width reduces. This is caused by two effects: First the waveguide propagation losses will be higher (as shown in figure 5.5), but more importantly, the leakage current along the sidewalls becomes more dominant. The devices with waveguide widths narrower than 1.6 µm would not operate at all.

Although the output power of these devices is low (around 0.5 mW before temperature roll off occurs), the threshold currents are stable over time, indicating that the passivation of the sidewalls is stable.

A second chip was cleaved with a length of 1.5 mm and contained 1st order air filled gratings 600 µm from one cleaved facet and 900 µm from the other cleaved facet. The threshold current densities are shown in figure 5.13. Again there is a strong dependence on waveguide width.
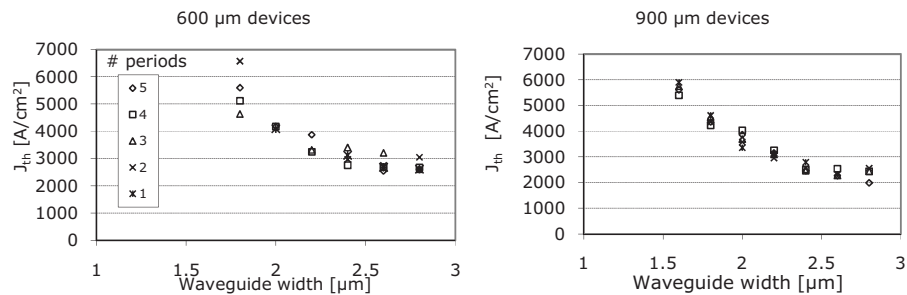
Figure 5.13: Threshold current densities of 1st order air filled DBR lasers

Chapter 5

The graph shows that there is no clear trend towards lower current densities with higher number of grating periods. This is unusual, since one would expect that when the mirror reflectivity is higher (larger number of grating periods), the gain required to compensate for the mirror losses (and thus to reach the lasing threshold), would be lower.

To explain the observed behavior, a simulation was performed using a simple rate equation model [8], with gain parameters taken from literature [6]. The threshold current density as a function of DBR reflectivity for DBR lasers of different cavity lengths and with different DBR reflectivity (R=10% - 100 %) is shown in figure 5.14. The graph shows that for longer cavity lengths, the difference in threshold current density due to the DBR reflectivity becomes very small. The graph also shows that a larger spread in threshold current densities is to be expected with short-cavity lasers.
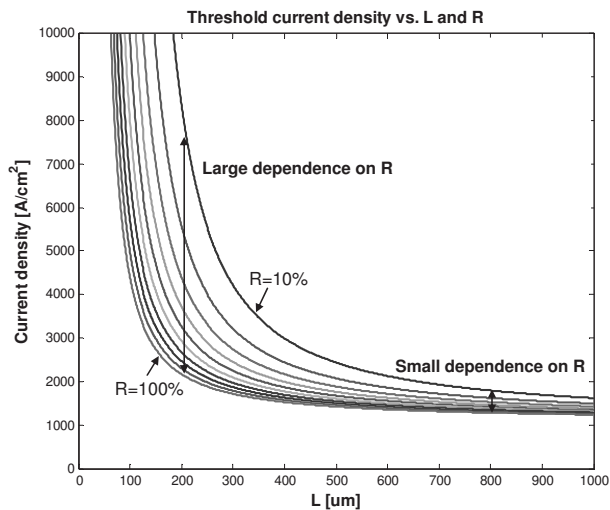
Figure 5.14: Rate equation model results showing threshold current density as a function of cavity length for lasers with 1 cleaved facet mirror and 1 DBR mirror (R=10% - 100% in steps of 10%).

100 µm devices
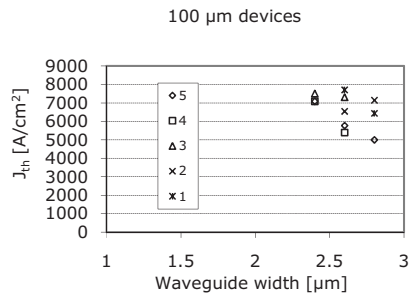
Figure 5.15: Threshold current densities for 100 µm DBR lasers with 1 cleaved facet and 1 3rd/1st order DBR grating filled with air.

A third chip with 100 µm long devices with $3^{rd}/1^{st}$ order air filled gratings shows a large spread in measured current densities (see figure 5.15). Only a few devices could be pumped hard enough to obtain laser operation. Again no clear trend between J_{th} and number of DBR gratings is visible, but the spread in measured values is much larger compared to the longer devices.

From the above results it is not possible to draw any quantitative conclusions on the strength of the reflection as a function of the number of periods. However, to have some idea of how the different types of DBR gratings compare to each other, we average the measured data from the devices of about 1 mm cavity length over the number of DBR periods. The results are plotted in figure 5.16.

Average threshold current densities deep-etched lasers
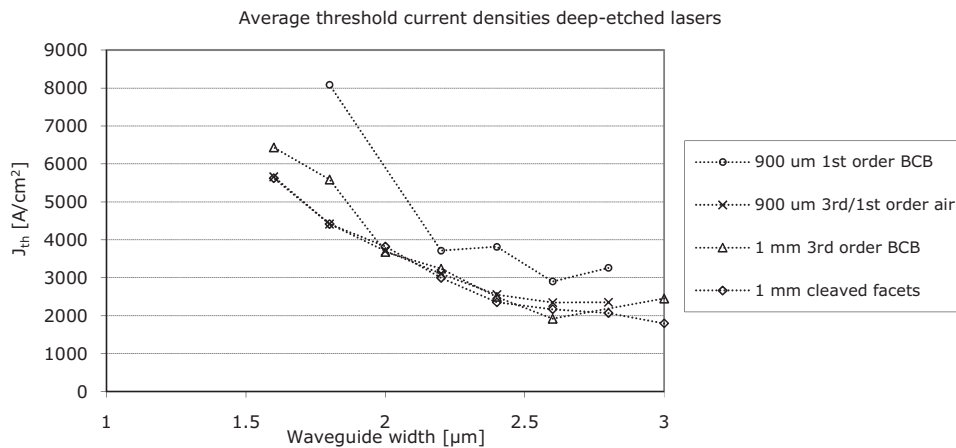
Figure 5.16: Average threshold current density as a function of waveguide width for various deeply-etched lasers with different type of mirrors.

The devices with 1st order BCB gratings have a higher J_{th} compared to the devices with similar cavity lengths. This is attributed to the reduced etch depth that was observed in figure 5.10. The reduced etch depth caused the reflected light to couple towards the substrate reducing the overall mirror reflectivity. We also see that the 1 mm long devices with a 3rd order BCB grating show similar threshold currents as the 1 mm cleaved facet lasers. This implies that the reflectivity of these DBR mirrors is comparable to that of a cleaved facet (0.3 – 0.35).

5.3.3 Conclusion

With the ICP process that was developed to etch deep DBR gratings with vertical side-walls it is possible to create deeply-etched lasers. However, the measured threshold current densities show a strong dependence on waveguide width, indicating large current leakage due to (non-radiative) recombination of the carriers on the sidewalls. This is probably caused by crystal damage due to the etching process. The threshold current is stable over time, which shows that the sidewalls are passivated well.

These laser devices are not very suitable to characterize the DBR reflectivities. This is due to 2 main reasons: First, the threshold current density of the longer devices depends only marginally on the mirror reflectivity. Second, the shorter devices require very high current densities to obtain laser operation. Device heating becomes a problem and therefore only a few lasers operate. Fabricating the lasers in a double etching technique, combining deeply etched mirrors with shallowly etched waveguides, can solve this problem. This is shown in the next section.

5.4 Deep-shallow DBR lasers

In the previous section it was found that short lasers are more sensitive to the DBR reflectivity than long devices. However, the required current densities to obtain laser operation are quite high and surface recombination can become a problem for fully deeply-etched devices. In this section another set of short-cavity devices is presented that was fabricated using a deep-shallow processing scheme.

5.4.1 Chip layout & fabrication

Shallow etched
SOA area

Deeply etched
DBR area
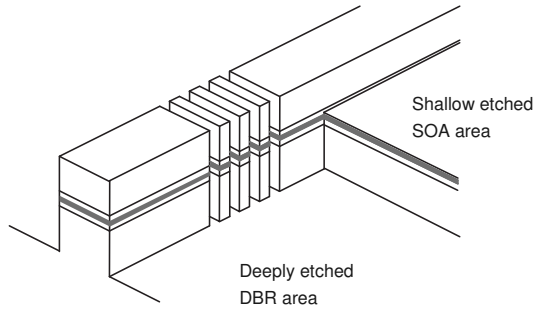
Figure 5.17: Schematic picture of a deep-shallow DBR laser. The active Q1.58 layer is highlighted in the picture.

The lasers described in this section are fabricated using the same layer stack as shown in figure 5.8, but the SOA sections are shallowly etched to a depth of just 100 nm in the waveguide film, as shown in figure 5.17. This leaves the active Q1.58 layer covered, which prevents surface recombination of the carriers. Moreover, the propagation losses are also lower in the shallow etched waveguides.

The fabrication details of the deep-shallow processing are given in sub-section 4.4.4. All lasers described in this section have 3rd order BCB-filled DBR gratings with a line/space ratio of 360/750 (nm). The reason for this choice is that it doesn't require etching away the BCB layer that is used for planarizing the device. Additionally the 3rd order design allows relatively large (750 nm) gaps in the DBR sections, which reduces the lag effect significantly compared to a 1st order design (250 nm gaps).

Deep etch:
 > 5 µm deep

Shallow etch:
 1.9 µm deep
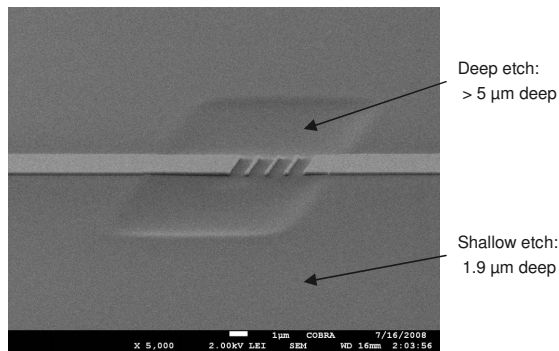
Figure 5.18: SEM image of deep-shallow DBR laser planarized with BCB.

The DBR sections are etched to a depth of 5 µm, while the shallow etched SOA ridges are 1.9 µm deep. A SEM image of a device planarized with a single layer of BCB is shown in figure 5.18. The deep-etched part is 10 µm long and 20 µm wide and is still visible as a

91

shallow depression in the BCB layer. The image demonstrates the excellent planarization properties of BCB.

5.4.2 Characterization of deep-shallow DBR lasers

For the characterization of the deep-shallow DBR lasers a threshold current density method was used, similar to the deeply-etched laser characterization that was described in section 5.3.2.
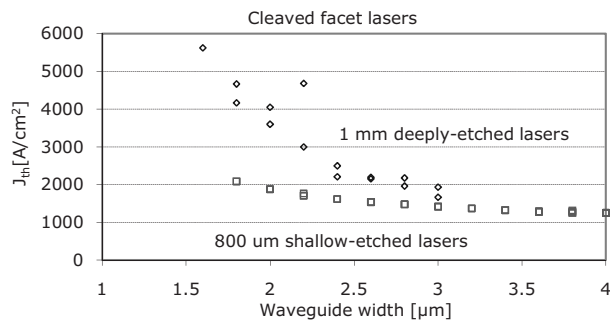
Figure 5.19: Threshold current density as a function of waveguide width for 1 mm deep etched lasers (diamonds) and 800 µm long shallow etched lasers (squares).

Again several chips were cleaved forming various laser lengths. First, 800 µm long lasers with two cleaved facets were measured. The threshold current densities are plotted as a function of waveguide width in figure 5.19. For comparison the values found for deeply-etched 1 mm long lasers (figure 5.12) are also given. The dependence of threshold current density on waveguide width is much smaller due to the absence of surface recombination. Also the spread in data points is smaller.
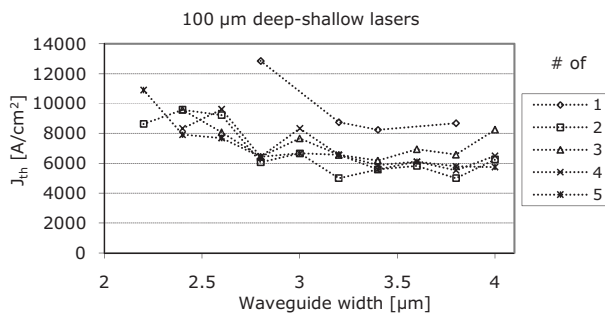
Figure 5.20: Threshold current density as a function of waveguide width for 100 µm long deep-shallow DBR lasers.

Next, the threshold current densities of 100 μm long lasers with one cleaved facet and one DBR grating were measured. The number of grating periods was varied between 1 and 5 periods. The results are shown in figure 5.20. The 1 period devices have a systematically higher threshold current density, indicating a lower reflectivity, but for a larger number of periods the reflectivity seems to be comparable since there is no visible trend towards lower J_{th}.

Compared to the fully deep etched lasers (figure 5.15), the yield of 100 μm devices is higher. This is mostly due to the fact that the shallow lasers can be pumped with a larger current without running into thermal problems. We expect that the threshold current density would be lower in the deep-shallow devices, since the current leakage due to the sidewall recombination is reduced (there is still surface recombination at the mirrors). However, when comparing the two types of lasers, this is not observed. This is attributed to the fact that the DBR reflectivity of the air filled DBRs in the deep etched lasers is higher than the BCB filled DBRs in the deep-shallow lasers (see simulated reflectivity in figure 5.9). Another difference is that the current injected in the deeply-etched lasers is concentrated completely in the waveguide, while in the shallow etched waveguides it can spread over a wider range, effectively reducing the carrier density.
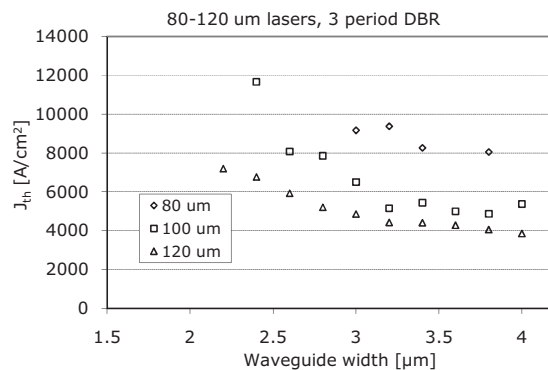
Figure 5.21: Threshold current density as a function of waveguide width for deep-shallow lasers with one cleaved facet and one 3rd order BCB filled DBR grating of 3 periods.

Figure 5.21 shows the threshold current density of 3-period DBR lasers with cavity lengths varying between 80 and 120 μm. In this plot it is shown that the spread in measured points increases with reduced cavity length, for devices with identical DBR mirrors. The devices with a cavity length of 80 μm were the smallest devices that were operating above laser threshold.

93

5.4.3 LI curves and spectra
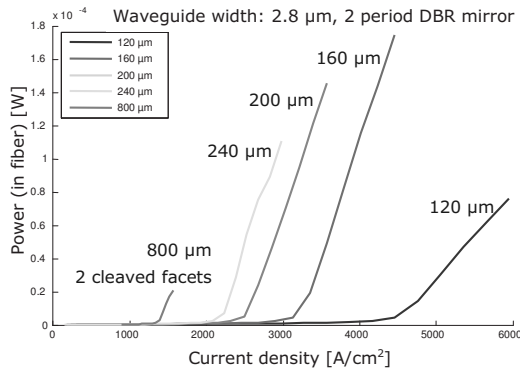
Figure 5.22: Output power as a function of current density of 2.8 µm wide deep-shallow lasers with 2 period 3rd order BCB filled DBR gratings.

In the previous sub-sections we have shown that with the double etching technology it is possible to get more operating lasers with short cavity as compared to the deeply-etched lasers. However, if we look at the output power as a function of current density for 2.8 µm wide 2-period DBR lasers of various lengths (plotted in figure 5.22), we see that the 120 µm long lasers have a lower efficiency than the longer lasers. This could be an indication that temperature effects are reducing the material gain at current densities above 4500 A/cm^2.
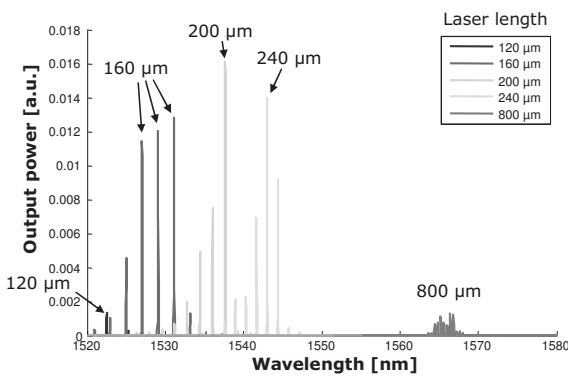
Figure 5.23: Lasing spectra of five different length lasers (2.8 µm waveguide width, 2 period DBR) just above threshold.

The lasing spectra of the same devices are shown in figure 5.23. A large shift in wavelength can be observed. This is due to the shifting gain spectrum caused by band filling. The shift is particularly large compared to the 800 µm reference device. It is therefore very difficult to extract accurate values for the DBR reflectivity, since the values needed to obtain a good

model for the gain of the material would be based on the data obtained from the 800 μm reference device, for example using a method as described in [6].

To circumvent this problem we have developed a method to study the DBR reflectivity using the same carrier density values for all devices. This method is described in the next section.

5.5 Sub-threshold characterization of DBR mirrors

In the previous sections it was shown that using the threshold current of a DBR laser to determine the DBR reflectivity has a number of drawbacks. Those are mainly caused by the fact that a good gain model is needed to determine the roundtrip gain at the threshold current density. This gain model is always fitted to a reference laser that has cleaved facets and a typical length in the order of 1 mm. To obtain accurate reflectivity results, however, the DBR lasers have to be much shorter. In these short lasers the threshold carrier density is much higher than the values to which the gain model was fitted, and therefore the gain model is not very suitable.

An additional problem of the 'threshold current'-method is that the DBR reflectivities obtained in this way are only relevant for the lasing wavelengths. However, it is also interesting to know the wavelength dependency of the reflectivity, preferably over a larger wavelength range.

Both problems (gain model required and narrow wavelength band) are overcome in the measurement method described in this section. It is based on measuring the Fabry-Perot fringe pattern of a short-cavity laser well below threshold, using the transparency current to have a well-defined operating point. This does not require a gain model to extract the reflectivity and gives information over a wide wavelength range.

The measurements were performed on the same deep-shallow lasers that were used in the previous section. The layout and fabrication was already described in sub-section 5.4.1. The new characterization method is explained in the next sub-section. Following this overview of the different measurement steps, each step is described in more detail in sub-sections 5.5.2 to 5.5.4. The results that were obtained using this method are described in sub-section 5.5.5, followed by a conclusion in sub-section 5.5.6.

5.5.1 Characterization of DBR mirrors in deep-shallow DBR lasers

The characterization method described in this section is based on measurements performed at the transparency carrier density (J_{tr}) of the active Q1.58 material. This carrier density can be determined very accurately with a method shown in sub-section 5.5.2.

95
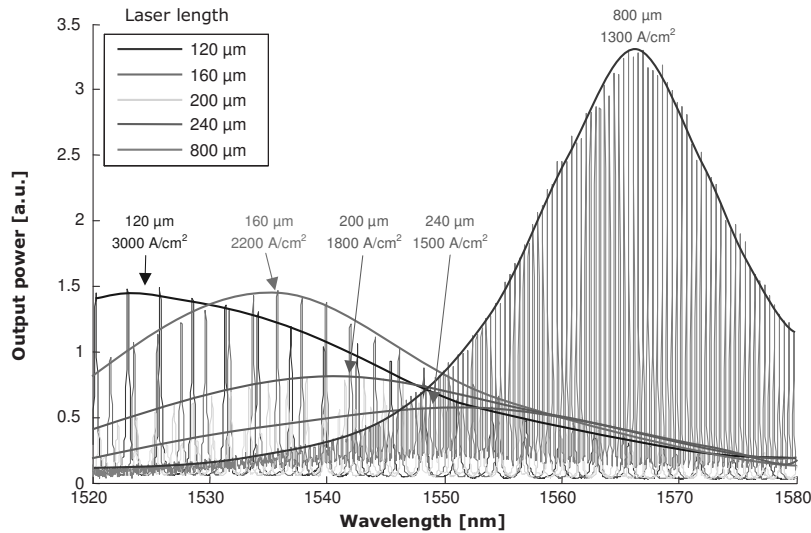
Figure 5.24: Sub-threshold spectra of the same lasers as shown in figure 5.23. The plotted envelopes show that the spectra overlap over a broad wavelength range.

Because the measurements are performed at a fixed carrier density for both the long reference laser with cleaved facets as well as the short DBR lasers, a gain model is not required. Furthermore, the transparency carrier density is smaller than the threshold current density ($J_{tr}<J_{th}$). Thus, the laser condition is not yet reached and the measured spectra from which the data is obtained are much wider. As an example some sub-threshold spectra (not necessarily at J_{tr}, since this is wavelength-dependent) are shown in figure 5.24. These spectra are taken from the same devices as those from which the lasing spectra in figure 5.23 are taken. There is a much larger overlap between spectra, in contrast to the situation when the devices are operated above threshold.

The method described in this section consists of 3 main steps:

1) measure the transparency current density $J_{tr}(\lambda)$
2) measure the propagation loss $a(\lambda)$ at transparency using a reference device
3) measure the reflectivities $R(\lambda)$ of short-cavity DBR lasers

These three steps are described in the following sub-sections.

5.5.2 Transparency current density

The method used for measuring the transparency current density is based on injecting an externally modulated optical signal into the laser and monitoring at which drive currents the external light is still absorbed (below transparency). In this situation the absorbed light generates extra carriers in the chip, which can be measured by looking at the voltage across

the device. When the current is increased to a level above transparency, the external light is amplified and carriers are taken away from the chip. This can also be observed by looking at the voltage.
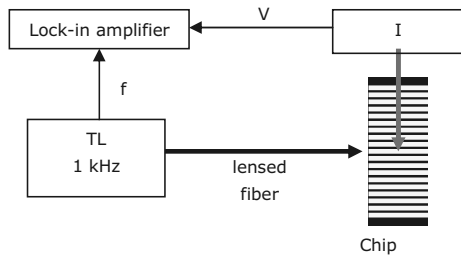
Figure 5.25: Setup to measure the transparency current density.

The measurement setup that was used to perform this experiment is shown in figure 5.25. The chip can be any laser chip (short or long, cleaved facet or not). In this example the 800 μm reference laser with 2 cleaved facets was used.

The tunable laser (TL) is modulated at 1 kHz and the influence on the voltage across the device is monitored using the lock-in amplifier. Then the current provided by the current source (I) is scanned. When the current is lower than the transparency current (I_{tr}), the current source has to provide less current to reach its setpoint due to the extra carriers from the absorbed signal. As a consequence the voltage across the device drops.

As the total current is increased, the absorption in the material decreases. The amplitude of the 1 kHz component of the measured signal decreases to zero when the current reaches I_{tr}. Above transparency, the injected TL light is amplified and takes away carriers in the active layer. The current source has to compensate this, causing the voltage to increase. The amplitude of the 1 kHz signal is now increasing again. So the minimum in the voltage amplitude indicates the transparency current.
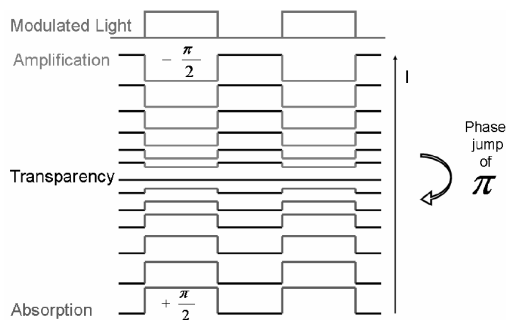
Figure 5.26: Impact of the modulated light from the tunable laser on the carrier density.

The transition between absorption and amplification is even more pronounced in the phase of the modulated signal. There is a 180° phase jump when the current goes through the transparency current. This is schematically shown in figure 5.26.

From the transparency current, the transparency current density J_{tr} can be determined. This value for J_{tr} is valid for all devices with the same waveguide width.
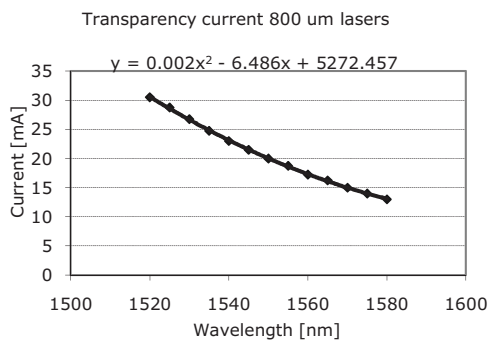
Figure 5.27: Transparency current of 800 μm reference device. The equation shows the fitted function which can be used to determine the transparency current for each wavelength.

The results of the transparency current measurements are shown in figure 5.27. The data in the plot was obtained from the 800 μm long reference device. We measured the transparency current for a wavelength range of 1520 – 1580 nm, with a 5 nm step size. Then we fitted a 2nd order polynomial through the points so we have an interpolated value for each wavelength.

5.5.3 Propagation loss in active waveguides
The transparency current measured in the previous step gives the current at which the Q1.58 active layer is transparent. However, the optical mode extends into the top and bottom cladding layers and since the material has a relatively high doping concentration, the mode still experiences a large propagation loss.
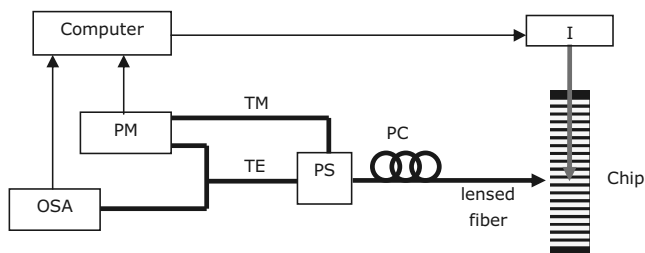
Figure 5.28: Setup to measure Fabry-Perot fringe pattern. I = current source, PM = HP power meter, OSA = ANDO optical spectrum analyzer, PS = polarization splitter, PC = polarization controller.

To determine the propagation loss we use the reference device with two cleaved facets, so we know the reflectivities of the end faces. The measurement setup is shown in figure 5.28. The Polarization Controller (PC) is adjusted in such a way that when the laser is operated above threshold, emitting mostly TE polarized light, most of the light is collected in the TE-branch after the Polarization Splitter (PS).

The Optical Spectrum Analyzer (OSA) is used to scan small pieces of the spectrum (5 nm) for different drive currents. These drive currents are chosen so that they cover the transparency current values obtained from figure 5.27. From the OSA scans the loss is extracted using the Fabry-Perot equation (see equation 5.1).
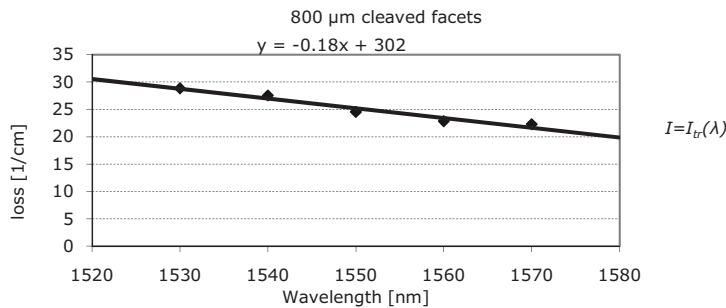
Figure 5.29: Propagation loss at the transparency current density. The equation shows the fitted function.

This process is repeated for several wavelengths so we obtain a loss value as a function of wavelength and drive current. The loss at the transparency current can then be obtained by linear interpolation. The loss obtained in this way is shown in figure 5.29. A linear function is fitted through the measured points to obtain a loss value for each wavelength, which will be used later on to determine the DBR reflectivity.

5.5.4 DBR mirror reflectivity

The measurement of the DBR reflectivity uses the same measurement setup as the determination of the propagation loss (figure 5.28). The OSA records the spectrum as a function of the current. The current range over which the measurements are performed is taken from the transparency current density $J_{tr}(\lambda)$ characterization.
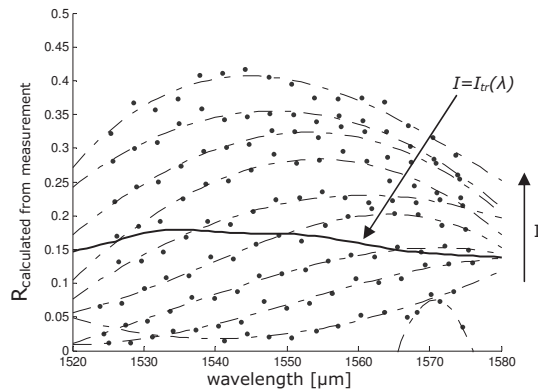
Figure 5.30: Calculated mirror reflectivity obtained from measurements on a 100 µm DBR laser with 1 period DBR mirror. The dots represent the resonance peaks for different drive currents. The dashed lines show the fitted 3rd order polynomials to obtain a value for each wavelength. The solid line shows the final value for the reflectivity at the transparency current density.

To determine the DBR reflectivity (R) the re-written FP equation that is given in eq. 5.2 is used. This equation requires the contrast C of the FP fringes and the propagation loss. C comes from the measured spectra, while the value for the propagation loss comes from the measurements described in sub-section 5.5.3. However, this loss value is only valid when the device is operated at the transparency current density, which is wavelength dependent. This means that the value for R (dots in figure 5.30) is overestimated when the drive current (I) is higher than the transparency current at that wavelength and underestimated when I is lower than I_{tr}.

In order to get the right value for R for each wavelength first a 3rd order polynomial function is fitted through each measurement result (dashed lines in figure 5.30). In this way an interpolated value for R for each wavelength is obtained. The final step is to linearly interpolate the R value between the measured currents so that we know the R value at the transparency current density (solid line in figure 5.30).

5.5.5 Results
Figure 5.31 shows the DBR reflectivity as a function of wavelength and number of DBR periods for a set of 100 µm long DBR lasers. The reflectivity value is lower than expected (see simulation results in Figure 2.21) and there is no trend towards higher reflectivities for a larger number of grating periods. A similar behavior is found for 160 µm long lasers (figure 5.32), although the reflectivity for the 2-period mirror is a little higher. Similar values are also observed in various other 2-period devices with different cavity lengths as shown in figure 5.33.
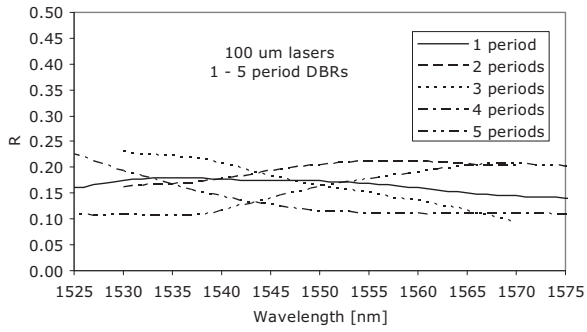
Figure 5.31: Measured reflectivity (R) as a function of wavelength for 1-5 period DBR gratings in 100 μm DBR lasers.
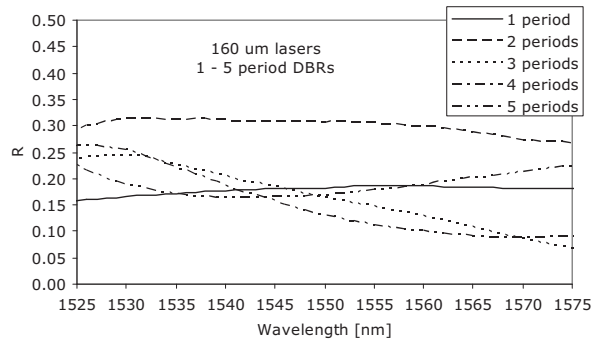
Figure 5.32: Measured reflectivity (R) as a function of wavelength for 1-5 period DBR gratings in 160 μm DBR lasers.
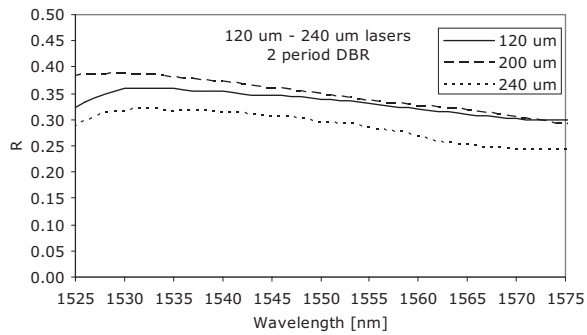
Figure 5.33: Measured reflectivity (R) as a function of wavelength for 2 period DBR gratings in 120 - 240 μm long DBR lasers.

101

There are several possible reasons for the low DBR reflectivity. First, the gratings were written using the EBL with an exposure dose obtained in a way as described in sub-section 4.2.5. However, by the time these samples were processed, the dose was only optimized for 1st order gratings filled with air. It is possible that the wider 3rd order gratings require a lower dose. The over dose will cause the grooves to become wider and the lines to become thinner, resulting in a lower reflection. This hypothesis is supported by the SEM images shown in figure 5.34. The top-part of the semiconductor lines in the DBR section that stick out of the BCB planarization layer seem smaller than the designed 360 nm (left image). However, when the BCB is etched away (right image) it is revealed that this reduction in size is not so big at the position of the waveguide layer.
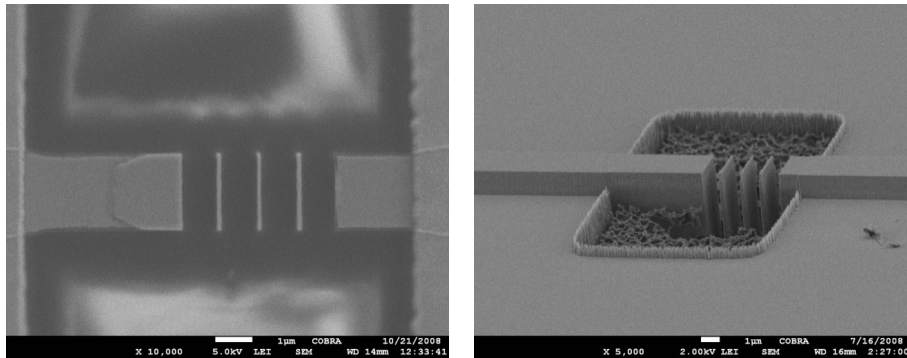
Figure 5.34: SEM images of a 4-period DBR grating filled with BCB (top-view, left image) and the same structure in a test sample where the BCB is etched away (right image). In the left image, the metal contacts are still partly visible at the edges of the picture. Some BCB residues are still visible in the deeply-etched area in the right image.

Another cause of the lower reflectivity is the fact that the DBR mirrors are connected to the amplifier section using an all-active material. The measurement method does not take into account any extra losses caused by this un-pumped waveguide section. Although this length is typically only 3-4 µm long (the actual value depends on the optical- to e-beam-lithography alignment), any extra loss in this waveguide reduces the final value for the reflectivity.

When we assume that no current from the amplifier spreads into the connecting waveguide (worst case scenario), the transmission in this waveguide can be approximated by the following equation:

$$T = e^{-\Gamma\alpha L} \tag{5.3}$$

in which Γ is the confinement factor of the light in the active area, a the imaginary part of the refractive index of un-pumped Q1.58 and L the length of the un-pumped waveguide. Assuming the following rough estimates for these parameters: $\Gamma=0.25$, $a=5\cdot10^5$ and $L=3\cdot10^{-6}$, the transmission of the un-pumped waveguide is just 69%. Since the light has to

pass through this section twice, the total transmission loss is $1-(0.69)^2 = 0.53$. This means that a measured reflectivity of 30% corresponds to an actual reflectivity of 64%.

The above calculation is just a quick estimate of the influence of the active waveguide between the contacted amplifier section and the DBR mirror. In reality some of the current will spread into the un-pumped waveguide through the highly doped contact and cladding layers. This would however reduce the number of carriers in the amplifier waveguide next to the un-pumped section, leading to an increased loss in this part. Also, the length of the un-pumped section can vary between the different devices, since the e-beam patterns were written in different layers for different number of DBR periods. And since in the fabrication process no local alignment features were used between the consecutive layers, the final position of the DBR mirror can vary by 1 or 2 μm.

5.5.6 Conclusion

In this section a new characterization method to quantify the reflectivity of DBR mirrors over a wide wavelength range was demonstrated. It is shown that using short-cavity lasers has the advantage that a spectrum analyzer with even a moderate resolution can be used. Because the measurements are conducted at the transparency current density, which can be accurately determined, a fitted gain model is not required. However, obtaining correct numbers for the propagation loss as a function of wavelength at the transparency current density is essential.

The values found for the reflectivity of 1-5 period deeply etched DBR mirrors filled with BCB are lower than expected from theoretical simulations. The difference is attributed to the fact that the waveguide that connects the DBR mirrors to the amplifier waveguides is made from all-active material, which has a very high absorption. Even a short waveguide can therefore effectively reduce the extracted DBR reflectivity by approximately 50%. Fabricating the same devices in an active-passive material system could solve this problem and allow a more accurate characterization of the DBR mirrors.

5.6 Characterization of DBR mirrors in active-passive circuits

5.6.1 Introduction

This section describes the characterization of deeply etched DBR mirrors that were processed using the full active-passive shallow-deep process flow as described in section 4.6. All the mirrors were filled with BCB and all the measurements were performed using TE polarized light. First the 1-period DBR mirrors in passive waveguides were characterized using a similar method as described in section 5.2. In these devices the cavity length was reduced to 100 μm in order to reduce the uncertainty caused by the variation in waveguide propagation losses.

Next 110 µm long short-cavity lasers were characterized using a sub-threshold method as described in section 5.5. The reflectivity results from the passive waveguide characterization were used as a reference to obtain accurate values for the material gain at a fixed drive current. Therefore a longer reference laser device was not necessary.

5.6.2 Single-period DBR mirrors in passive waveguides

The measured structures are shown in figure 5.35. It consists of 4.5 mm long passive waveguides that have a 7° angle with respect to the cleaved chip facets to prevent reflections from the facets. In the middle of the waveguides 100 µm long cavities were created using single-period DBR mirrors with length L_{gap}. The length of the etched gap was varied between 470 nm and 1030 nm. There are 15 waveguides in total. Inside the cavities the waveguides are deeply etched, with measured propagation losses of about 5 dB/cm.
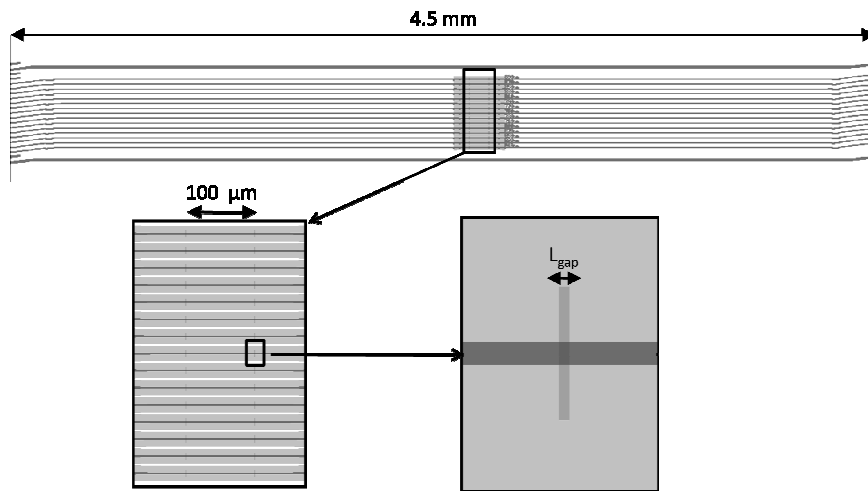
Figure 5.35: Measured structures for passive DBR cavities.

Broadband light from an EDFA source is coupled into the waveguides from one end and the transmission spectra are recorded on the other end using an Optical Spectrum Analyzer (OSA). The 100 µm cavities cause an FP-fringe pattern from which the mirror reflectivity can be extracted as described in sub-section 5.2.2. An example of a (normalized) fringe pattern and the resulting reflectivity spectrum are shown in figure 5.36. The spectra were normalized using a reference EDFA spectrum recorded from a waveguide without DBR cavity. Because the EDFA power in the 1500-1520 nm and the 1580-1600 nm ranges is very low the resulting spectrum is a little noisy in these areas. These ranges are therefore not taken into account in the reflectivity determination.

The results obtained with this method are more accurate than the results obtained in section 5.2.3 because the cavities are much shorter. Therefore the reflectivity determination is not influenced by variations in the propagation loss.
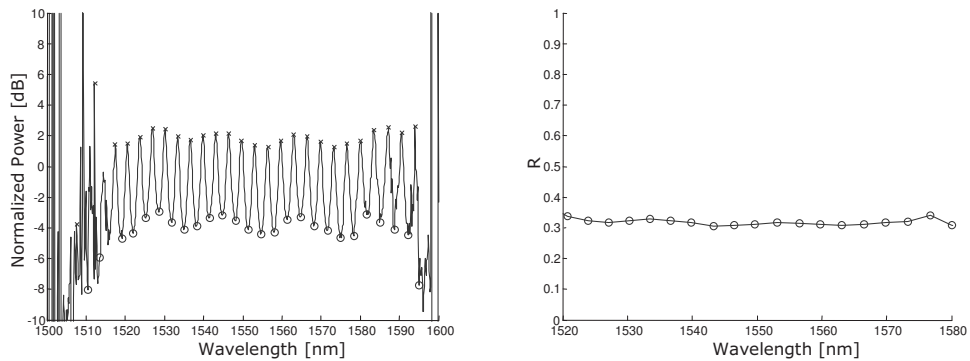
Figure 5.36: Normalized transmission fringe pattern (left) with maxima (x) and minima (o) indicated in the graph. The calculated DBR reflectivity is shown in the right plot. The designed gap length was 870 nm.

The plot in figure 5.37 shows the obtained reflectivity as a function of the designed DBR gap length. The minimum reflectivity found at L_{gap}=650 nm was expected to occur around L_{gap}=550 nm (see figure 2.19). However, the actual realized gap length might differ from the designed value due to variations in e-beam exposure dose. To check this, some SEM images were made from similar structures and the length of the gap was measured. The obtained values are plotted in figure 5.38. The graph shows that in this particular sample the realized DBR gap length is approximately 100 nm shorter than the designed value.
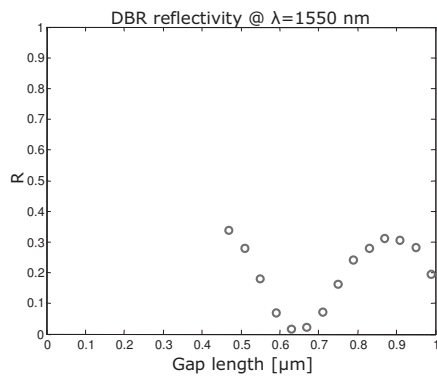
Figure 5.37: Single period DBR reflectivity at λ=1.55 μm as a function of designed gap length.

105
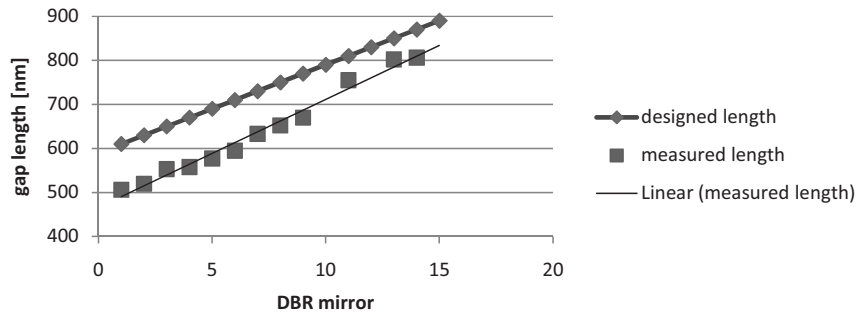
Figure 5.38: SEM measurements of DBR gap length.

Using this information the results from Figure 5.37 were adjusted to the correct gap length and plotted together with the results from the FDTD simulations from Figure 2.19. The results are shown in figure 5.39. The shapes of the graphs match very well, but the absolute value of the measured reflectivities is lower than the simulated value. This is attributed to small fabrication imperfections such as rounding of the waveguide corners at the DBR mirror and sidewall roughness. These imperfections reduce the reflectivity at maximum resonance (300 nm and 800 nm gap length), but it should also increase the minimum reflectivity around L_{gap}=550 nm. In contrast, however, the minimum reflectivity reduces to almost 0. A possible explanation for this behavior is found by looking at the SEM images that were used to determine the actual realized gap length. In figure 5.40, such a SEM image is shown together with a schematic picture of the shape of the etched gap and the refracted light paths. The etched facets of the DBR gap are slightly curved due to the fabrication process. The curved facets can cause diffraction of the light reflecting from the first DBR facet, as shown in the schematic presentation on the right of figure 5.40. However, the light reflected from the second facet is concentrated when it is reflected back from the second curved facet. Therefore it is possible that the reflected light from the second facet is equally strong as the light reflected from the first facet, and thus, in the case of destructive interference, it can cause the total reflectivity to reduce to almost 0.
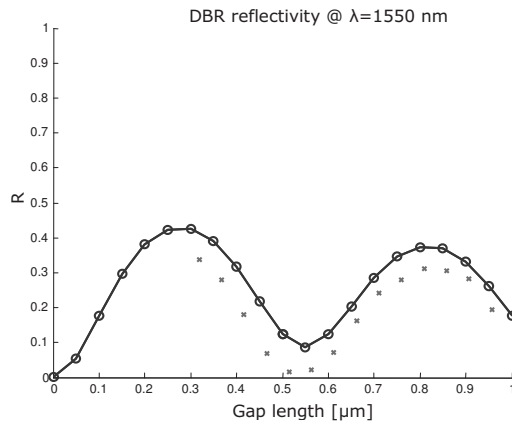
Figure 5.39: Measured DBR reflectivity (x) as a function of the realized gap length plotted together with the simulated values from Figure 2.19 (o).
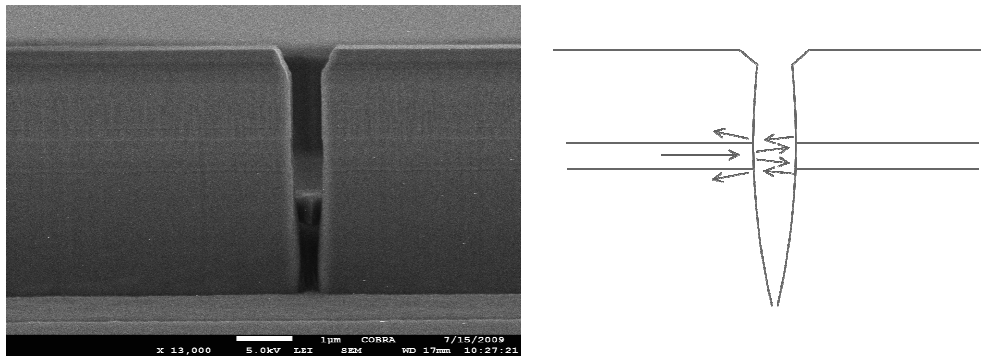
Figure 5.40: SEM image of realized single-gap DBR mirror (left image) and schematic picture of light refracted from the curved facets (right image).

5.6.3 Active-passive DBR lasers

In order to characterize DBR mirrors with a larger number of periods, a sub-threshold method as described in section 5.5 was used. Since the chips that were used in this section were cleaved at a length of 4.5 mm, devices that use the cleaved facets as the laser mirrors have a very small mode-spacing. Accurate measurement of the sub-threshold spectrum in order to obtain the propagation losses as described in sub-section 5.5.3 is therefore not possible, since the resolution of the OSA is not high enough.

However, using the results obtained from the single-period DBR mirrors described in the previous sub-section, it is possible to extract information on the material gain at a certain

107

current density and use this as a reference instead of the propagation loss. The measurement therefore consists of 3 steps:

1) Measure the sub-threshold spectrum of single-period DBR laser
2) Calculate the material gain at this current density
3) Measure and calculate the DBR reflectivities of 2-5 period DBR lasers

For these measurements a set of 110 µm long DBR lasers were used that contained a 100 µm long shallowly etched active section. The DBR mirrors were etched in the passive waveguides. The structure is shown in figure 5.41. The lasers were all operated at 5 mA, which is about 50% of the threshold current of the devices with the lowest lasing threshold. The sub-threshold spectra are shown in figure 5.42. The maxima and the minima are also indicated in the plots. The minima in the spectra are very close to, or even below the noise floor of the spectrum analyzer, especially for the devices with a larger number of DBR periods. Some smoothing was applied to the spectra in order to obtain a more realistic value for the minima, but for the devices with 4 and 5 period mirrors the actual minima are probably lower. This will result in an underestimation of the mirror reflectivity in these devices.
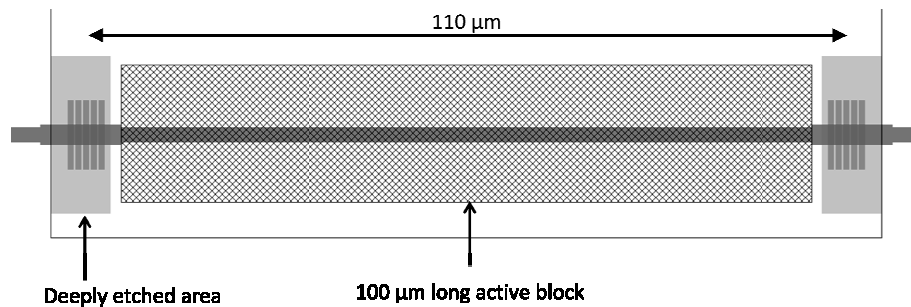
Figure 5.41: Active-passive DBR lasers used for DBR characterization.
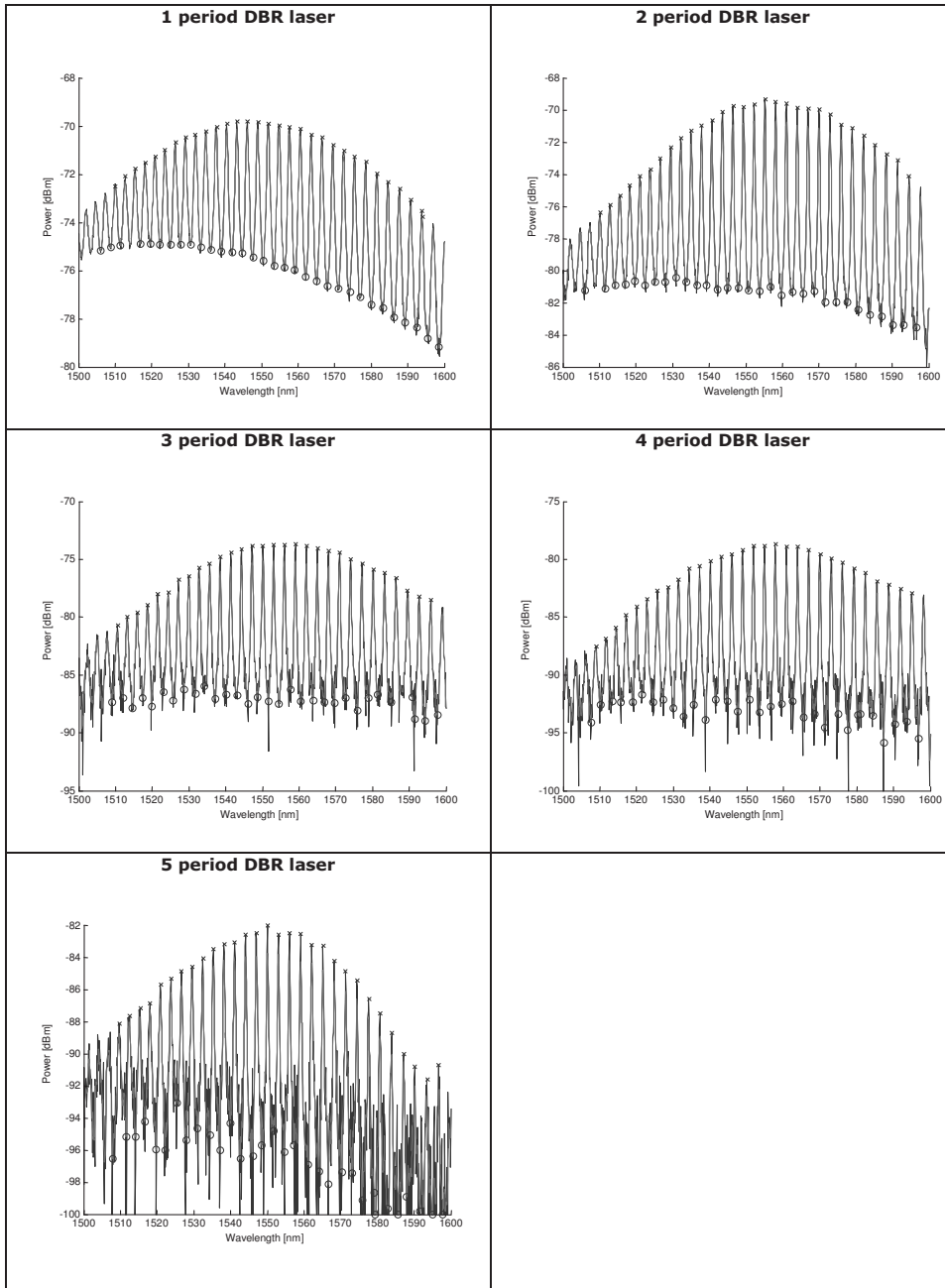
Figure 5.42: Recorded sub-threshold patterns of various DBR lasers. Maxima (x) and minima (o) that were used to calculate the contrast ratio C are also indicated.

Chapter 5

From the spectrum of the 1 period DBR laser, using the reflectivity obtained from the passive cavity measurement, the material gain was calculated. The results are shown in figure 5.43. Using this gain value, the DBR reflectivity was calculated from the sub-threshold spectra of the other devices. The results are shown in figure 5.44. The graph also shows the values used as a reference for the single period DBR mirrors.
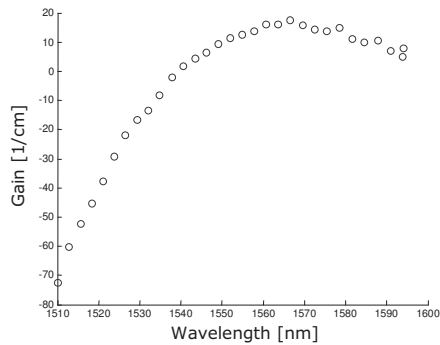
Figure 5.43: Modal gain at 5 mA drive current (100 µm long active area).
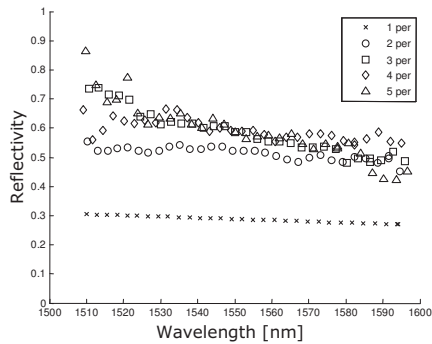
Figure 5.44: DBR reflectivity for various number of DBR periods. Number of periods is indicated in the graph legend.

From the plots we can see that the DBR reflectivity increases as the number of DBR periods increase. However, since for the devices with 3-5 period mirrors the minima in the recorded spectra are close to, or below the noise floor of the spectrum analyzer, the resulting DBR reflectivity value is limited by the equipment sensitivity. This is due to the high transmission loss of the DBR mirrors with more than 3 periods. The effect is larger at the lower and upper parts of the spectra, because the spontaneous emission power is very low at these wavelengths. In figure 5.45 the measured reflectivity at the wavelength of λ=1550 nm is shown together with the simulated values obtained by 3D FDTD simulation. The measured

values follow the simulated reflectivity quite well, but saturate around 60% due to the noise limitation.
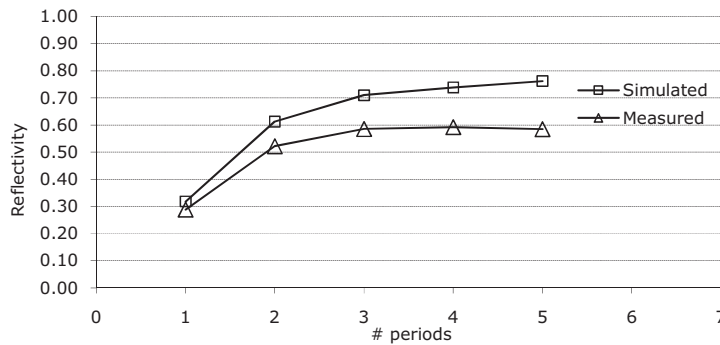
Figure 5.45: Simulated and measured DBR reflectivity at λ=1550 nm.

5.6.4 Conclusion

In this section a method to characterize DBR mirrors in active-passive integrated circuits was presented. The method combines the technique used in section 5.2 (characterization of DBR mirrors in passive waveguides) with the sub-threshold technique described in section 5.5. The advantage of this combination is that a long reference laser with cleaved mirrors is not required and that the final characterization can be performed at any injection current as long as it is below lasing threshold. A complicated interpolation to obtain the reflectivity exactly at the transparency current density as described in sub-section 5.5.4 is therefore not required. The only disadvantage is that the characterization required a relatively complex chip which contains active-passive material.

The results obtained with this method show reasonably good agreement with the simulation results for DBR mirrors with 1-3 periods. For the characterization of very high reflective mirrors (4 periods and more), the low transmission signal limits the accuracy of the method. This problem could be circumvented by using a different laser structure with a high reflective mirror on one side and a low reflective mirror (single period) on the other.

5.7 Discussion

In this chapter various characterization methods to analyze the DBR performance were presented. A number of chips were fabricated in order to obtain accurate results over a wide wavelength range. The fabrication process increased in complexity, but it does not deviate from the process steps described in chapter 4 that are required to realize the most common integrated circuit functionality.

The methods based on determining the threshold current density are simple, but an accurate gain model is needed and that the reflectivity that can be extracted is only valid for the lasing wavelength.

The Fabry-Perot resonance measurements have the advantage that the reflectivity can be determined over a wide wavelength range. Using laser devices to characterize the DBR mirrors has the additional advantage that the characterization light is generated on-chip, making an accurate (tunable-) light source not necessary and polarization control easier.

The quality of the measurement results depends a lot on the method used and the type of characterization structure that was used. The results from the first characterization experiments on 1st order BCB filled DBR gratings in passive waveguides show reasonably high reflectivities, although the spread in measurement points is very large and the wavelength dependence was not studied due to the limited tunability of the available light source. In the all-active devices the DBR reflectivity is much lower than what we expected from simulations. Also the expected trend of higher reflectivity as the number of periods increase was not observed. We believe that the main reason for the difference lies in the fact that all-active, highly absorbing material was used in the waveguide connecting the DBR mirror with the amplifier section. This problem is indeed avoided by using DBR lasers in active-passive material. These devices show higher reflectivities, up to 60%, which confirms the hypothesis that the absorption of the all-active material is causing the lower reflectivity in the all-active devices. For the accurate characterization of DBR mirrors with 4 or more periods it would be better to choose a structure with only one high reflective mirror, rather than two. The light can then be collected through a low reflective mirror which would improve the signal power.

With the current methods, the loss of the signal transmitted through the DBR cannot be determined. This has not been investigated in this thesis, since transmission loss and waveguide propagation loss are difficult to determine separately. However, this is an interesting performance parameter to study, because it gives information about the loss in the DBR mirror. Further investigation towards suitable methods for determining the transmission properties is therefore required.

References

1 S. Rennon, K. Avary, F. Klopf, J. P. Reithmaier and A. Forchel, "Edge-Emitting Microlasers With One Active Layer of Quantum Dots", IEEE J. Sel. Top. Quantum Electronics, Vol. 7, No. 2, Mar. 2001

2 M. M. Raj, J. Wiedmann, Y. Saka, K. Ebihara, S. Arai, "Highly Uniform 1.5 μm Wavelength Deeply Etched Semiconductor/Benzocyclobutene Distributed Bragg Reflector Lasers", Jpn. J. Appl. Phys, Vol. 29, No 12B, Dec. 2000

3 L. Raffaele, R. M. de la Rue, J. S. Roberts, T. M. Krauss, "Edge-Emitting Semiconductor Microlasers with Ultrashort-Cavity and Dry-Etched High-Reflectivity Photonic Microstructure Mirrors", IEEE Photonics Technology Letters, Vol. 13, No. 3, Mar. 2001

4 B.W.Hakki and T.Paoli, "Gain spectra in GaAs double heterostructure injection lasers", Journal of Applied Physics, vol.46, no. 3, pp. 1299-1305, 1975

5 R.G. Walker, "Simple and accurate loss measurement technique for semiconductor optical waveguides," Electron. Lett., vol. 21, no. 13, pp. 581-583, June 1985

6 Y. Barbarin, E.A.J.M Bente, L. Mussard, G. Servanton, Y.S. Oei, R. Nötzel, and M.K. Smit, "Gain measurements of Fabry-Perot InP/InGaAsP lasers using an ultra high resolution spectrometer", *Appl. Opt.*, vol. 45, no. 35, pp. 9007-9012, 2006

7 P.A. Besse, J.S. Gu, H. Melchior, "Reflectivity minimization of semiconductor laser amplifiers with coated and angled facets considering two-dimensional beam profiles," IEEE Journal of Quantum Electronics, vol.27, no.6, pp.1830-1836, Jun 1991

8 L. A. Clodren and S. W. Corzine, "Diode Lasers and Photonic Integrated Circuits", John Wiley & Sons, 1995, section 2.5 & 2.6
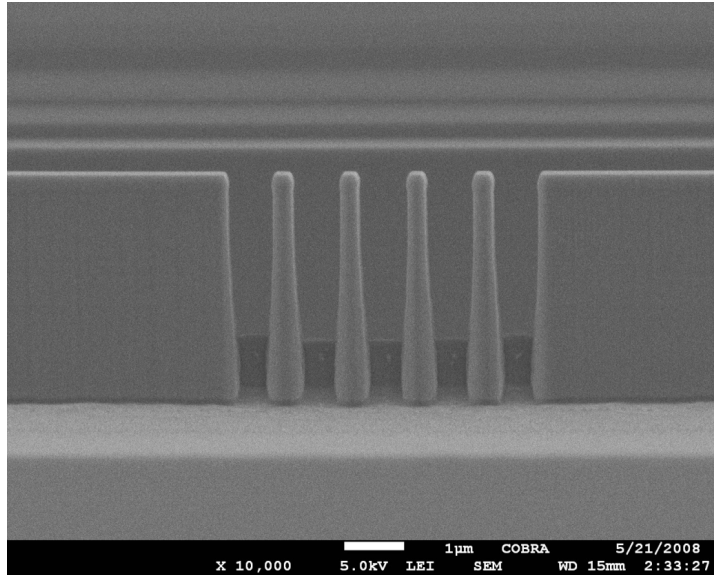
"A good day"

Deeply-etched DBR grating

6 Integrated Filtered-Feedback Tunable Laser with Deeply-Etched DBR Mirrors and AWG filter

In the previous chapters many aspects of deep-etched Distributed Bragg Reflector (DBR) mirrors were introduced. The various design and simulation tools that are available were reviewed, the newly developed fabrication process was described and various characterization methods were explained. In this chapter an example of an application of the deep-etched DBR mirrors in a complex Photonic Integrated Circuit (PIC) is demonstrated. This application shows that the introduction of DBR mirrors as a building block in a generic PIC design platform can offer many new possibilities.

In this chapter a novel discretely tunable laser for telecommunication purposes is described. It consists of a Fabry-Perot laser with deeply etched DBR mirrors in combination with a feedback circuit that forces the laser to operate at a single wavelength. The first results of this new Integrated Filtered-Feedback Tunable Laser (IFF-TL) device are very promising, although a full dynamical characterization was not done yet.

6.1 Introduction

Tunable lasers are widely used in telecommunication networks nowadays because they allow flexible reconfiguration of the network within micro-seconds. Additionally they provide a replacement for fixed-wavelength lasers. Although the wavelength tunability comes with a price, the inventory costs are reduced since only a few replacement lasers need to be kept in stock, rather than at least one laser for each wavelength used in the network [1,2].

The extra cost of a tunable laser compared to a fixed wavelength laser is usually caused by the complex control electronics that are required to stabilize the laser output signal. A tunable Distributed Bragg Reflector (DBR) laser based on tunable DBR mirrors for example has at least 4 analog control parameters: the main laser bias current, the tuning currents to the front and rear mirrors and a tuning current to a phase section to prevent unwanted mode-hops [3].

All these control currents affect the thermal stability inside the laser which also has influence on the wavelength of the output signal. Since these temperature effects occur on a much longer timescale than the initial switching mechanisms, constant re-adjustment of the laser controls is necessary. These complex control schemes make the total system more expensive [3].

The principle of the IFF-TL was first described in [4] and then experimentally demonstrated by Matsuo et al. in [5]. In this work two coupled micro-ring filters were used for controlling the wavelength. It was shown that with this approach the frequency drift due to temperature changes can be reduced to less than 1 GHz. In another publication by Fürst et al. [6] a ring resonator laser was forced to operate in a single laser mode by using filtered

feedback from a tunable narrow-band DBR grating. In their paper the authors report a switching speed of 450 ps. However, in both these devices the filter component was controlled by one or two analog input signals, making the operation of the devices still complicated and sensitive to temperature fluctuations.

In this chapter we present a laser which uses a compact Arrayed Waveguide Grating (AWG) integrated with short Semiconductor Optical Amplifier (SOA) gate switches for controlling the wavelength. In an earlier paper [7] it has been shown that these short gate switches allow for switching times of a few ns. In this chapter we demonstrate that the filtered feedback principle in combination with an AWG and an SOA gate switch array allows for simple and stable tuning. To the best of our knowledge the device presented in this chapter is the first device that operates in a quasi-digital manner, making it a very promising device for large scale application in fiber networks.

6.2 Operating principle

A schematic picture of the novel Integrated Filtered-Feedback Tunable Laser (IFF-TL) is shown in figure 6.1. A Fabry-Perot (FP) laser is formed by a SOA and two deeply etched Distributed Bragg Reflector (DBR) mirrors. The laser cavity length is chosen such that the mode spacing equals the channel spacing in the standard ITU-grid used for telecom applications [8], e.g. 50 or 100 GHz.

The FP laser is coupled to an AWG filter [9] that splits the light of the FP laser in several waveguide branches. Each branch contains an SOA that works as an optical gate. When put in reverse bias the SOA will absorb the light, but when put in forward bias the light will be transmitted or even amplified. The light is then reflected either by a cleaved chip facet, another DBR mirror or any other form of broadband mirror, and fed back through the AWG into the FP laser. The feedback light causes the laser mode with the largest feedback strength to dominate over the other modes and single mode operation is achieved. The feedback strength is controlled by the gates in the feedback branches. The output light leaves the chip through the opposite DBR mirror.
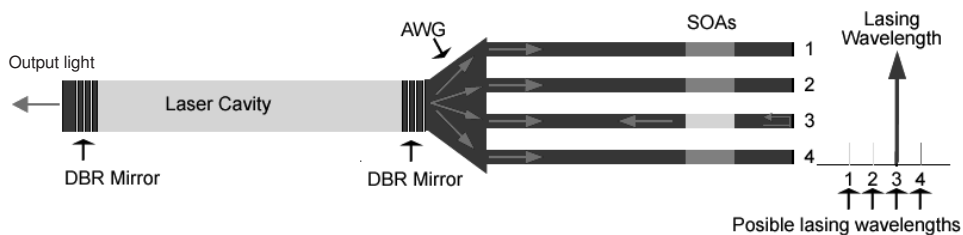
Figure 6.1: Schematic picture of the IFF-TL device.

The concept of filtered-feedback has many advantages over other tunable laser concepts. Compared to DBR lasers containing tunable DBR mirrors [10,11,12] the main difference is

116

that the tuning mechanism is placed outside the main laser cavity. This means that there is no change in refractive index in the main FP laser cavity while switching the wavelength. Therefore the wavelength stability is improved and control schemes are much simpler. The limitation is that the device can only operate at a fixed set of wavelengths and cannot be tuned continuously.

The effect of temperature changes due to changing tuning currents is very small. Any change of temperature usually results in a wavelength drift. Since this wavelength drift occurs on a much longer time scale than the wavelength switching, it complicates the laser control. A good comparison of these temperature effects in a conventional (ring-resonator-based) tunable laser and a filtered-feedback tunable laser is given in [5].

Compared to conventional AWG lasers [7,13] the main advantage is that in the IFF-TL device the AWG is placed outside the main laser cavity. This means that the losses caused by the AWG do not have to be compensated by the gain section to reach lasing threshold. Any non-uniformity in the transmission of the AWG channels only translates into a lower feedback signal for some wavelengths. This can potentially slow down the switching speeds for these channels, but the threshold current is not changed. Therefore the carrier density in the laser cavity will be the same which results in a very stable wavelength.

The device can switch between any two wavelengths without addressing unwanted wavelengths. This prevents the so-called 'dark-tuning', which requires blanking of the laser output while switching the wavelength.

6.3 Device design
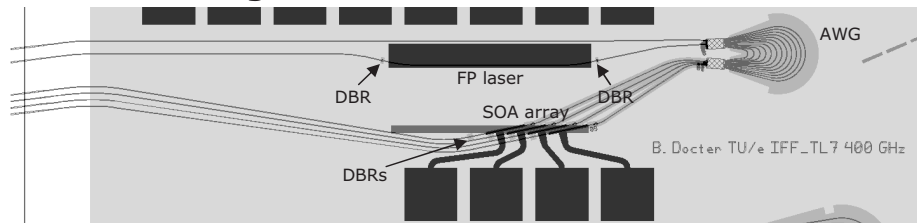
Figure 6.2: Mask design of the realized IFF-TL device.

6.3.1 FP-laser

The layout that was used for the IFF-TL devices is shown in figure 6.2. The main element of the IFF-TL is an 822 µm long FP laser with 2-period deeply etched DBR mirrors. This part of the device is shown in figure 6.3. The waveguides cross the active-passive interface under an angle to reduce any possible reflections from the butt-joint. The 2-period DBR mirrors are deeply etched, while the rest of the structure consists of shallow etched waveguides.

The DBR mirrors allow us to control the laser cavity length very accurately. This is important since the mode-spacing $\Delta\lambda$ is given by the following formula:

$$\Delta\lambda = \frac{\lambda^2}{2N_g L_{cav}}$$

(6.1)

where N_g is the group index of the waveguide ($N_g \approx 3.65$) and λ is the central wavelength (1.55 μm). The cavity length L_{cav} of 822 μm therefore corresponds to a mode spacing of 0.4 nm or 50 GHz. Note that the group index N_g depends on the carrier density in the laser. It is therefore influenced by the DBR reflectivity. However, the longer the laser cavity, the lower the dependence of carrier density on DBR reflectivity as was shown in sub-section 5.3.2 (figure 5.14). The exact position of the FP laser modes can be tuned by changing the operating temperature of the laser.
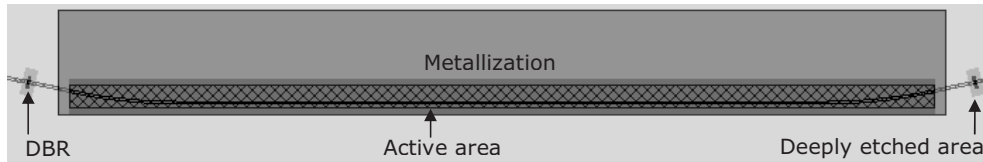
Figure 6.3: Detail of the chip layout showing the FP laser with deeply etched DBR mirrors.

6.3.2 AWG filter

The AWG filter was designed using a deep-shallow double etching technique as described in [14]. The layout of the AWG device is shown in figure 6.4. The 4-channel AWG connected to the FP laser has a channel spacing of 3.2 nm or 400 GHz.
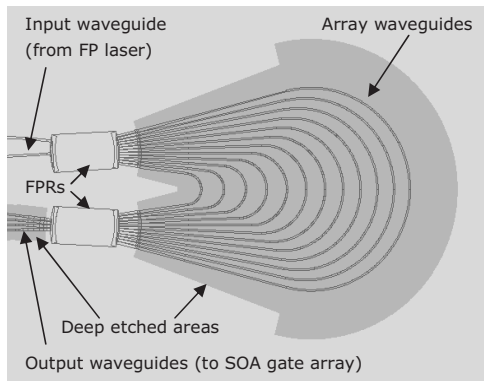
Figure 6.4: Detail of the chip layout showing the AWG filter. The deep and shallow etched areas are indicated in the figure. (FPR = Free Propagation Region).
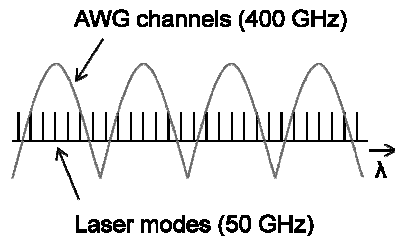
Figure 6.5: Possible FP-laser modes and AWG filter response.

The channel spacing of the AWG filter has been chosen a multiple of the channel spacing of the FP laser. As long as the channel spacing of the AWG is an integer number times the channel spacing of the FP laser, the device will still operate. This is schematically shown in figure 6.5. Choosing the FP mode spacing a fraction of the AWG channel spacing guarantees that at least 1 FP mode falls within the passband of each AWG channel. The disadvantage of this approach is that when multiple FP modes are passed through one AWG channel, the phase of the light being fed back to the laser plays a more important role in the final lasing mode selection. The result is that 50 GHz mode hops can occur. However, adjusting the bias current on the SOA gates can influence the phase of the feedback light, and thereby the right mode can be selected.

Note that the AWG filter must discriminate between two wavelength channels, but the difference in transmission properties does not have to be very large. For comparison: the difference in mirror loss that is used in conventional DBR lasers to operate with more than 40 dB Side Mode Suppression Ratio (SMSR) is only 1-2 dB [15]. In the case of a filtered feedback device we expect that a similar difference in feedback strength is sufficient to switch the laser. The requirements in terms of extinction loss and cross-talk levels are therefore much more relaxed than the specifications required for instance for a WDM receiver filter. The AWG design can therefore be quite small (e.g. <500x500 µm for a 4-channel 400 GHz design).

6.3.3 SOA gate array
In the feedback branches an array of 100 µm long SOA gates has been incorporated. This gate array is connected to a series of metal contact pads which can be accessed using a standard electrical multi-probe. Directly after the gates there are 3-period DBR mirrors that reflect about 85% of the light back through the gates and the AWG to provide the filtered feedback signal. These DBR mirrors also let a small portion of the light pass that can be used for characterization purposes.

119
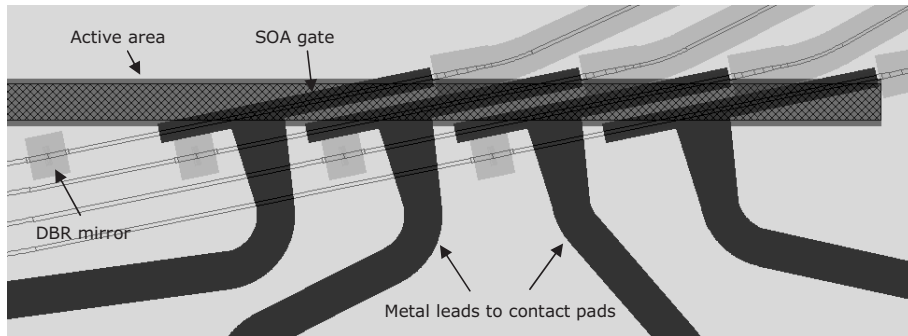
Figure 6.6: Detail of the chip layout showing the SOA gate array.

The feedback light passes through the SOA gates twice. This means that in order to absorb the light in un-biased gates, the SOAs can be very short. Probably lengths of 10-20 μm are also possible, although care has to be taken that the laser does not saturate the SOAs. To prevent this a reverse bias can be applied. In this first design, however, it was chosen to keep the SOA length a little longer to be able to compensate for losses in the AWG and the DBR mirrors.

Apart from changing the amplitude of the feedback light, the SOA gates can also be used to manipulate the phase of the feedback light, since the refractive index of the SOAs is quite dependent on the carrier density. In order to benefit most from this phase effect, the SOAs were made 100 μm long, which is longer than strictly required to obtain sufficient extinction ratio. However, once the feedback requirements (amplitude and phase) are better understood, it is expected that the SOA gate lengths can be reduced significantly, enhancing the electrical bandwidth of the gates.

6.3.4 DBR mirrors
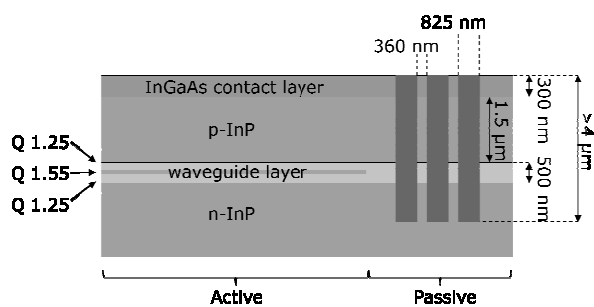
Figure 6.7: Schematic side-view picture of deeply-etched DBR mirror.

The deeply etched DBR mirrors that are used to form the FP laser are schematically shown in figure 6.7. These DBR mirrors provide high reflectivity over the full gain spectrum [16]. The gaps between the mirrors should be etched at least 1.5 µm through the waveguide layer in order to obtain maximum reflectivity (see section 2.3.2, figure 2.14). After etching the mirrors, they are filled with BCB (refractive index n_{BCB}=1.54). This reduces the diffraction losses, but decreases the critical feature size of the DBRs as well. We use a 3rd order DBR design, where the length of each section equals ¾λ/N (N is the effective index of the mode in each material). This means that the gaps that are etched in the waveguides are 825 nm wide and the semiconductor left in between the gaps is 360 nm wide (see also section 2.4).
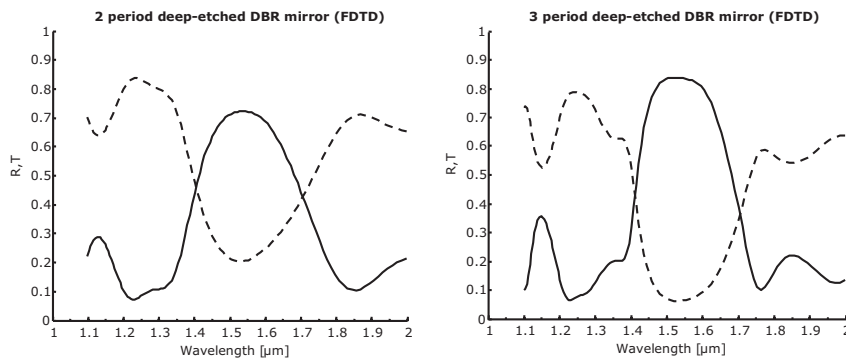
Figure 6.8: 3D FDTD simulation of the reflection (solid lines) and transmission (dashed lines) of a 2 period deeply-etched DBR mirror (left) and a 3 period deeply-etched DBR mirror (right).

In the IFF-TL device described in this chapter we used 2-period DBR mirrors to form the FP laser cavity and 3-period DBR mirrors in the feedback branches to reflect the light back to the FP-laser. The calculated reflection and transmission spectra of such mirrors are shown in figure 6.8. The 2-period mirror provides about 70% reflectivity, but still allows approximately 20% (= -7.0 dB) of the light through the mirror into the feedback section. Of course the light that comes back from the feedback section has to pass this mirror once more before it enters the laser again. The 3-period mirror at the end of the feedback branch reflects about 85% (= 0.7 dB loss).

Assuming that the AWG insertion loss is about 5 dB for a single pass, the combination of these mirrors and AWG would result in a feedback strength of approximately -24.7 dB. This is the feedback value when the SOA gates are opened. When the SOAs are not biased, the feedback will be much lower, but the extra absorption loss is very dependent on the total optical power due to saturation effects in the SOAs.

6.4 Filtered-feedback model

The operation principle was tested by modeling the device as a 2-mode laser in which we can selectively apply feedback to one of the modes[1]. The effect of the feedback was modeled using a system of rate equations extended with a delayed term which accounts for the feedback as described by Lang and Kobayashi [17]. The filtering of the feedback light was applied according to Yousefi and Lenstra [18].
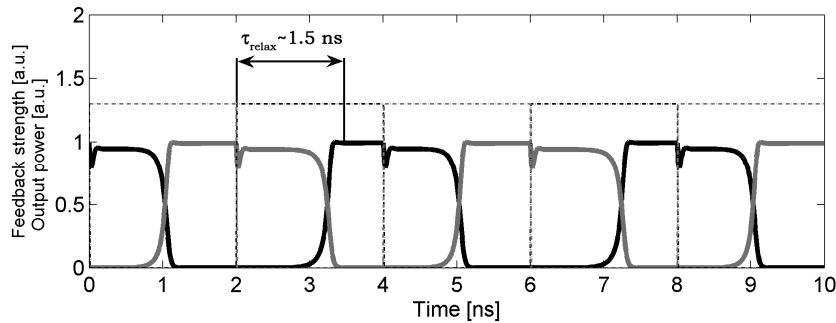
Figure 6.9: Simulated switching behavior of a 2-channel device without SE noise

The result of such simulations is shown in figure 6.9. The two lines represent the output power in two different wavelengths when the device is switching periodically between two gates. When gate 1 is biased in order to provide feedback, the corresponding mode will stably lase. If the feedback is moved to another channel, for example by forward biasing the SOA in gate 2, the operation of the system settles to the second mode. The time needed for the second mode to build up and suppress the first mode is approximately 1.5 ns. The switching of the bias currents is assumed to occur simultaneously.

The small dip in output power at the time the feedback signal is switched can be explained in the following way: When the gates are switched to a different channel, the feedback signal drops to a very low level. This results in a small decrease in the effective mirror reflectivity. Since the carrier density in the laser cavity is clamped at the threshold value (before the feedback was removed), the laser now briefly drops below the threshold, hence

---

[1] For the modeling of the IFF-TL devices the author works in close collaboration with researchers from the Department of Applied Physics and Photonics of the Vrije Universiteit Brussel. Because the model that is discussed in this chapter was not made by the author, the details are not discussed here and only the relevant results are reported. Since at the time of writing the model was not published yet, no reference could be given. The model was developed by S. Beri, I.V. Ermakov and J. Danckaert.

the dip in output power. However, the extra carriers required to compensate the loss of feedback are quickly provided and the system settles in a new equilibrium until the power of the new mode builds up enough to switch the wavelength.
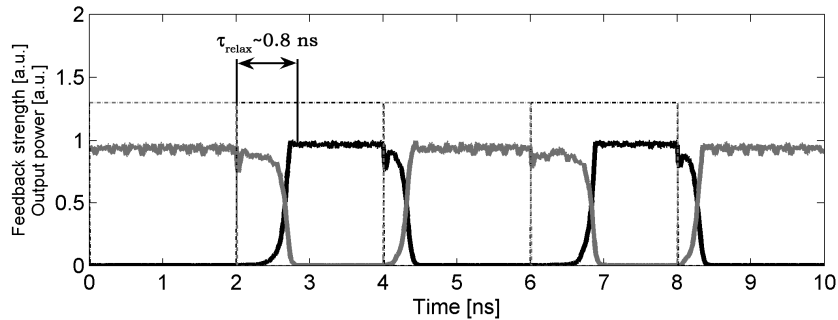
Figure 6.10: Simulated switching behavior of a 2-channel device including SE noise.

In the previous results the model did not include any Spontaneous Emission (SE) noise. However, the SE noise plays an important role in the switching dynamics, because it enhances the build-up of power in the new mode. This effect can be observed in figure 6.10, where SE noise was added to the model. With SE noise the switching-time between the two modes becomes 0.8 ns. This result matches quite well with measured switching speeds in the ring resonator based filtered feedback devices presented in [5] and [6] and the AWG laser using gate switches described in [7].

6.5 Fabrication

6.5.1 Active-passive integration material

The IFF-TL device was fabricated using an active-passive integration scheme developed in co-operation with JDS Uniphase [19,20]. All layers are grown by Metal-Organic Vapor Phase Epitaxy (MOVPE). First the active layer stack is grown on the n-doped substrate. The active layer is formed by a 120 nm thick Q1.55 layer embedded in two 190 nm thick Q1.25 confinement layers. The active blocks are then covered by a lithography-defined SiO$_2$ layer and removed wet-chemically. Then the passive Q1.25 waveguide layer is selectively grown (500 nm thick) in the 2nd growth step. After removal of the SiO$_2$ mask layer the 3rd and final growth step adds the common cladding and contact layers. The final layer stack for both the active and passive parts is shown in Table 6.1.

	Active			Passive		
#	material	thickness		doping		
14*	p-Qtop	570		1.5×10^{19}		
13	p-InP	1000		1×10^{18}		
12	p-InP	300		5×10^{17}		
11	p-Q1.25	20		3×10^{17}		
#	material	thickness	doping	#	material	thickness	doping
8	p-InP	200	3×10^{17}	10	InP	200	n.i.d.
7	p-Q1.25	50	1×10^{17}				
6	Q1.25	140	n.i.d.	9	n-Q1.25	360	6×10^{16}
5	Q1.55	120	n.i.d.				
4	n-Q1.25	50	6×10^{16}				
#	material	thickness		doping		
3	n-Q1.25	140		6×10^{16}		
2	n-InP	500		5×10^{17}		
1	n-InP	500		1×10^{18}		
0	n-InP	substrate		$1\text{-}4 \times 10^{18}$		

Table 6.1: Active-passive layer stack. The thick lines show the different growth steps: First the active layer stack is grown on the substrate (layers 1 - 8). In the 2nd growth step the passive waveguide layers are grown (layers 9 & 10). In the 3rd growth step the common cladding layers and contact layer are grown (layers 11 - 14). All thicknesses are measured in nm. N.i.d. stands for not intentionally doped.

*: the contact layer consists of graded material stack with increasing bandgap wavelength and doping profile. The exact layer composition is confidential.

6.5.2 Combined electron beam and optical lithography

After the growth of the materials the masking layers for the waveguide definition are applied. First we deposit a 430 nm thick SiO_2 layer by PECVD and then a 50 nm Cr layer is evaporated. The Cr layer allows us to combine the e-beam lithography (EBL) pattern required for the DBR mirrors with the optical lithography pattern required for the waveguides. The combined lithography process is shown in figure 6.11. A 320 nm thick ZEP e-beam resist is applied and the DBR patterns are written using a Raith 150 e-beam system using 30 kV acceleration voltage. The DBR pattern consists of the DBR gaps and is defined 10 μm wide, which is much wider than the 2 μm wide waveguides. This allows very tolerant alignment of the waveguide pattern but also reduces the impact of proximity effects in the e-beam lithography which are most prominent at the corners of the DBRs.

The DBR pattern is transferred into the Cr layer by $Cl_2{:}O_2$ ICP etching. Then the waveguide pattern is aligned by optical lithography on the DBR structures. This pattern is also transferred to the Cr layer which then serves as an etching mask to open the 430 nm thick SiO_2 layer in a CHF_3 RIE process.
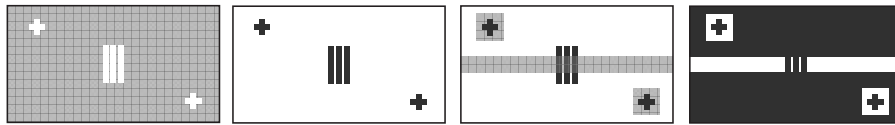
a) DBR pattern in ZEP on Cr   b) DBR pattern in Cr on SiO$_x$ c) Waveguide lithography   d) Final Cr mask

Figure 6.11: Lithography process. First, the DBRs are written by e-beam lithography (a), then the DBR pattern is etched into the chromium mask (b), then the waveguides are defined by optical lithography (c), and are also etched into the chromium mask (d).

6.5.3 Double etching process

The device was fabricated using a double-etching technique. This enables the realization of shallow-etched and deeply-etched waveguides using the same lithography pattern for the optical channels, avoiding strict alignment requirements. The shallow waveguides are used for low-loss interconnects and SOAs, while the deeply-etched waveguides are suitable for tight bends and DBR reflectors. The deep-etching was done using a Cl$_2$:Ar:H$_2$ Inductively Coupled Plasma (ICP) etching process. This process offers straight and smooth sidewalls which are necessary for the deeply-etched DBR mirrors. A SEM image of a fabricated DBR mirror is shown in figure 6.12. The shallow SOA waveguides were later etched by CH$_4$:H$_2$ ICP etching.
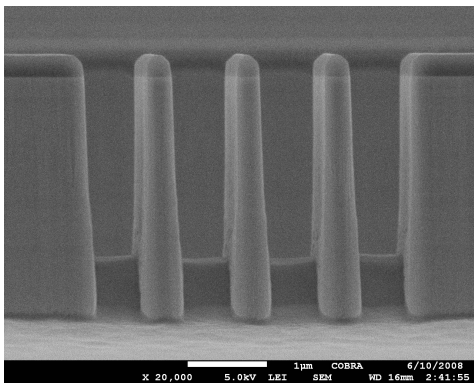
Figure 6.12: Side-view SEM image of a deeply-etched DBR mirror. The SiO$_2$ etching mask is still present.

6.5.4 Planarization and metallization

After the etching a 100 nm SiO$_2$ passivation layer is applied by PECVD and the chip is planarized using a single layer of BCB 3022-46. The planarization properties of the BCB are such that when spun at the right speed, hardly any back-etching is required to open the top of all the waveguides. Ti/Pt/Au p-contacts are added using e-beam evaporation and lift-off. Then an extra 1 µm thick Au layer is electroplated on the large contacts to ensure uniform current injection. Finally the sample is cleaved and fixed on a copper mount.

6.6 Characterization

6.6.1 LI characteristics
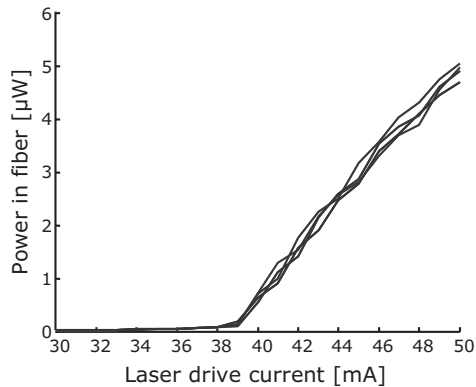
Figure 6.13: LI curves of the IFF-TL device while forward biasing different gates at 10 mA. Note that x-axis scale starts at 30 mA.

Figure 6.13 shows the LI curves for the IFF-TL device operating at 15 °C. The device has an output waveguide with an angle of 7° with respect to the chip facet. This reduces the reflections from the edge of the chip. The light was collected using a lensed fiber and then split into two branches, one to record the output power and one to record the spectrum. The power collected in the fiber is quite low because of high coupling losses between the chip and the lensed fiber.

The different curves in figure 6.13 were recorded while forward biasing each of the gates separately with 10 mA of current. This provides only about 1-2 dB gain, due to the limited length of but the gates. There is also one curve where no gate was opened. From the graphs it is visible that the threshold current is not affected by the feedback light. This indicates that the carrier density in the laser stays constant while switching the channels, which is beneficial for the wavelength stability.

6.6.2 Lasing spectra
Figure 6.14 shows the superimposed lasing spectra of the devices when operated at 45 mA. The text near the different laser peaks indicate which gate was operated. The forward bias on the different gates was between 2 and 13 mA. We can clearly see single mode operation for each of the channels. The SMSR for the various signals is at least 20 dB.

Gate #	Bias current
1	4.0 mA
2	13.0 mA
3	5.0 mA
4	2.0 mA
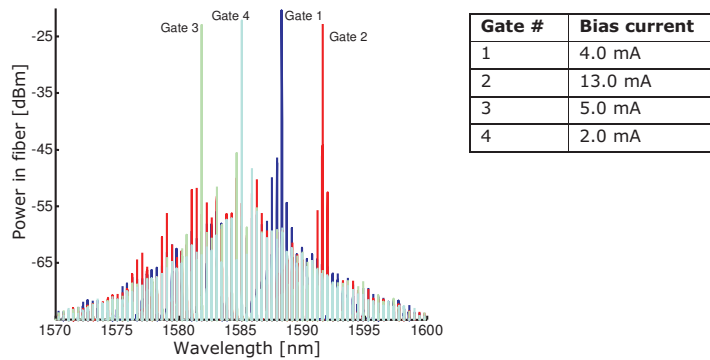
Figure 6.14: Superimposed lasing spectra of the IFF-TL device while forward biasing the different gates. The laser was forward biased at 45 mA, the currents on the different gates are shown in the table

In figure 6.15 a smaller part of the spectrum is plotted. In this figure we observe the sub-threshold side modes that originate from the modes of the FP cavity. The mode spacing is 0.404 nm. This corresponds to a frequency spacing of 50.5 GHz, 1% deviation from the ITU spacing. The distance between the lasing channels is 404 GHz.

The plot demonstrates very nicely the wavelength stability of the device. The FP side modes coincide exactly, no matter which gate is operated. This shows that the group index of the modes in the laser does not change, even though the gates are operated at different currents.
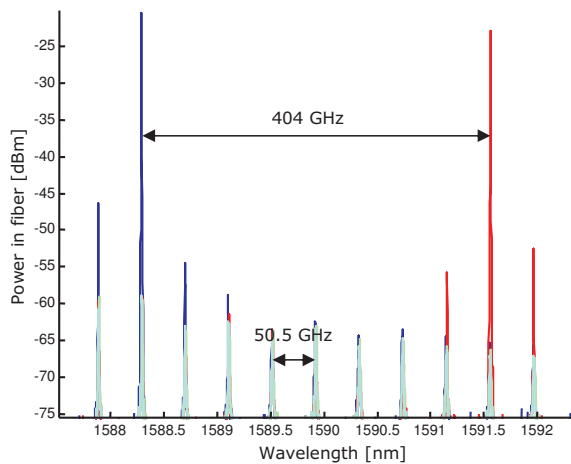
Figure 6.15: Detail of the lasing spectra showing 50.5 GHz FP mode spacing and 404 GHz mode spacing between AWG channels 1 and 2.

6.6.3 Lasing mode selection

In another experiment the peak wavelengths were recorded using a wavelength meter (ANDO AQ6141). This device records the wavelength and power of the peaks in an arbitrary spectrum. Only peaks within -10 dB from the highest peak in the spectrum were recorded.
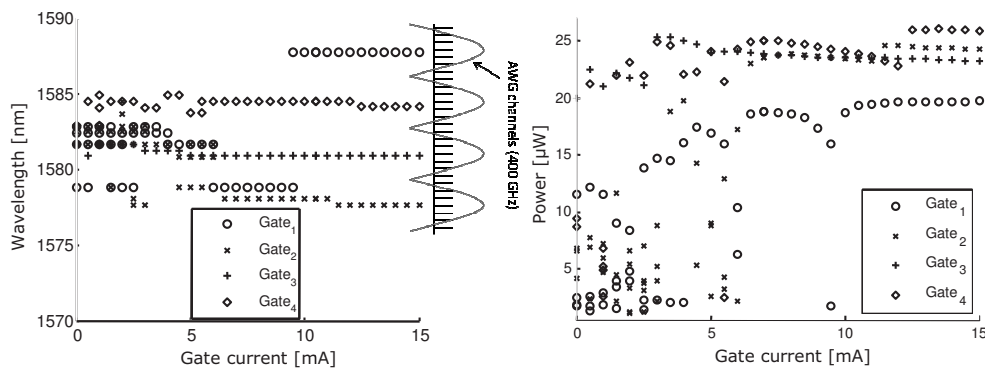
Figure 6.16: Lasing wavelength (left) and output power (right) as a function of gate current. For convenience the AWG filter channels were also indicated in the left figure.

In figure 6.16 the lasing wavelength (left figure) and the output power (right figure) are plotted as a function of the forward bias applied to the different gates. The current applied to the main laser cavity was 41 mA and the temperature was 12 °C. In this experiment also a -10V reverse bias was applied on the gates that were not forward biased to make sure all the light was absorbed.

Some of the lasing peaks do not correspond to the peaks found in figure 6.15. The main difference is the wavelength of gate nr. 2, which is now 1 FSR of the AWG further down the spectrum. This is due to a shift in the gain spectrum caused by the slightly different operating conditions.

The amount of gate-current required to get the laser operating at the wavelength corresponding to the selected feedback branch seems to be higher for gates nr. 1 and 2 than for gates nr. 3 and 4. This can be explained by the fact that a higher feedback power is necessary for wavelengths that are further away from the center of the gain spectrum, which is around 1582 nm.

50 GHz mode-hops (50 GHz = 0.4 nm) are visible which are caused by the large channel bandwidth of the AWG compared to the 50 GHz mode spacing of the FP laser. The wavelength that has the most favorable phase matching will lock the laser. However, the lasing wavelength is usually stable over a large range in gate currents. This shows that the exact phase is not very critical.

Also, once the laser is locked to a single mode operation point, the output power does not fluctuate much with small changes in the gate current. Therefore the device can be operated in a 'quasi-digital' manner, where the exact operation current is not very critical. This could potentially lead to a significant reduction of the cost of the control electronics required to operate this laser.

6.6.4 Feedback phase

From the results on the wavelength selection experiments that were described in the previous sub-section we concluded that the exact phase of the feedback signal is not very critical. Although the modeling of the feedback phase is still under investigation, we will try to give some arguments for this conclusion here.

Because the laser has highly reflective mirrors, the feedback signal is quite low (~-25 dB, but this is a rough estimate, see section 6.3.4). This means that the lasing modes do not drift in order to find a wavelength with better phase matching when the feedback light is not perfectly phase-matched (see figure 6.15). Instead, the laser will operate at the feedback frequency that has the best phase-matching, which explains the 50 GHz mode hops (figure 6.16).

In future designs we plan to either decrease the AWG channel spacing or increase the FP laser mode-spacing so that only 1 FP laser mode exists in each AWG channel. We expect that as long as the selected feedback wavelength has a positive phase and the contribution of the feedback light is higher than any of the residual reflections that are present in the feedback circuit, the laser will lock at the feedback wavelength. However, making sure that the feedback signal has a positive phase might require an additional phase tuning control current.

6.7 Discussion

A novel concept in the field of tunable lasers has been demonstrated. In this section the most important properties of the IFF-TL will be summarized and put into perspective with respect to the many alternatives that are commercially available nowadays.

6.7.1 Output power & SMSR

The output power of the device in the experiments reported in this chapter are relatively low. The device was operated not far above threshold because there were some problems in the electrical contacting of the devices. We were therefore careful in increasing the laser currents. Also the coupling efficiency from the chip to the lensed fiber that was used to collect the light is not very good. However, even when these factors are taken into account, the output power of this device is still much lower than the output power that commercial laser vendors offer nowadays (>10 dBm). A solution can be to integrate an SOA at the laser output to boost the signal, but changing the laser design so that the output DBR mirror has a lower reflectivity will also have a significant effect.

The SMSR of these devices was at least 20 dB. The SMSR could be further increased by increasing the feedback strength by reducing the mirror reflectivity or increasing the SOA gate bias. However, increasing the feedback strength might also reduce the wavelength stability of the device. Further modeling and design experiments should give more insight in these effects.

6.7.2 Switching speed

The theoretical investigation of the filtered feedback concept shows that nanosecond wavelength switching speeds are possible. Previous experiments with devices operating with a similar feedback concept [5,6] showed confirmation of the very fast switching speeds that can be obtained using feedback to switch an FP laser. However, full dynamic characterization was not yet done and is currently hampered due to electrical impedance matching issues.

If the predicted switching speed can be realized, the current IFF-TL will be a factor 10-1000 faster than today's state of the art tunable lasers [2]. The ns switching speed will make the device suitable for packet switching, which is believed to be a large application area in future optical communication networks, because it makes the overall network much more flexible in terms of bandwidth allocation, dynamical routing, error checking, etc.

6.7.3 Temperature effects

Because the gate switches are placed outside the laser cavity, temperature changes due to the switching currents do not affect the lasing wavelength. This was shown in figure 6.15.

Wavelength drift due to changes in temperature can be a big problem in tunable lasers using integrated tunable DBR mirrors that are tuned by current injection [21]. The temperature behavior can be predicted using various time constants. A control scheme that pre-compensates these temperature drifts can then be designed, but this complicates the control electronics significantly.

Matsuo et al. [5] already demonstrated an early version of a laser based on the IFF-TL concept, using a continuously tunable filter made of two ring resonators. In their first experiments they show a reduction in optical frequency drift from 7 to 1 GHz. A similar effect is expected in the AWG-based IFF-TL devices since the frequency drift is caused by a phase shift of the feedback light, and the gate switches used in these devices have similar path lengths as the tunable rings used in the device presented by Matsuo et al. However, results from [7] show that the gate length might be reduced significantly, which will lead to lower switching currents and therefore less temperature induced frequency drift.

6.7.4 Reliability

The laser presented in this chapter is the first demonstration of an AWG-based IFF-TL with deep etched DBR mirrors. The device concept inherently provides some interesting features concerning stability of the operation over a long time period.

The first measurement results show that the currents required to switch the IFF-TL device have a large tolerance in operation point. This makes the control easier, but it also has advantages for the long term reliability of the laser. Aging effects due to an increase in crystal defects in the tuning sections [22] have a smaller impact and a larger drift in control currents can be tolerated.

6.7.5 Control electronics

Existing tunable lasers can address more than 100 WDM channels with only 4 analog control currents (gain, 2 tunable DBR mirrors and a phase control section). However, to find the right combination of current settings to obtain a stable operating point requires a complex tuning table and intelligent electronics. The quasi-digital operation scheme of the AWG-based IFF-TL reduces the complexity of the electronics required to control the laser. However, the total number of control currents can become large as the number of wavelength channels increases. Furthermore it might be necessary to include a phase control section in future designs.

Keeping the control electronics simple is important since the cost of the electronics is a major part of the total price of the tunable lasers that are commercially available nowadays. A reduction of these costs would make this device more interesting in high volume, low cost applications like metro and access networks.

6.7.6 Number of wavelengths

The device presented in this paper has 4 wavelength channels determined by the AWG. The concept can easily be extended to a larger number of wavelengths, but increasing the density of the AWG channels also results in a larger AWG. The surface of the AWG roughly increases by a factor of 1.5 when the channel spacing is reduced by a factor of 2. The advantage of having a denser channel spacing in the AWG, while keeping the same FP-laser mode spacing is that the 50 GHz mode hops that were observed in Figure 6.16 would occur less often. This could also be achieved by decreasing the FP laser length so that the mode spacing of the laser becomes larger (e.g. 100 GHz). This would however result in a reduction of the output power. Furthermore, it might be more difficult to find an operation current were the feedback signal is in phase with the laser output signal. Future chip designs should give more insight in this matter.

The current AWG design is the same as what one would use as a demultiplexer in a WDM network. This means that cross-talk levels are low (usually lower than -15 dB) and extinction loss is minimized. However, for the laser to operate with a good SMSR, larger

crosstalk levels can be tolerated. Even -3 dB crosstalk might be sufficient since the feedback light passes the AWG twice. Also the extinction loss can be higher. It is therefore expected that the size of the AWG can be reduced. With these modifications it is expected that with a 50 GHz AWG the number of wavelengths in the device can be increased to 32.

6.7.7 Conclusion & outlook

The AWG-based IFF-TL demonstrates the new possibilities in PIC design that are offered by deep etched DBR gratings. With these integrated mirrors it is possible to make an FP laser with a well-defined cavity length and mode spacing. Also, the feedback circuit can be placed right next to the main laser cavity, minimizing the delay of the feedback signal. This is important since the delay plays an important role in the stability of feedback lasers.

The new concept of the IFF-TL combines high switching speeds with easy wavelength control. The number of wavelengths in the current device is limited to 4, but the concept can be extended to more wavelengths. In the present device the fiber-coupled power is low, but improved designs should allow for higher output powers, for example by reducing the reflectivity of the front DBR grating. The 800 μm cavity should in principle allow for at least 10 mW of output power.

This is the first realization of this new concept using an AWG filter. In future designs it is possible to reduce the size of the AWG, which occupies a large part of the chip area, by sacrificing a little on the performance of the filter. This way the number of wavelengths can be increased without increasing the size of the component.

More optimization cycles are also planned to gain further insight in the requirements for the DBR mirrors. The current device has a 2-period DBR mirror between the laser and the AWG. The transmission properties determine the feedback power in the laser cavity. It will therefore affect many aspects of the device such as switching speed, wavelength stability, sensitivity to feedback phase, etc. Also the mirror on the output side of the laser can be optimized for maximum output power.

Currently the predicted dynamical behavior was not measured yet. Electrical impedance matching of the SOA gates is the limiting factor at the moment. In the near future we expect to get more results on the switching behavior and the wavelength stability. We also plan to characterize more devices with smaller AWG channel spacing and larger number of wavelength channels.

In this chapter we have focused on applications in optical telecommunication networks. However, the device is also interesting for laser dynamics research. A lot of research has been done on feedback effects in semiconductor lasers. Matching the theory with experiments is difficult when working with discrete components. The current device offers scientist a more controlled environment to study feedback effects. It is therefore not only a promising device in a commercial sense, but also for further scientific research.

References

1 L. A. Coldren, "Monolithic tunable diode lasers," IEEE J. Sel. Topics in Quantum Electronics, vol.6, no.6, pp.988-999, Nov/Dec 2000

2 J. Buus, E. J. Murphy, "Tunable Lasers in Optical Networks," J. Lightwave Technol. Vol. 24, pp. 5, 2006

3 L. A. Coldren, G. A. Fish, Y. Akulova, J. S. Barton, L. Johansson, and C. W. Coldren, "Tunable Semiconductor Lasers: A Tutorial," J. Lightwave Technol. No. 22, pp. 193, 2004

4 B. Docter, S. Beri, F. Karouta, M.K. Smit, "Semiconductor laser device", International patent #PCT/NL/2008/000185, filed August 01, 2008

5 S. Matsuo, T. Segawa, T. Kakitsuka, T. Sato, R. Takahashi, H. Suzuki, B. Docter, F. Karouta, M.K. Smit, "Integrated filtered feedback tunable laser using double-ring-resonator-coupled filter," IEEE 21st International Semiconductor Laser Conference, 2008. ISLC 2008., vol., no., pp.155-156, 14-18 Sept. 2008

6 S. Furst, S. Yu, M. Sorel, "Fast and Digitally Wavelength-Tunable Semiconductor Ring Laser Using a Monolithically Integrated Distributed Bragg Reflector," IEEE Phot. Tech. Letters, vol.20, no.23, pp.1926-1928, Dec.1, 2008

7 A. La Porta, M.J.R. Heck, X.J.M. Leijtens, L.M. Augustin, T. de Vries, E. Smalbrugge, Y.S. Oei, R. Nötzel, R. Gaudino, D.J. Robbins, M.K. Smit, "Monolithic AWG-based discretely tunable laser with nanosecond switching speed". 21st Annual Meeting of the IEEE LEOS PD session, 2008

8 ITU-T G.694.1, "Spectral grids for WDM applications: DWDM frequency grid," May 2002

9 M.K. Smit, C. van Dam, "PHASAR-based WDM-devices: Principles, design and applications," IEEE Journal of Selected Topics in Quantum Electronics, vol.2, no.2, pp.236-250, Jun 1996

10 Y. A. Akulova, G. A. Fish, P.-C. Koh, C. L. Schow, P. Kozodoy, A. P. Dahl, S. Nakagawa, M. C. Larson, M. P. Mack, T. A. Strand, C. W. Coldren, E. Hegblom, S. K. Penniman, T.Wipiejewski, and L. A. Coldren, "Widely tunable electroabsorption-modulated sampled-grating (DBR) laser transmitters," IEEE J. Sel. Topics Quantum Electron., vol. 8, no. 6, pp. 1349–1357, Nov./Dec. 2002

11 A. J. Ward, D. J. Robbins, G. Busico, E. Barton, L. Ponnampalam, J. P. Duck, N. D.Whitbread, P. J.Williams, D. C. J. Reid, A. C. Carter, and M. J.Wale, "Widely tunable DS-DBR laser with monolithically integrated SOA: Design and performance," IEEE J. Sel. Topics Quantum Electron., vol. 11, no. 1, pp. 149–156, Jan./Feb. 2005

12 J.-O. Wesström, G. Sarlet, S. Hammerfeldt, L. Lundqvist, P. Szabo, and P.-J. Rigole, "State-of-the-art performance of widely tunable modulated grating Y-branch lasers," presented at the Optical Fiber Communication (OFC), Los Angeles, CA, Feb. 2004, Paper TuE2

13 J.H. den Besten, R.G. Broeke, M. van Geemert, J.J.M. Binsma, R. Heinrichsdorff, T. van Dongen, E.A.J.M. Bente, X.J.M. Leijtens, M.K. Smit, "An integrated coupled-cavity 16-wavelength digitally tunable laser," IEEE Photonics Technology Letters, vol.14, no.12, pp. 1653-1655, Dec 2002

14 Y. Barbarin; X.J.M. Leijtens; E.A.J.M. Bente; C.M. Louzao; J.R. Kooiman; M.K. Smit, "Extremely small AWG demultiplexer fabricated on InP by using a double-etch Process," IEEE Photonics Technology Letters, vol.16, no.11, pp.2478-2480, Nov. 2004

15 H. G. Bukkems, "New Approaches to Widely Tunable Semiconductor Lasers", PhD thesis, Technische Universiteit Eindhoven, The Netherlands, 2006

16 B. Docter, F. Karouta, E.A.J.M. Bente, T. de Smet, M.K. Smit, "Short-cavity lasers with deeply etched DBR mirrors for photonic integrated circuits". Proc. Symp IEEE/LEOS Benelux Chapter, Twente, Netherlands, 2008

17 R. Lang, K. Kobayashi, "External optical feedback effects on semiconductor injection laser properties," IEEE Journal of Quantum Electronics, vol.16, no.3, pp. 347-355, Mar 1980

18 M. Yousefi; D. Lenstra, "Dynamical behavior of a semiconductor laser with filtered external optical feedback," IEEE Journal of Quantum Electronics, vol.35, no.6, pp.970-976, Jun 1999

19 J.J.M. Binsma, M. van Geemert, F. Heinrichsdorff, T. van Dongen, R.G. Broeke, E.A.J.M. Bente, M.K. Smit, "MOVPE Waveguide Regrowth in InGaAsP/InP with Extremely Low Butt-Joint Loss", Proc. IEEE/LEOS Symp. Benelux chapter, Brussels, 2001

20 R.G. Broeke, J.J.M. Binsma, M. van Geemert, T. de Vries, Y.S. Oei, X.J.M. Leijtens, M.K. Smit, "Monolithical Integration of Semiconductor Optical Amplifiers and Passive Modefilters for Low Facet Reflectivity", Proc. IEEE/LEOS Symp. Benelux chapter, Brussels, 2001

21 B.Moeyersoon, J.Wittebolle, G.Morthier, "Wavelength switching of semiconductor tunable lasers - how to suppress thermally induced wavelength drift", Proc. Symp. IEEE/LEOS Benelux Chapter, Amsterdam, 2002

22 S.L. Woodward, P. Parayanthal, U. Koren, "The effects of aging on the Bragg section of a DBR laser," IEEE Photonics Technology Letters, vol.5, no.7, pp.750-752, Jul 1993
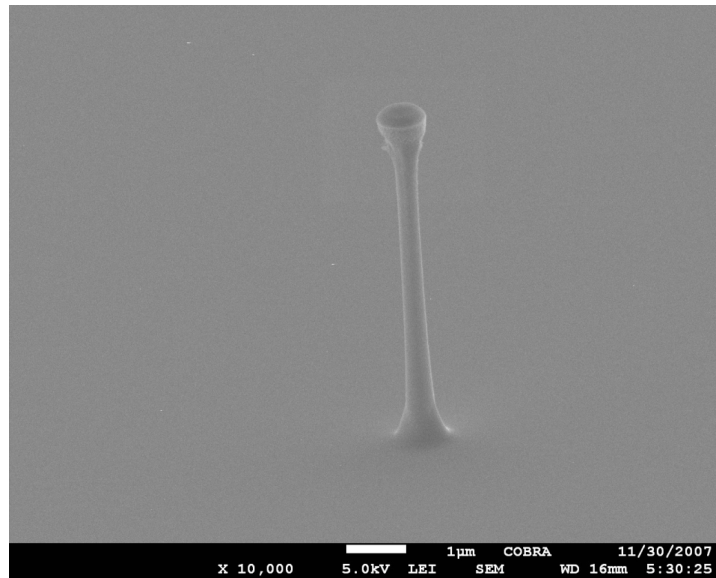
"Nano lamp post"

Sometimes small dust particles can lead to interesting results.
Nano-pillar etched about 4 μm deep in InP.

7 Conclusions and outlook

7.1 Conclusions

DBR mirrors offer a lot of functionality in Photonic Integrated Circuits (PICs). With the deeply etched mirrors a high reflectivity can be obtained within only a few periods. The mirrors can be placed anywhere on the chip, creating new possibilities in PIC design. The Integrated Filtered Feedback Tunable Laser (IFF-TL) device presented in chapter 6 is a good example of one of these new possibilities. Other possible applications are (active-) Fabry-Perot etalons, AWG filters with mirrors in the phased array arms, coupled cavity lasers used as flip-flop memory elements, etc.

The focus of this thesis is on the development of the new component in such a way that it can be combined with existing active and passive components in a generic integration technology. We reviewed the required simulation tools and investigated the design parameters (chapter 2), described the current state of the technology and its limitations (chapter 3), showed the advances in fabrication technology (chapter 4) and presented new characterization methods to measure the performance of deeply etched DBR mirrors (chapter 5).

7.1.1 Device modeling

For the modeling of deeply-etched DBR gratings, various simulation algorithms can be used. When the refractive index difference between the grating sections is not very large a Coupled Mode Theory approach is very efficient. However, as the refractive index increases, a more robust method based on accurately calculating the guided and radiating modes in each section of the grating (Bi-directional Eigenmode Propagation (BEP) method) gives more accurate results. However, the BEP method is limited to 2D analysis of the structure, while for the deeply etched DBR mirrors it is important to take the diffraction of the light in the horizontal as well as the vertical direction into account. Therefore a 3D FDTD approach is most suitable. It also has the advantage that the entire spectral behavior is obtained from a single simulation run. But because the method requires a lot of computer resources, only small structures can be analyzed.

It was found that for a deeply etched DBR grating, the sidewalls need to be vertical, with less than 5° deviation. It was also shown that a 3rd order grating design can still provide a sufficient reflection bandwidth (>200 nm). Also filling the grating with a polymer (i.e. BCB) used for planarization does not prevent the DBR mirrors from having a high reflectivity (>90%) within a limited number of periods (<6).

It was found that the ideal length of the gaps in a 3rd order mirror design is 825 nm. This is slightly more than the values expected from a simple plain-wave approach (750 nm). This is due to the divergence of the field in the gap regions.

7.1.2 Short cavity DBR lasers

The short-cavity DBR lasers based on Vertical Groove (VG) gratings presented in chapter 3 are suitable components for future all-optical logic circuitry, since they operate with low power consumption. Therefore the heat generated when many of these lasers are integrated on a single chip is still manageable.

However, a further reduction in size and power consumption was not possible with these devices based on VG gratings. The total device size was limited by the size of the DBR mirrors, which were 50 and 80 μm long, and by connecting the gratings to the gain section with tapered waveguides of 26 μm length. This limits the size of the smallest devices to 207 μm.

A large reduction in size can be expected when replacing the vertical groove gratings by deeply etched gratings.

7.1.3 Fabrication technology

The fabrication process that was developed to realize deeply etched DBR gratings in complex PICs was described in chapter 4. A new etching process and a new masking process that allows the combination of EBL and optical lithography for the fabrication of deeply-etched DBR mirrors were demonstrated. Also the impact of changing the etching process on the other processing steps was shown.

The new fabrication process adds the DBR mirror building block to the existing range of building blocks (shallow- & deep waveguides, SOAs, phase modulators, etc.). The addition of the DBR mirrors does not compromise the performance of the other components.

7.1.4 Characterization of deeply etched DBR mirrors

In chapter 5 several passive and active chips that were processed using the new fabrication technology were characterized. The shortest lasers that were working in CW operation at room temperature were only 80 μm long.

A new sub-threshold measurement technique based on Fabry-Perot resonance characterization was presented. This method is very suitable to determine the reflection properties of the DBR mirrors over a wide wavelength range.

In the all-active devices, however, the DBR reflectivity is much lower than what we expected from simulations. Also the expected trend of higher reflectivity as the number of periods increase was not observed. It was shown that this was caused by the all-active, highly absorbing material that was used in the waveguide connecting the DBR mirror with the amplifier section. This problem was solved by using an active-passive material system for the next set of devices.

7.1.5 Integrated Filtered Feedback Tunable Laser

The novel tunable laser presented in chapter 6 is a good demonstration of the new possibilities in PIC design that are created by the deeply etched DBR gratings. The DBR mirrors allow us to make a Fabry-Perot laser with a well-defined cavity length and mode spacing matching with the ITU grid for telecommunication wavelengths. A feedback circuit can be placed right next to the FP laser cavity. This feedback circuit contains an AWG wavelength filter and an SOA gate array that can be used to select one of the FP modes and rapidly switch between them.

The first realization of this device shows stable laser operation over a large range of input currents. This shows that temperature changes due to switching currents have very little effect on the laser performance.

Simulations show that wavelength switching speeds in the order of 1 ns are possible. Unfortunately this has not been verified with measurements yet. The control of the device is very easy, since most of the inputs can be operated over a wide current range, making the operation 'quasi-digital'.

The total surface area of the circuit is less than 2 mm^2, which means that approximately 1750 chips can be made from a 3" wafer.

7.1.6 General conclusion

The DBR technology developed in this research project offers a lot of new possibilities to create new devices in PICs. The addition of the deeply etched DBR grating as a new building block does not compromise the performance of other building blocks.

7.2 Outlook

The deeply etched DBR gratings can be used as a new building block in many PIC applications. The application of the mirrors is not limited to the tunable laser presented in chapter 6. It also allows the realization of (active-) Fabry-Perot etalons (which can work as a wavelength locker), AWG filters with mirrors in the phased array arms (reducing the size of the AWG), or coupled cavity lasers (used as flip-flop memory elements), etc. More research should be done however on the characterization of the DBR mirrors. For this purpose, short-cavity DBR lasers should be fabricated in an active-passive material system.

The device that served as a demonstrator for the new DBR technology, the novel IFF-TL, is a very promising device in terms of switching speed and ease of control. The very fast switching speed that is predicted by the first modeling efforts makes the device promising for packet switching applications. Furthermore, the device

shows a low sensitivity to variations in control currents. This potentially reduces the cost of the control electronics compared to the current continuously tunable lasers.

The number of wavelengths in the current device is limited to only 4, but the concept can be extended to more wavelengths. In principle a channel spacing of 50 GHz is possible which would extend the number of channels to 32. Although the output power is very low, new designs are planned to improve this. In these new designs we also plan to further investigate the requirements on feedback strength and phase in order to get an optimal performing device.

The IFF-TL device also offers scientists a better controllable environment to study the effect of optical feedback in semiconductor lasers. It is therefore expected that the device is not only promising for commercial applications, but also interesting for fundamental research on semiconductor lasers.
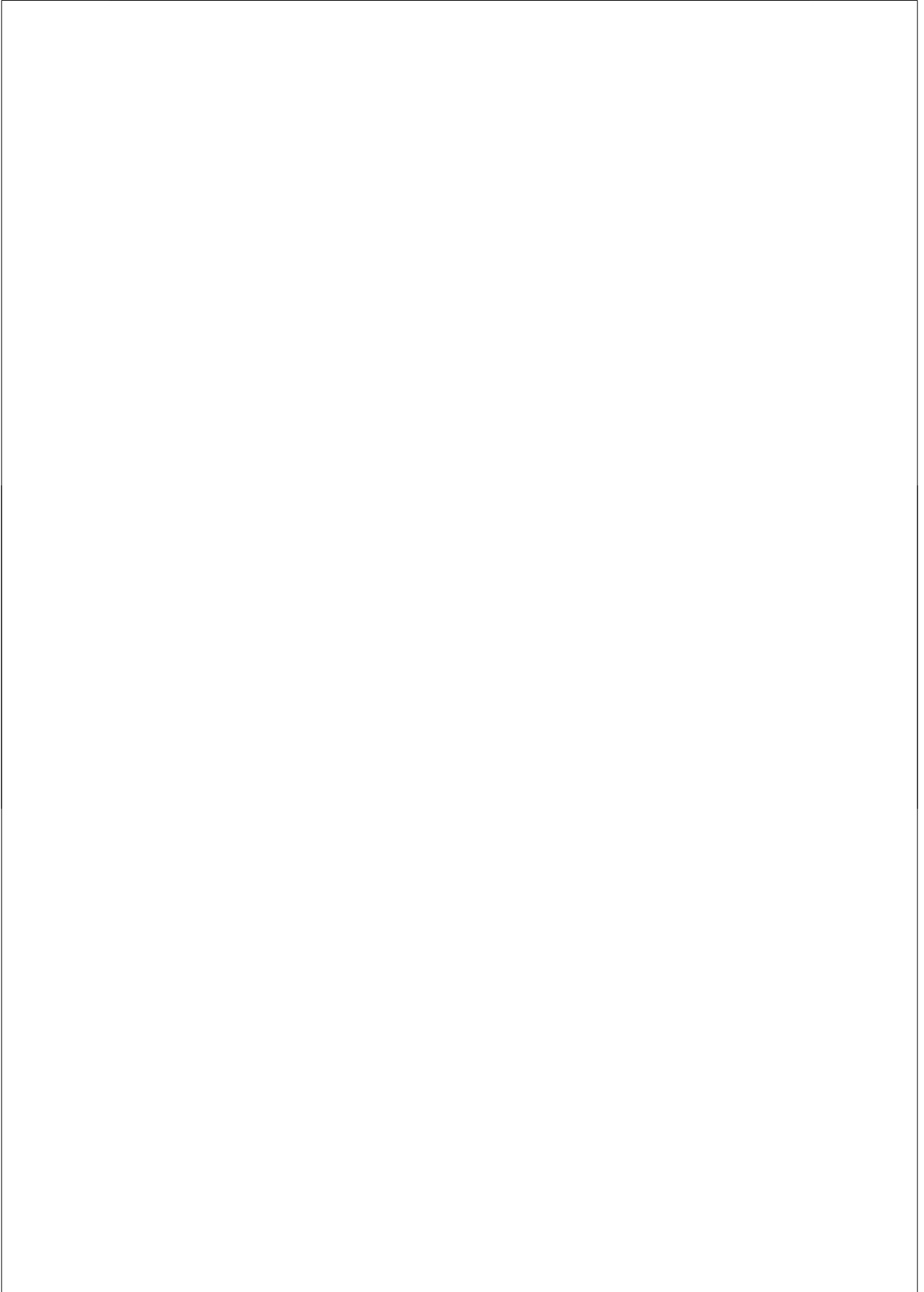
Appendix A – Process flow

This appendix describes the full process flow of the active-passive process including deeply-etched DBR mirrors. Its main purpose is for reference in the COBRA cleanroom, hence the specific mention of recipe names and numbers. Where applicable, references to other sections of the thesis are given.

The process flow also contains a sub-section for the formation of n-contacts at the top of the chip (**Top-n-contact wet etch**). These contacts can be used to create high speed switches. This step was recently added to the process flow, and is still under development. Since it is not used in the devices presented in this thesis it was not mentioned in the process description in chapter 4.

Cleaning
10 min O_2 stripper
2 min 10:1 $H_2O:H_3PO_4$
$HCl:H_3PO_4$ 1:4 1 min

Mask layer deposition
PECVD SiO_x 300hf $SiH_4:N_2:N_2O$ 8.5:161.5:710 sccm, 1000 mTorr, 300°C, 20W, 6 min (~440nm)

EBL alignment markers
HPR504 standard litho (MA-6):
       HMDS primer oven, standard recipe
       Spin HPR504 3000 rpm, 30s
       Soft bake 100°C 2m30s
       MA-6 exposure 3.9s (EBL alignment mask)
       Post exposure bake 115°C 2m30s
       Develop PLSI:H_2O 1:1 1m15s
       5 min O_2 stripper 50W (recipe 5)
       Hard bake 120°C 2 min
Nitride RIE std. wg. process $CHF_3:O_2$ 50:5 sccm, 56 mTorr, 100W, 15 min
10 min O_2 stripper 300W (recipe 7)
InP RIE std. process 10 cycles (~ 1 µm deep):
    -   2 min $CH_4:H_2$ 20:80 sccm, 60 mTorr, 220W
    -   4 sec O_2 100 sccm, 100 mTorr, 200W

E-beam DBR lithography
BVR e-beam evaporator 50 nm Cr
Spin ZEP (5000 rpm, 40s)
Bake (100-150°C 4 min, 200°C 2 min)
Raith EBL exposure (DBR patterns, see section 4.2.5)
Develop ZEP (1 min, 45s rinse)
ICP Cr etch $Cl_2:O_2$ 15:15 sccm, 10 mTorr, 500W ICP, 5W RF, 60°C, 1 min
water rinse 5-10 min
strip ZEP in n,n-dimethylacethamide (30s)
IPA rinse, blow dry

Optical waveguide lithography
HDMS primer oven, standard recipe
HPR504 standard litho (same as above, but no O_2 strip-step, using waveguide mask)
1% HF dip (1-2s)
ICP Cr etch Cl_2:O_2 15:15 sccm, 10 mTorr, 500W ICP, 5W RF, 60°C, 1 min
water rinse 5-10 min
Nitride RIE O_2 20 sccm, 15 mTorr, 50W, 1 min to break top of resist layer
Strip HPR with acetone spray
IPA rinse, blow dry

Mask etching
Nitride RIE CHF_3 60 sccm, 15 mTorr, 50W, 26 min
30 min O_2 stripper 300W (recipe 7)
2 min 10:1 H_2O:H_3PO_4

Shallow-deep definition
Spin PI2737 3000rpm 90s
Bake 40°C - 90°C 5 min.
MA-6 exposure 90s (shallow-deep mask)
Develop in DE 9040 40s
Rinse in RI 9140 40s, blow dry
Vacuum oven PI2737 recipe (325°C)

Deep etch
ICP Cl_2:Ar:H_2 7:4:12, 4 mTorr, 60°C, 750W ICP, 150W RF, 2m30s (see section 4.3.4)
water rinse 5-10 min
10 min O_2 stripper 300W
2 min 10:1 H_2O:H_3PO_4
1% HF dip (1-2s)

Shallow etch
ICP CH_4:H_2, 2.1 µm deep, ~21 cycles dep. etch rate:
    - CH_4:H_2 30:10 sccm, 200W ICP, 180W RF, 10 mTorr, 60°C, 1 min
    - O_2 40 sccm, 200W ICP, 180W RF, 10 mTorr, 60°C, 10 sec

Surface passivation
BHF 2 min
10 min O_2 stripper 300W (recipe 2)
2 min 10:1 H_2O:H_3PO_4
H_2SO_4:H_2O_2:H_2O 1:1:100 1 min.
BHF 10 min
PECVD SiO_x 300hf (see above) 1 min (~75nm)

Top-n-contact wet etch
Spin AZ4533 2000 rpm, 30 s
softbake 100°C 50s
MA-6 exposure 45s (n-contact mask)
develop AZdev:H2O 1:1 2m30s
Microscope check
hardbake 115°C 50 sec.
BHF 1 min

Appendix A

Q wet etch (H_2SO_4:H_2O_2:H_2O 1:1:10) 5 min
strip AZ4533 in with acetone & IPA

Planarization
pre-bake on hotplate 150°C, 5 min
Spin AP3000 (recipe Q)
Spin BCB 3022-46 5000 rpm max (recipe P)
Soft bake 120°C, 2 min
Vacuum oven PI2723 recipe (325°C)
Nitride RIE BCB etch O_2:CHF_3 20:4 sccm, 50W, 50 mTorr, 5 min. (sample upside down to clean backside)
Nitride RIE BCB etch O_2:CHF_3 20:4 sccm, 50W, 15 mTorr, 1-2 min. (make sure wgs. are open)

Passive waveguide protection with SiO_x (better contact adhesion on BCB)
PECVD SiO_x 300hf (see above) 6 min (~400 nm)

BCB removal
Spin AZ4533 2000 rpm, 30s
softbake 100°C, 50s
MA-6 exposure 45s (BCB mask)
develop AZdev:H_2O 1:1 2m30s
hardbake 115°C 50s
BHF 2 min
strip AZ4533 in with acetone & IPA
Nitride RIE BCB etch O_2:CHF_3 20:4 sccm, 50W, 15 mTorr, 35 min.

Open Contacts
Spin AZ4533 2000RPM, 30s
softbake 100°C 50s
MA-6 exposure 45s (contact mask)
develop AZdev:H_2O 1:1 2m30s
hardbake 115°C 50s
Nitride RIE CHF_3 60 sccm, 15 mTorr, 50W, 26 min
Strip resist:
       Nitride RIE BCB etch O_2:CHF_3 20:4 sccm, 50W, 15 mTorr, 1m15s
       Acetone & IPA spray
       Nitride RIE BCB etch O_2:CHF_3 20:4 sccm, 50W, 15 mTorr, 1m15s

Metallization
Spin MaN-440 2000 rpm, 30s
Softbake 90°C, 5 min
MA-6 exposure 4x100s (metallization mask)
Develop MaD-332, 90 s
H2SO4:H2O2:H2O 1:1:100 60 sec. (etch top of contact layer)
FC2000 e-beam evaporator Ti/Pt/Au 60/75/300 nm
Lift-off in acetone (1 hour in vapour, 1 hour soak, then spray)
FC2000 e-beam evaporator Ti/Pt/Au 60/75/200 nm
Anneal 325°C, 30s.
Measure IV characteristics
repeat anneal / IV characterization

Plating

Sputter 100 nm Au seed layer
Spin AZ4533 2000RPM, 30 s
softbake 95°C 20 min
MA-6 exposure 37.5 s
develop AZdev:H_2O 1:1 2m30s
hardbake 120°C 20 min
O_2 stripping 50W 5 min (recipe 5)
paint backside of sample with resist & bake
Electroplating, 40 cycles ~ 1µm
SiN RIE PI etch O_2:CHF_3 20:2 sccm, 50W, 15 mTorr, 1 min
remove resist with acetone & IPA
etch back seed layer in KCN (Degussa)

Cleaving & finishing

Cleave sample using scriber & manual cleave
Epotec chips on copper chucks
Bake in oven 150°C 30 min
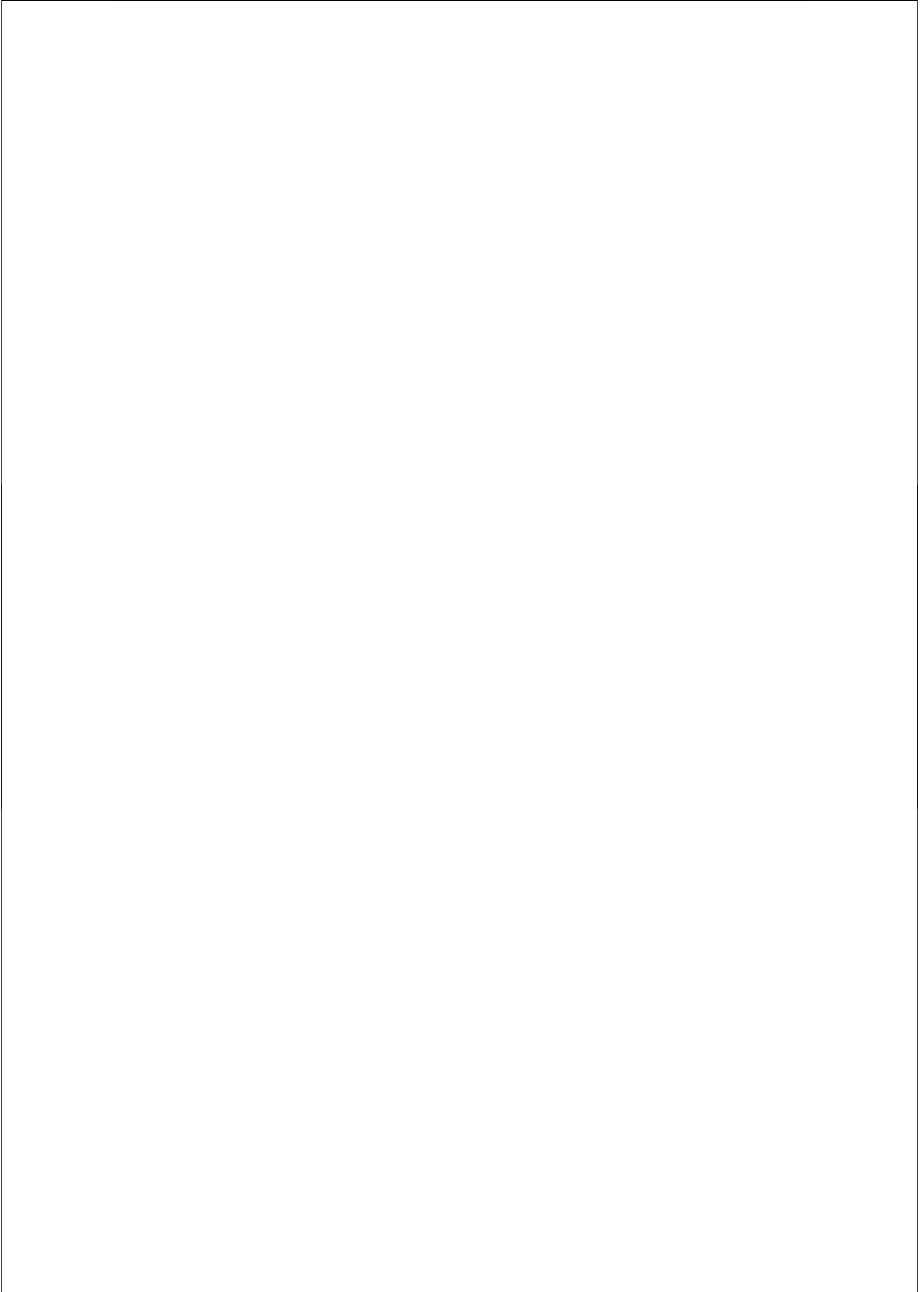
Summary

Deeply-etched DBR mirrors for Photonic Integrated Circuits and Tunable Lasers

Deeply-etched Distributed Bragg Reflector (DBR) mirrors are a new versatile building block for Photonic Integrated Circuits that allows us to create more complex circuits for optical telecommunication applications.

The DBR mirrors increase the device design flexibility because the mirrors can be placed anywhere on the chip. This enables the realization of compact lasers (<100 μm) that can be used as low power signal sources in complex (digital) circuits. The DBR mirrors can also be used to create lasers with a very well defined cavity length, controlling the wavelengths of the emitted light accurately.

This thesis contains an overview of the current State-of-the-Art in DBR reflectors in Photonic Integrated Circuits (PICs). The design theory is explained and the performance of the mirrors is described with several simulation models.

A major part of the thesis describes the technological advances that were made to realize the deeply-etched DBR mirrors in such a way that they can be integrated with other active and passive components to create complex PICs.

New characterization methods were developed to analyze the mirror performance. These methods were demonstrated with the realization and characterization of short-cavity lasers using various material compositions.

As a demonstration of the new possibilities that the DBR mirrors offer, a novel tunable laser is presented. The Integrated Filtered Feedback Tunable Laser (IFF-TL) combines DBR mirrors with active laser and switching components and passive wavelength filters. This laser concept is expected to allow faster switching between the wavelengths, because of the lower thermal drift. Also the electronic control of the laser is much simpler compared to today's state-of-the-art tunable lasers. It is therefore a promising component for future all-optical packet-switching networks and low cost Fiber-To-The-Home (FTTH) applications.
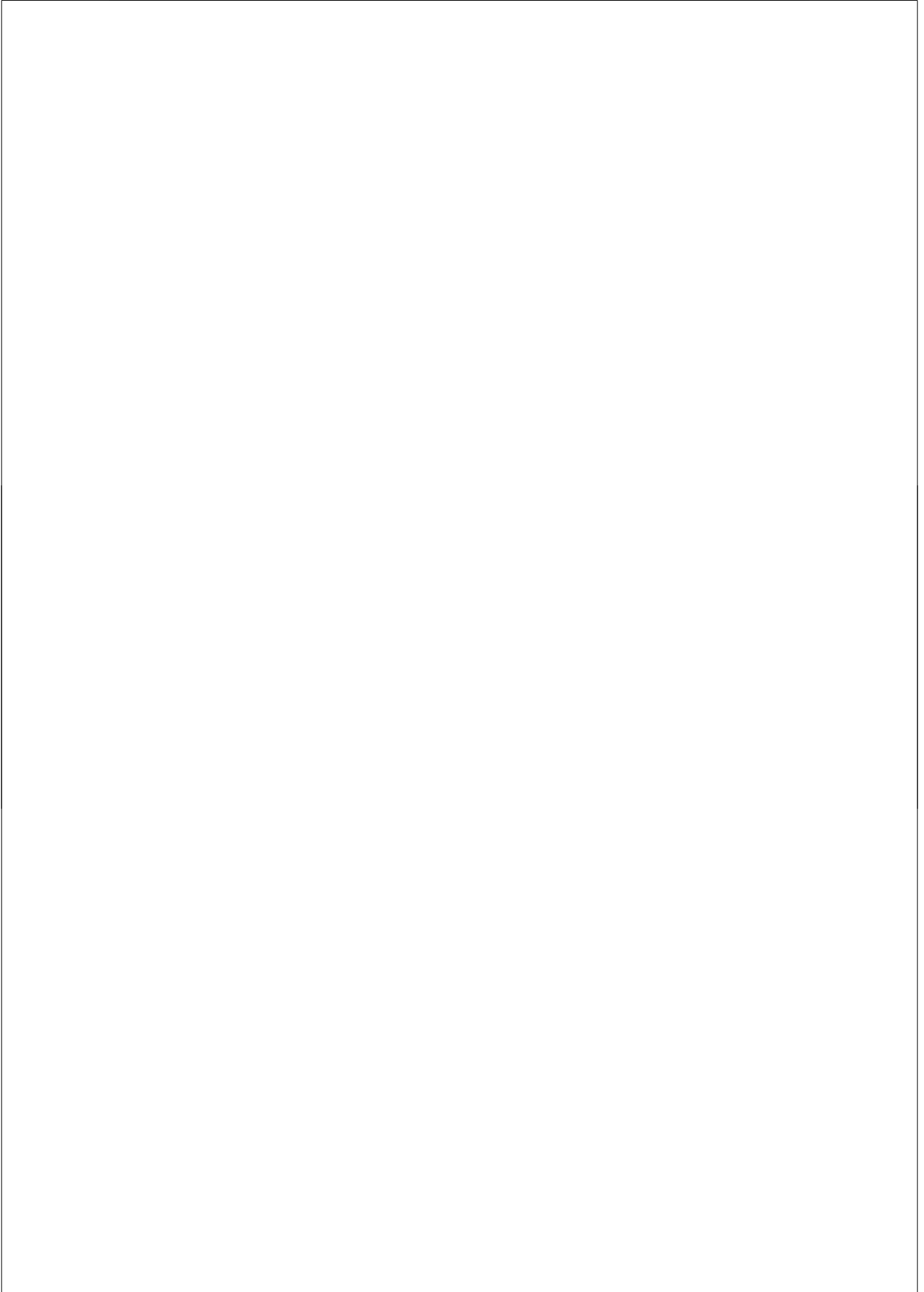
Dankwoord

Juist, het dankwoord… Het meest gelezen hoofdstuk van een proefschrift, terwijl het vaak als laatste even snel opgesteld wordt, op het moment dat de deadline het eigenlijk niet meer toelaat... Of ben ik daarin uniek? Vast niet!

De eerste die uiteraard bedankt moet worden is mijn promotor Meint die me een plek in de OED groep aanbood, ondanks dat ik bij mijn sollicitatie aangaf niet een echte wetenschapper te zijn. Als je maar een werkende chip maakt was het antwoord. Nou dat is gelukt, en ik heb er ook nog een proefschrift over proberen te schrijven. Wie weet heeft dat me toch een beetje wetenschapper gemaakt...

Fouad, bedankt voor al je begeleiding, vooral in de cleanroom. Ik vond het fijn om met je samen te werken. Bedankt dat je me af en toe lekker eigenwijs liet zijn. Jos, bedankt voor je hulp bij het tot stand komen van dit werk. Jouw suggesties en adviezen waren onmisbaar tijdens het schrijfproces. Many thanks also to the rest of my promotion committee: Mike, Ton, Jan, your corrections were very much appreciated.

Ben, Barry, Erik-Jan, Tjibbe, Kitty & Jeroen: jullie zijn de echte helden van OED! Dankzij jullie inzet kunnen wij chips maken. Bedankt voor alle hulp in de cleanroom, van jullie heb ik ongetwijfeld het meeste geleerd de afgelopen 4 jaar. Hans, de IT bij OED is altijd OK! Els, Susan en Jose, bedankt voor de administratieve ondersteuning.

Erwin, bedankt voor je hulp bij de karakterisatie van de vele chips. Xaveer, door jouw werk is chip-ontwerp een fluitje van een cent! Siang, bedankt voor het uitleggen van de wondere wereld die RIE etsen heet. Huub, je bent nog niet zo lang geleden bij OED begonnen, maar ik ga je toch vast bedanken voor je waardevolle input in het vervolgtraject dat we gaan starten. En dan kom ik vanzelf bij Jan-Hein: bedankt voor je intresse in mijn gezwets over optische chips. Door jouw enthousiasme ligt er een mooie toekomst in het verschiet. Ik ben benieuwd waar we uit gaan komen!

Stefano, for you I reserve a special place. Not only did you do a great job in getting the STW EFFECT proposal accepted, you made it possible that we now have a great collaboration with Jan and Ilya in Brussels. Thanks for the modeling efforts that you have made already and I hope we can continue the good work in the future.

I would also like to thank all the colleagues at NTT. Suzuki-san, Matsuo-san, Kakistuka-san and of course my dear friend Toru: thank you for the great time during my stay in Japan. Your country is one of the most amazing places I've seen in

List of publications

Journal articles

A.A.M. Kok, E.J. Geluk, B. Docter, J.J.G.M. van der Tol, R. Nötzel, M.K. Smit, R.G.F. Baets, "Transmission of pillar-based photonic crystal waveguides in InP technology," Applied Physics Letters, 91(20), pp. 201109, 2007.

B. Docter, T. Segawa, T. Kakitsuka, S. Matsuo, T. Ishii, Y. Kawaguchi, Y. Kondo, H. Suzuki, F. Karouta, M.K. Smit. "Short-cavity DBR laser using vertical groove gratings for large-scale photonic integrated circuits," IEEE Photonics Technology Letters, 19(19), 1469-1471, 2007.

D.J.W. Klunder, F.S. Tan, T. van der Veen, H.F. Bulthuis, G. Sengo, B. Docter; H.J.W.M. Hoekstra, A. Driessen, "Experimental and numerical study of SiON microresonators with air and polymer cladding," Journal of Lightwave Technology, vol.21, no.4, pp. 1099-1110, 2003

Patents

B. Docter, S. Beri, F. Karouta, M.K. Smit, "Semiconductor laser device", Int. patent #PCT/NL/2008/000185, filed August 01, 2008

Conferences

B. Docter, J. Pozo, F. Karouta, S. Beri, I.V. Ermakov, J. Danckaert, M.K. Smit, "Novel Integrated Tunable Laser using Filtered Feedback for simple and very fast tuning," Proc. 35th European Conference on Optical Communication (ECOC), session 8.2, 20-24 sept. 2009, Vienna, Austria

L. Xu, X.J.M. Leijtens, B. Docter, T. de Vries, E. Smalbrugge, F. Karouta, M.K. Smit, "MMI-Reflector: A Novel On-chip Reflector for Photonic Integrated Circuits", Proc. 35th European Conference on Optical Communication (ECOC), poster 2.24, 20-24 sept. 2009, Vienna, Austria

B. Docter, J. Pozo, F. Karouta, M.K. Smit, "Novel integrated tunable laser for optical communication systems", 3[e] Fotonica Evenement, 3 apr. 2009, Nieuwegein, The Netherlands

F. Karouta, B. Docter, E.J. Geluk, M.K. Smit, P. Kaspar, "Three level masking for improved aspect ratio InP-based photonic crystals," 20th International Conference on Indium Phosphide and Related Materials, IPRM 2008, 25-29 May 2008. (pp. 1-4), Versailles, France

F. Karouta, B. Docter, A.A.M. Kok, E.J. Geluk, J.J.G.M. van der Tol, M.K. Smit, "High aspect ratio etching and application in InP-based photonic integrated circuits," Proc. ECS Fall Meeting 2008, Symposium Integrated Optoelectronics (E5). Honolulu, Hawaii

B. Docter, F. Karouta, E.A.J.M. Bente, T. de Smet, M.K. Smit, "Short-cavity lasers with deeply etched DBR mirrors for photonic integrated circuits," Proc. Symposium IEEE/LEOS Benelux Chapter (pp. 39-42), 27-28 November, 2008, Twente, The Netherlands

B. Docter, F. Karouta, E.A.J.M. Bente, T. de Smet, M.K. Smit, "Short-cavity lasers with deeply etched DBR mirrors for photonic integrated circuits," Proc. European Semiconductor Laser Workshop 2008, September 19-20, Eindhoven, The Netherlands

S. Matsuo, T. Segawa, T. Kakitsuka, T. Sato, R. Takahashi, H. Suzuki, B. Docter, F. Karouta, M.K. Smit, "Integrated filtered feedback tunable laser using double-ring-resonator-coupled filter," IEEE 21st International Semiconductor Laser Conference, ISLC 2008, pp. 155-156, 14 - 18 Sept., Sorrento, Italy

List of publications

J. Pozo, E.A.J.M. Bente, M.J.R. Heck, B. Docter, F. Karouta, A.A.M. Kok, J.J.G.M. van der Tol, M.K. Smit, S. Anantathanasarn, R. Nötzel, M. Yousefi, S. Beri, D. Lenstra, "InP-based lasers and photonic crystals devices for integrated photonics," 10th Anniversary International Conference on Transparent Optical Networks, ICTON 2008, pp. 131-134, 22-26 June 2008, Athens, Greece

F. Karouta, B. Docter, P. Kaspar, E.J. Geluk, M.K. Smit, "Very high aspect ratio of photonic crystals holes in InP," Proc. 12th Annual Symposium of the IEEE/LEOS Benelux Chapter 2007. (pp. 227-230). Brussels, Belgium

B. Docter, E.J. Geluk, F. Karouta, M.K. Smit, "Deep etched DBR gratings in InP for photonic integrated circuits," Proc. European Conference on Integrated Optics ECIO 2007 (ThG20). Copenhagen, Denmark

B. Docter, E.J. Geluk, F. Karouta, M.K. Smit, "Deep etched DBR mirrors for compact integrated lasers," Proc. ePIXnet Winter School 2007, Pontresina, Switzerland

B. Docter, E.J. Geluk, F. Karouta, M.J.H. Sander-Jochem, M.K. Smit, "Deep etched DBR gratings in InP for photonic integrated circuits," Proc. 19th International Conference on Indium Phosphide and Related Materials, IPRM 2007, pp. 226-228, Matsue, Japan

B. Docter, E.J. Geluk, T. de Smet, F. Karouta, M.K. Smit, "Reflectivity measurements of deeply etched DBR gratings in InP-based double heterostructures," Proc. 12th Annual Symposium of the IEEE/LEOS Benelux Chapter 2007, pp. 111-114, Brussels, Belgium

T. Segawa, B. Docter, T. Kakitsuka, S. Matsuo, T. Ishii, Y. Kawaguchi, Y. Kondo, F. Karouta, M.K. Smit, H. Suzuki, "Short-cavity DBR laser using an InP/InGaAsP deep-ridge waveguide with vertical-groove gratings," Proc. OptoElectronics and Communications Conference (OECC)/ Integrated Optics & Optical fiber Communication (IOOC) 2007, 13D1-3, pp. 650-651, Yokohama, Japan

B. Docter, E.J. Geluk, M.J.H. Sander-Jochem, F. Karouta, M.K. Smit, "Deep etching of DBR gratings in InP using CI_2 based ICP processes," Proc. 11th Symposium IEEE/LEOS Benelux Chapter, pp. 97-100, 30 Nov - 1 Dec 2006, Eindhoven, The Netherlands

F. Karouta, B. Docter, E.J. Geluk, M.J.H. Sander-Jochem, J.J.G.M. van der Tol, M.K. Smit, "Role of temperature and gas-chemistry in micro-masking on InP by ICP etching," Proc. IEEE LEOS Annual Meeting (ThDD2), pp. 987-988, Sydney, Australia

Curriculum Vitae

Boudewijn Docter was born in Amsterdam, The Netherlands, in 1978. After finishing secondary school (Montessori Lyceum Amsterdam) in 1996 he started his Electrical Engineering study at Twente University (Enschede, The Netherlands). His major was in Microsystems, with Integrated Optics as his specialty. His Master thesis was about integrated ring lasers using Erbium doped Al_2O_3 as an amplifier material on SiON waveguides. He received his MSc degree in 2002.

During his study and since 1998 Boudewijn worked as a part-time programmer at BBV, a software company making design and simulation software for integrated optics. After his graduation he continued working in this company, which was taken over by Kymata/Alcatel Optronics and later Concept2Volume (C2V), as a design engineer working on state-of-the-art AWG designs in SiO_2 technology, waveguide stress modeling and yield prediction software tools.

In 2004 Boudewijn had a short break from the field of integrated optics to work as a rock climbing expedition leader for Hot Rock Ltd., guiding an overland rock climbing trip during 11 months from Indonesia across Asia to the United Kingdom.

On June 1st 2005 Boudewijn started his PhD project at the Opto-Electronic Devices group at the faculty of Electrical Engineering of the Eindhoven University of Technology. Supervised by Dr. F. Karouta, Dr. J.J.G.M. van der Tol and Prof. M.K. Smit he worked on the development of deeply-etched DBR mirrors as a building block for complex InP-based photonic integrated circuits and tunable lasers. During his PhD project he spent 6 months at NTT Photonics Laboratories, Atsugi, Japan, to work on short-cavity lasers for photonic integrated circuits.

Presently Boudewijn continues working at the OED group to further develop the tunable laser components towards a commercially viable product for packet-switching and Fiber-To-The-Home applications.